Table of Contents

Table of Contents **1**

Table of Figures **5**

Abstract **15**

Acknowledgements **17**

Abbreviations **19**

Chapter 1 Introduction **23**

1.1 Fuel cells 23

1.1.1 Proton exchange membrane fuel cell 25

1.1.2 Direct formic acid fuel cell 27

1.1.3 Direct methanol fuel cell 29

1.1.4 Alkaline anion exchange membrane fuel cell 31

1.2 Electrocatalysis 34

1.2.1 Adsorption 34

1.2.2 Sabatier principle 35

1.2.3 Volcano plot of formic acid decomposition 38

1.3 *In situ* Infrared spectroscopy for studying electrocatalysts 39

1.3.1 CO as a surface probe 40

1.3.2 *In situ* IR spectroscopy of metal electrodes and nanoparticles 44

1.3.2.1 On Metal electrodes 44

1.3.2.2 With nanoparticles 47

1.4 Electrochemical conversion of carbon dioxide: enzymes and metals 49

1.4.1 Formation of hydrocarbons from electro-reduction of CO 49

1.4.2 Copper as CO_2 reduction catalyst 51

1.4.3 CO_2 reduction catalysed by a biological catalyst: carbon monoxide dehydrogenase 54

1.4.4 Design of a cascade system for hydrocarbon formation via CO_2 reduction 58

1.5 Aim of this Thesis 60

Chapter 2 Theory and Methodology 61

2.1 Electrochemical Theory and Methods 61

2.1.1 Three electrode system 61

2.1.2 Electrochemical responses 63

2.1.3 Cyclic voltammetry 66

2.1.4 Catalytic voltammetry and the rotating disk electrode experiments 68

2.1.5 Electrochemical cell preparation 73

2.2 Fourier transform infrared spectroscopy 75

2.2.1 Introduction to Infrared spectroscopy 75

2.2.2 Selection rule 76

2.2.3 Surface selection rule 78

2.2.4 Fourier transform infrared spectroscopy 80

2.3 Attenuated total reflectance IR spectroscopy and the spectroelectrochemical cell design 82

2.3.1 Attenuated total reflectance IR spectroscopy 82

2.3.2 Cell design for studying supported nanocatalysts 85

2.4 Experimental 89

2.4.1 Pd / XC-72 (Premetek) catalyst ink preparation 89

2.4.2 Chemicals 89

2.4.3 Electrodes and IRE cleaning 90

Chapter 3 *In situ* ATR-IR spectroelectrochemical approach for formic acid oxidation on supported nanoparticles 92

3.1 Catalyst sample preparation of for ATR-IR SEC studies 93

3.1.1 Electrochemical studies of Pd / C (Sigma-Aldrich) 93

3.1.2 *In situ* IR spectroelectrochemistry of a Pd / C (Sigma-Aldrich) 96

3.1.3 Film thickness analysis for Pd / C (Sigma-Aldrich) 101

3.2 Spectroelectrochemical study on Pd / XC-72 (Premetek) 102

3.2.1 Thinner and cleaner catalyst film 102

3.2.2 Electrochemical characterization of Pd / XC-72 (Premetek) 104

3.2.3 *In situ* IR spectroelectrochemical study for Pd / XC-72 (Premetek) 105

3.3 Discussion 108

Chapter 4 *In situ* spectroelectrochemical study of the deactivation of Pd / XC-72 particles during formic acid oxidation 110

4.1 Introduction: Formic acid oxidation and CO poisoning on Pd 110

4.1.1 Pathway review of formic acid oxidation on metals 110

4.1.2 Deactivation of Pd catalysts in formic acid oxidation 113

4.2 *In situ* IR spectroelectrochemical study of Pd / XC-72 catalyst in formic acid containing different impurities 115

4.2.1 CO poison surface 116

4.2.2 Oxidation of reagent grade formic acid 121

4.2.3 HPLC grade formic acid spiked by small organic chemicals 125

4.3 Discussion 128

Chapter 5 *In situ* spectroelectrochemical study of ethanol oxidation on Pd / XC-72 particles 131

5.1 Introduction to methanol oxidation on Pd 131

5.1.1 Pathways of methanol oxidation 131

5.1.2 Previous infrared spectroscopic studies on Pd-catalysed electro-oxidation of methanol 133

5.2 IR Spectroelectrochemical study on methanol oxidation on Pd / XC-72 nanoparticles in acidic environment 134

5.3 Methanol oxidation on Pd / XC-72in alkaline solution 139

5.3.1 Cyclic voltammetry of Pd / XC-72 in alkaline solution 139

5.3.2 Cyclic voltammetry of Pd in 0.1 M methanol in alkaline solution .. 141

5.3.3 *In situ* spectroelectrochemistry of methanol oxidation on Pd in alkaline solution 143

5.4 Discussion 150

Chapter 6 Electrochemical conversion of carbon dioxide into hydrocarbon feedstock 154

6.1 CODH / Cu particle system 154

6.1.1 BP 2000 supported CODH 155

6.1.2 Supporting copper nanoparticles on BP 2000 158

6.2 Electrochemistry of BP 2000 supported CODH and Cu 159

6.2.1 BP2000 supported CODH 159

6.2.2 BP2000 supported Cu nanoparticles 161
6.2.3 Cascade system for CO_2 reduction 163
6.3 Discussion and outlook 165
Chapter 7 Conclusion and outlook 167
7.1 Conclusion 167
7.2 Outlook 171
Bibliography 173

Table of Figures

Figure 1-1 The overview of a proton exchange membrane fuel cell. The protons generated by fuel oxidation at the anode form water with oxygen ions at the cathode after diffusing through the exchange membrane. 26

Figure 1-2 Schematic illustration of the H_2 / O_2 alkaline PEMFC's working mechanism. 32

Figure 1-3 The original volcano plot made by Balandin shows the correlation between HER activities (determined from electrocatalytic current data) and M-H bond strengths for different metals. The Pt group metal shows the most optimal M-H bond strength toward hydrogen evolution. Reprinted from reference 37 with permission. 36

Figure 1-4 Volcano plot for the decomposition of formic acid on transition metals. Adapted from reference 39. The platinum group metals show the most optimal ΔH_f for formic acid decomposition.....38

Figure 1-5 Molecular orbital diagram for carbon monoxide molecule.....42

Figure 1-6 A schematic diagram of the synergic bonding of CO to the metal. A: The σ-donation from CO(5σ) to the M(dσ). B: The π-backdonation from M(dπ) to CO(2π*). C: The interaction of adsorbed CO with a metal surface. 42

Figure 1-7 Typical frequency ranges for the CO stretching mode for carbon monoxide adsorbed in A: Linear-bonded, B: Bridge-bonded, C: Multiple-bonded and D: Hollow-bonded sites. 43

Figure 1-8 Electrochemical cells and optical arrangements used for *in situ* characterization of electrode / electrolyte interfaces with A) IRAS and B) ATR-SEIRAS. Reproduced from reference 46. 46

Figure 1-9 Experimentally determined current and product distribution at a copper electrode. Product distribution and total current produced as a function of applied potential (*vs* reversible hydrogen electrode, RHE) in the electrochemical reduction of CO_2 at a copper electrode in 0.1 M $KHCO_3$ (pH 6.8) at 18.5 C, as measured by Hori et al.[72] Reprinted with permission. 52

Figure 1-10 Overall architecture of the homodimeric CODH, highlighting the locations of all 5 cofactors. Figure prepared using pymol from data in PDB file 3I39 for the X-ray crystallographic structure of CODHII from *Carboxydothermus hydrogenoformans*. 55

Figure 1-11 States proposed to be involved in the catalytic cycle of CODH I_{Ch}. The C_{ox} state is an inactive, oxidised state that is reduced at potentials below -200 mV to the catalytically active C_{red1} state. 56

Figure 1-12 A: Protein film electrochemistry involves immobilisation of proteins by adsorbing a sub mono-layer of protein on the working electrode. By measuring electronic current and controlling electrochemical potential, the enzyme catalytic chemistry can be studied. B: The protein film voltammograms (shows the correlation between catalytic current measured and the potential (E) applied at working electrode. SHE stand for standard hydrogen electrode) of CODH electro-catalysing CO / CO_2 conversion. Reprinted from reference 83 with permission. 57

Figure 1-13 A schematic illustration for the composite electrocatalyst system for CO_2 reduction to hydrocarbons. CODH accelerates the rate of CO formation from CO_2 reduction, then relays CO to Cu for hydrogenation to hydrocarbons. 59

Figure 2-1 A schematic circuit diagram of a three electrode system. In a three-electrode system, a potential at the working electrode is imposed with respect to the reference electrode and the counter electrode is allowed to equalise the current from the reaction at the working electrode. 62

Figure 2-2 A diagram representative of double layer on the electrode-solution interface. Positive charge reflects deficiency of electron on electrode. 65

Figure 2-3 Waveform for cyclic voltammetry. The potential is applied as a function of time during cyclic voltammetry. 66

Figure 2-4 A cyclic voltammogram of 1 mM $K_3Fe(CN)_6$ in water on a glassy carbon working electrode recorded at a rate of 50 mV s^{-1}. 67

Figure 2-5 A catalytic cyclic voltammogram of carbon monoxide dehydrogenase (CODH) under a 100 % CO atmosphere at an electrode rotation rate of 1000 rpm and a scan rate of 10 mV s^{-1} . The potential dependent positive current comes from the electro-oxidation of CO to CO_2 by CODH. The catalysis is limited by mass transport when the potential is scanned above about -0.1 V, shown by the plateau in current. 69

Figure 2-6 A: A schematic image of the rotating disk electrode. B: Laminar flow lines at the rotating disk during electrode rotation. 70

Figure 2-7 Schematic concentration profile of analyte near the surface of the rotating disk electrode when the potential is great enough to reduction the concentration of analyte near 0 at the electrode surface. 71
Figure 2-8 Cyclic voltammograms of CODH on a rotating disk electrode under a 100 % CO atmosphere at 10 mV s^{-1} scan rate with different electrode rotation rates..... 72
Figure 2-9 A schematic diagram of the apparatus used for electrochemistry experiments..... 74
Figure 2-10 Vibrational modes of molecules of H_2O and CO_2. 78
Figure 2-11 The image dipole moment within the adsorbent compensates the effect of the adsorbate's dipole moment for the parallel orientation but enhances the effect of dipole moment for a perpendicular orientation. Adapted from reference 84. 79
Figure 2-12 The schematic representation surface selection rule on the metal substrate for CO and formate. 80
Figure 2-13 A schematic view of the setup of an interferometer..... 81
Figure 2-14 A: Diagram of Snell's law when an incident ray travels from one medium to another medium. B: When θ2 becomes larger than 90^0 and total internal reflection occurs..... 83
Figure 2-15 A schematic representation of the evanescent wave penetrating through a certain thickness of the sample dispersed on the IRE..... 85
Figure 3-1 Cyclic voltammogram of 100 μg Pd on matrix activated carbon in N_2-saturated 0.1 M $HClO_4$ at a GC electrode rotation rate of 1000 rpm and a scan rate of 10 mV s^{-1} 94

Figure 3-2 A cyclic voltammogram of 10 % Pd on matrix activated carbon in N_2 saturated 0.5 M $HClO_4$ with 0.1 M HCOOH. The measurement was carried out with the electrode rotating at 1000 rpm and at a scan rate of 10 mV s^{-1}.....95

Figure 3-3 A: Cyclic voltammograms for Pd on matrix activated carbon (Sigma-Aldrich) in N_2 saturated 0.5 M $HClO_4$ with 0.1 M HCOOH was collected in SEC cell solution flow rate at 12 mL min^{-1} and at scan rate 1 mV s^{-1}. B: CV recorded at an RDE measurement reproduced from Figure 3-2. 97

Figure 3-4 *In situ* IR spectra recorded simultaneously with the voltammogram in Figure 3-3A. The peak at 2341 cm^{-1} is assigned to solution phase CO_2 as the product of formic acid oxidation. The peak at lower wavenumber appears at high potential and shifts to lower wavenumber on the backward scan. 98

Figure 3-5 A: Pd on matrix activated carbon exposed to CO-saturated electrolyte at open circuit potential B: The average of spectra recorded between 1050 mV and 1150 mV v.s SHE during the potential sweep towards positive potentials in formic acid 0.1 M.....100

Figure 3-6 Scanning electron microscope image of a 60% Pd / C (Sigma-Aldrich) film collected on a Si surface showing the thickness is around 30 μm. 102

Figure 3-7 The scanning electron microscope image of a Pd / XC-72 catalyst (Premetek) film collected on a Si surface showing the thickness is < 2 μm. ...103

Figure 3-8 A: Cyclic voltammogram of Pd / XC-72 in 0.5 M $HClO_4$ with 10 mVs^{-1} scan rate B: Cyclic voltammogram of Pd / XC-72 in 0.5 M $HClO_4$ and 0.1 M formic acid with 10 mVs^{-1} scan rate. Both of the two experiments were

conducted at a RDE with the Pd / XC-72 deposited on the surface with the electrode rotating at 1000 rpm.....104
Figure 3-9 Cyclic voltammograms for Pd / XC-72 in N_2 saturated 0.5 M $HClO_4$ with 0.1 M HCOOH was collected in SEC cell with flow rate: 12 mL min^{-1} and at scan rate 1 mV s^{-1}.....106
Figure 3-10 *In situ* IR spectra recorded simultaneously with the voltammogram in Figure 3-9. The peak at 2341 cm^{-1} is assigned to solution phase CO_2 as the product of formic acid oxidation.....107
Figure 3-11 A: The cyclic voltammogram recorded during formic acid oxidation on Pd / XC-72 B: The IR peak intensity of n(CO_2) from the spectra over potential scan.....107
Figure 4-1 Cyclic voltammogram of CO-bound Pd / XC-72 in the SEC cell in N_2 saturated 0.5 M $HClO_4$. The CO-saturated acid was first flowed in and out of the SEC cell for 300 seconds and then the catalyst film was washed by pumping N_2-flushed acid in and out of the SEC cell for another 300 seconds before and during the measurement. Scan rate: 1 mVs^{-1}. Flow rate: 12 mL min^{-1}.....117
Figure 4-2 *In situ* ATR-IR spectra of the Pd / XC-72 recorded simultaneously with the voltammogram in Figure 4-1 (Positive-going scan). Two n(CO) IR peaks, CO_L and CO_B were found after the CO-saturated solution flowed into SEC cell. The spectrum that was recorded at 0 V before CO-saturated solution introduced into SEC cell is used as the background. 119

Figure 4-3 Cyclic voltammogram recorded in 0.1 M reagent grade of formic acid oxidation in the SEC cell. Scan rate: 1 mV sec^{-1}. Solution flow rate: 12 mL min^{-1}. 121

Figure 4-4 A: Zoomed-in spectrum of the spectrum at 0.7 V B: *In situ* ATR-IR spectra of the Pd / XC-72 recorded simultaneously with the voltammogram Figure 4-3. 122

Figure 4-5 A) Time-resolved ATR-IR spectra of the Pd / XC-72 recorded simultaneously with the voltammogram in Figure 4-3A (Positive scan) B) Top: the integrated area between 1700-1870 cm^{-1} as CO peak intensity. Middle: peak intensity of CO_2. Bottom: The cyclic voltammogram record under reagent grade of formic acid oxidation in the SEC cell..... 123

Figure 4-6 *In situ* ATR-IR spectra of the Pd / XC-72 recorded during potential scan from 0 V to 1.2 V in 0.5 M $HClO_4$ with 0.1 M HPLC grade formic acid and 100 ppm methanol. Scan rate: 1 mVs^{-1}. Flow rate: 12 mL min^{-1}..... 126

Figure 4-7 Difference spectra of Pd / XC-72 in formic acid with different impurities at 0.8 V. All the different spectra uses the spectrum recorded at 0 V under the same condition as background. 127

Figure 5-1 The parallel pathways of methanol oxidation proposed by the reference 116. 132

Figure 5-2 Red: Cyclic voltammogram of Pd / XC-72 in 0.5 M $HClO_4$. Black: Cyclic voltammogram of Pd / XC-72 in the 0.5 M $HClO_4$ containing 0.1 M CH_3OH. Both were recorded at a 1 mV sec^{-1} scan rate and 12 mL min^{-1} flow rate in the SEC cell..... 136

Figure 5-3 A: *In situ* ATR-IR spectra of Pd / XC-72 catalyst recorded simultaneously with the voltammogram in Figure 5-2 black line B: the integrated area between 1700-1870 cm^{-1}, indicative of CO peak intensity (blue) and the peak intensity of CO_2 during potential scan in Figure 5-2. C: the cyclic voltammogram recorded under methanol oxidation in the SEC cell reproduced from Figure 5-2. 138

Figure 5-4 A cyclic voltammogram of Pd / XC-72 on a RDE electrode in 0.5 M KOH at 10 mV s^{-1} scan rate and 1000 rpm rotation rate. 140

Figure 5-5 Cyclic voltammogram of Pd / XC-72 on a RDE in 0.5 M KOH containing 0.1 M methanol at 1 mV s^{-1} at 10 mV s^{-1} scan rate and 1000 rpm rotation rate. 142

Figure 5-6 A: The amplified spectrum between 1700-2000 cm^{-1} at -0.2 V B: ATR-IR spectra of the Pd / XC-72 recorded simultaneously with the voltammogram in Figure 5-7 black line..... 145

Figure 5-7 The infrared peak intensities of different IR signals during potential scan. n_{as}(OCO) band of $HCOO^-$ (brown), d(C-H) band of $HCOO^-$ (red), n_s(OCO) band of $HCOO_{ads}$ (green) and n(CO_H) of hollow-bound CO (blue). The cyclic voltammogram recorded under of methanol oxidation in the SEC cell in 0.5 KOH + 0.1 M methanol (black) 147

Figure 5-8 Difference spectra recorded at different potentials in 0.1 M methanol, processed using the initial spectrum at -0.8 V as reference..... 149

Figure 5-9 IR spectra of black: 0.1 M 0.1 M HCOOH + 0.1 M KOH red: 0.1 M methanol + 0.5 M KOH. Both against the spectra taken with 0.5 M KOH. ... 151

Figure 5-10 The parallel pathways of methanol oxidation on Pd.[117] The blue region presents the idea that in alkaline conditions the methanol oxidation mainly goes though the formic acid pathway. The reaction also goes through the CO pathway, but this is much less favourable. The red region presents the idea that in acid solution methanol oxidation is dominated by the CO pathway. 152

Figure 6-1 A schematic illustration for the composite electrocatalyst system for CO_2 reduction to hydrocarbons.....155

Figure 6-2 Different spectrum of 1 µL film of BP 2000 supported CODH dispersion using the spectrum taken with Si prism as background. The clear amide 1 band at 1645 cm^{-1} and amide 2 band at 1550 cm^{-1} indicates the existence of protein of the carbon particles. 157

Figure 6-3 Protein film voltammetry of CODH under 100 % CO. Rotation rate: 1000rpm, scan rate: 10 mV s^{-1}.....159

Figure 6-4 Protein film voltammetry of CODH: blue: CODH on BP 2000 on PGE under 100 % N_2, red: CODH film under 100% CO_2 on PGE. Rotation rate: 1000 rpm, scan rate: 10 mV s^{-1}.....160

Figure 6-5 The cyclic voltammogram of BP 2000 supported Cu nanoparticles on a PGE electrode. Scan rate: 50 mV sec^{-1} Rotation rate: 1000 rpm. The CV shows typical features of Cu nanoparticles suggesting Cu nanoparticles are well supported on BP 2000.....161

Figure 6-6 The cyclic voltammetry of BP 2000 supported Cu under 100 % N_2 (black), 100 % CO_2 (red) atmosphere in pH 6.0 50 mM MES buffer at 10 mV s^{-1} scan rate and 1000 rpm rotation rate.....162

Figure 6-7 A: The cyclic voltammetry of BP 2000 supported Cu under 100 % N_2 (black) and 100 % CO_2 (red) atmosphere, reproduced from Figure 6-6. B: the cyclic voltammetry of BP 2000 supported Cu / CODH under 100 %N_2 (black), 100 % CO_2 atmosphere. All the CVs were recorded at 10 mV s^{-1} scan rate and 1000 rpm rotation rate. 164
Figure 6-8 The potential sweep of BP 2000 supported Cu (black) and BP 2000 supported Cu / CODH (red) under 100 % CO_2 atmosphere at 10 mV s^{-1} scan rate and 1000 rpm rotation rate. 165

Abstract

Studies of carbon monoxide activation and poison on metallic and enzymatic sites: The new ATR-IR spectroelectrochemical approach

Gan-Zuei Chang
Brasenose College, University of Oxford
A Thesis submitted for the degree of Doctor of Philosophy, Hilary Term 2016

Direct liquid fuel cells (DLFCs) offer a great opportunity to replace traditional fuel combustion with cleaner localised energy production. One of the biggest challenges for developing a commercial DLFC device is the production of CO during fuel oxidation. CO is not only one of the most common intermediates of hydrocarbon fuels oxidation but also a poison of most metal catalysts. *In situ* infrared (IR) spectroelectrochemical (SEC) techniques have been intensively used to understand the reaction mechanisms for oxidation of different fuels and to study the presence and activation of CO on different bulk metal electrodes. However, there have been few studies of supported nanocatalysts during electrocatalytic turnover relevant to realistic fuel cell devices. In this Thesis, a new attenuated total reflectance IR (ATR-IR) SEC approach is used to study the

electrocatalytic oxidation of formic acid and methanol on a commercial carbon supported Pd nanocatalyst (Premetek, USA, 60% Pd / XC-72).

The results from ATR-IR SEC studies of formic acid oxidation on the Pd nanoparticles show CO poisoning, and reveal that this is derived from trace organic impurities present in reagent grade formic acid, rather than from the dehydration of formic acid itself.

The supported Pd catalyst shows very different activities for methanol oxidation in different pH conditions. In acidic conditions, the catalyst is strongly poisoned by adsorbed CO and shows very low activity towards methanol oxidation. On the other hand, in alkaline conditions, only very weak IR signal from adsorbed CO can be detected and the activity of methanol oxidation is much higher compared to the acidic conditions. The detection of strong IR signals from formate suggests that formate acts as a significant reactive intermediate.

In the final part of this Thesis, the possibility of developing a more efficient electrocatalytic system to reduce greenhouse gas CO_2 to hydrocarbon feedstocks is demonstrated by using a composite catalyst which comprises an enzyme to reduce CO_2 to CO, and copper nanoparticles for further reduction of CO.

Overall this Thesis provides insight into the activation of CO at metal sites during electrocatalytic reactions which are relevant to energy technologies.

Acknowledgements

Firstly, I would like to express my sincere gratitude to my supervisor Professor Kylie Vincent for the continuous support of my DPhil study and related research, for her patience, motivation, and immense knowledge. Her guidance helped me in all the time of research and writing of this thesis. Without her constant support and encouragement, this work would have never been done.

My sincere thanks also goes to Dr. Ian Mcpherson and Dr. Robert Jacobs for their helps on establishing experiment methods in the initial stage of the *in situ* SEC project. They have also offered many valuable ideas and useful discussions for the project.

I would also like to thank Dr. Matteo Duca for his helps and very useful suggestions on the work of CO_2 electro-reduction project and Dr. Simantini Nayak for her ideas and discussion on modification of the SEC cell. I also must thank Dr. Phil Ash for his guidance of instrument setup (a lot of tubing), fixing all the broken instruments (mainly on IR spectrometer problems and the doors of glove boxes) and providing exotic spicy food and extra strong coffee.

My thanks extend to all of the members of the Vincent Group, past and present. Without them, working in Vincent group will not be so fun.

I am very grateful to the Hulme completion grant and all the financial supports (including free food and drinks in college) from Brasenose College to support my research and life.

I am thankful for great support from my family in the hardest time. Finally, thanks to all my friends who have shared great memories with me in Oxford.

Abbreviations

Å	Angstrom (10^{-10} m)
AEM	Anion exchange membrane
AAEMFC	Alkaline anion exchange membrane fuel cell
Ag/AgCl	Silver / Silver chloride reference electrode
ATR	Attenuated total reflectance
°C	Degrees Celsius
CODH	Carbon monoxide dehydrogenase
DFAFC	Direct formic acid fuel cell
DLFC	Direct liquid fuel cell
DMFC	Direct methanol fuel cell
E	Electrode potential
E_m	Midpoint potential

E°	Standard reduction potential
FAO	Formic acid oxidation
FT	Fourier transform
GC	Glassy carbon
HER	Hydrogen evolution reaction
I	Current
IR	Infrared
IRAS	Infrared reflection absorption spectroscopy
MMSE	Mercury-mercurous sulfate electrode
MOR	Methanol oxidation reaction
NMR	Nuclear magnetic resonance
PFE	Protein film electrochemistry
PGE	Pyrolytic graphite edge
ppm	Parts per million

s	Second(s)
SCE	Saturated calomel electrode
SEC	Spectroelectrochemistry
SEIRAS	Surface enhanced infrared spectroscopy
SHE	Standard hydrogen electrode
t	Time
T	Temperature
UPD	Underpotential deposition

Chapter 1

Introduction

1.1 Fuel cells

Since the industrial revolution, natural energy resources (such as oil and coal) have been rapidly used up. Widescale combustion of oil and coal has released large amounts of carbon dioxide (CO_2) into the atmosphere. It is widely recognised that the high concentration of CO_2 in the atmosphere is one of the major factors causing the greenhouse effect and leading to global climate change.[1] Therefore, cutting down CO_2 emissions and looking for new sources of clean, renewable energy to replace traditional fuel combustion becomes very important. One of the most promising alternative energy technologies are fuel cells. The fundamental principle of fuel cells includes oxidation of the fuel at the anode and reduction of the oxidant at the cathode.[2] The electrons generated from anodic oxidation lead to an electric current being produced in the external circuit. There are five major types of fuel cell, which are classified by the type of electrolyte they use, as shown in Table 1-1 below:[3,4]

Table 1-1 Major types of fuel cell.[3,4]

Fuel Cell Name	Fuel	Electrolyte / Charge Carriers	Operating Temperature (°C)
Alkaline fuel cell (AFC)	H_2	KOH solution / OH^-	< 80 °C
Proton exchange membrane fuel cell (PEMFC)	H_2 / hydrocarbons	Polymer membrane / H^+	< 150 °C
Phosphoric acid fuel cell (PAFC)	H_2	Phosphoric acid / H^+	ca. 200 °C
Molten carbonate fuel cell (MCFC)	Hydrocarbons	Molten carbonate / CO_3^{2-}	650 - 800 °C
Solid oxide fuel cell (SOFC)	Hydrocarbons	Ceramic / O_2^-	500 -1000 °C

Most of these types of fuel cell are still in the laboratory development stage. Proton exchange membrane fuel cells are one of the types of fuel cell that are presently near to be commercialised.

1.1.1 Proton exchange membrane fuel cell

The proton exchange membrane fuel cell (PEMFC) has the advantages of low operating temperature, high power density and relatively lower cost which offers a great chance for being developed to a commercialised product. This makes it superior to other types of fuel cell listed in Table 1-1.[3–6] In a PEMFC, protons and electrons are formed by the oxidation of fuels. Figure 1-1 shows the schematic overview of a PEMFC. The PEMFC employs a proton conducting polymeric membrane as its electrolyte, which separates the anode and cathode sides, as shown in Figure 1-1. The membrane, catalyst layers and the gas diffusion layers (GDL) are collectively called the membrane electrode assembly (MEA). In a typical dihydrogen PEMFC, at the anode catalyst layer, the H_2 oxidation reaction (HOR) takes place: H_2 is electrochemically oxidised into protons and electrons as Equation 1-1.

$$2H_2 \rightarrow 4H^+ + 4e^- \quad \text{(1-1)}$$

The protons are conducted through the membrane to the cathode, whereas the electrons are forced to travel in an external circuit to the cathode, because the membrane is electrically insulating. At the cathode catalyst layer, the protons

which have diffused from the anode catalyst layer react with O_2 which is reduced to H_2O as shown in Equation 1-2.

$$4H^+ + 4e^- + O_2 \rightarrow 2H_2O \quad \text{.....(1-2)}$$

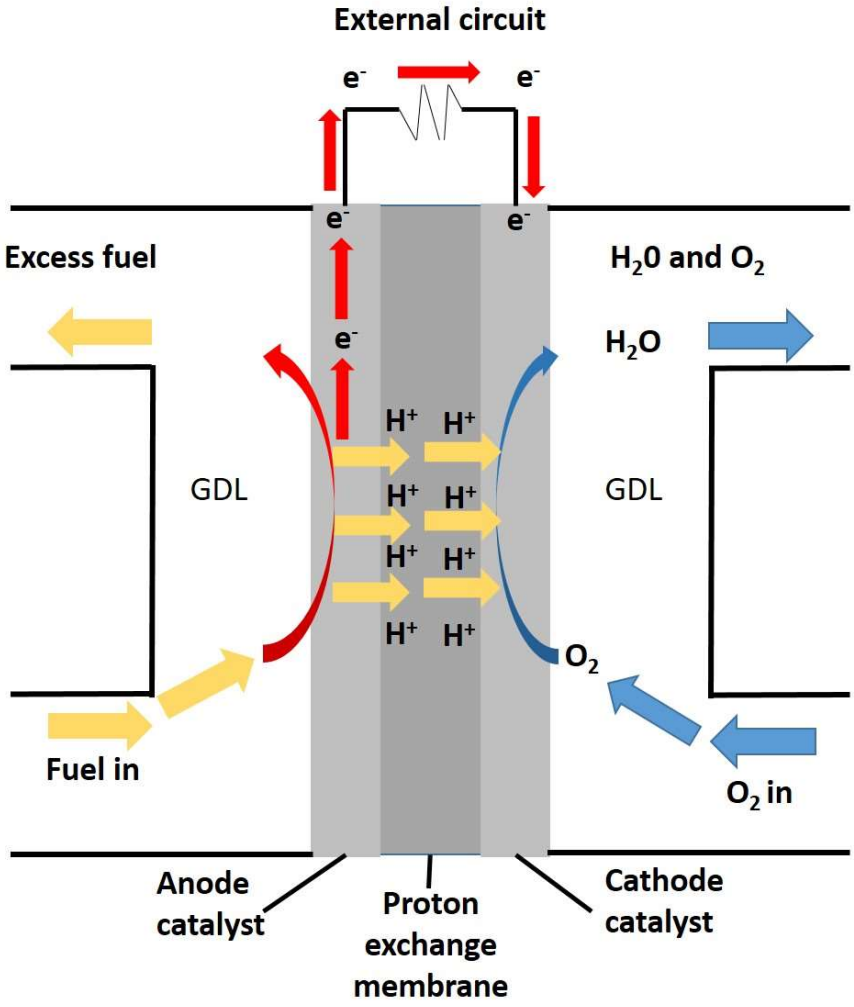


Figure 1-1 The overview of a proton exchange membrane fuel cell. The protons generated by fuel oxidation at the anode form water with oxygen ions at the cathode after diffusing through the exchange membrane.

In the last few decades, a number of liquid fuels have been studied with the purpose of replacing hydrogen gas in fuel cell applications.[7] The use of liquid

fuels such as formic acid (HCOOH), methanol (CH_3OH) and ethanol (C_2H_5OH) have several advantages over H_2, principally that the technology and infrastructure for their production, storage and transportation has been well established over many decades.[8] Furthermore, they provide comparable energy densities to that of liquid H_2.

In the next two sections, two different types of PEMFCs using formic acid and methanol as fuels will be introduced.

1.1.2 Direct formic acid fuel cell

The direct formic acid fuel cell (DFAFC) is based on a similar concept to the dihydrogen PEMFC. Instead of H_2, formic acid is used at the anode as the fuel (Figure 1-1). Formic acid has a relatively lower energy density than methanol and ethanol,[9] and the performance of a DFAFC is comparatively lower than for alcohol fuel cells.[10,11] However, formic acid is a liquid under atmospheric pressure, and distributing and transporting formic acid is easy. Therefore, formic acid is still in consideration as an alternative liquid fuel, instead of H_2 or other natural gases.

The half-reaction of the formic acid oxidation at the anode and the cathodic reaction are shown in Equation 1-3 and 1-4 respectively.

$$HCOOH \rightarrow CO_2 + 2H^+ + 2e^- \quad \text{.....(1-3)}$$

$$2H^+ + 2e^- + 1/2O_2 \rightarrow H_2O \quad \text{.....(1-4)}$$

Noble metals are generally used as the fuel cell catalysts due to these metals having vacant orbitals and available d electrons. More detail of electro-catalysis chemistry on metal surfaces will be introduced and discussed in section 1.2. It is generally accepted that the electrocatalytic oxidation of HCOOH to CO_2 on a metal surface proceeds via a dual path mechanism. This involves the direct oxidation of reactive weakly-adsorbed intermediates to form CO_2 in parallel with the indirect oxidation (Equation 1-5 and 1-6) pathway involving formic acid dehydration and the subsequent electro-oxidation of the resultant strongly-adsorbed carbon monoxide (CO_{ads}) to CO_2.[12–14]

Direct Pathway: $HCOOH \rightarrow$ reactive intermediates $\rightarrow CO_2 + 2H^+ + 2e^-$…….(1-5)

Indirect Pathway: $HCOOH \rightarrow CO_{ads} + H_2O \rightarrow CO_2 + 2H^+ + 2e^-$……(1-6)

Pt and Pt-based catalysts are widely used as fuel cell catalysts.[12,15] However, using a Pt-based catalyst for DFAFC is unfavourable due to the low energy density and high possibility of CO poisoning on the Pt surface.[16,12,17,18] Electrocatalysts made of different materials show very different performances for formic acid oxidation and resistance against CO poisoning.[15,19]

It is well-known that the interaction of formic acid molecules with Pt and Pd surfaces is completely different.[12,15,20–22] Pd is able to break only the O–H bonds of the HCOOH molecule in the entire potential region, while Pt seems to have a propensity to break the C–O and / or C–H bond (at low overpotentials) and the O–H bond (at high overpotentials).[12,15,20,21] Therefore, formic acid oxidation on

Pd surfaces can mainly go through the dehydrogenation reaction step (Equation 1-5), whereas, on Pt surfaces the dehydration (indirect) pathway is dominant at low potentials. The use of a pure Pd catalyst as an anode has been recently demonstrated by Masel et al. to give superior oxidation performance in DFAFCs, compared to use of Pt-based catalysts, due to its high activity even at low temperature.[23] However, pure Pd has a significant drawback that its high performance is not sustained for extended periods of time and the mechanism of FAO on Pd is still very unclear and debatable.[24,25]

In chapter 3 and chapter 4, the mechanism of formic acid oxidation on a Pd catalyst is studied mechanistically to further our understanding of this process.

1.1.3 Direct methanol fuel cell

Similar to DFAFC, the direct methanol fuel cell (DMFC) is based on the concept of a proton exchange membrane fuel cell, using methanol as fuel instead of hydrogen gas. At the anode, the methanol is oxidised to carbon dioxide and six protons, plus six electrons (Equation 1-7). The six protons formed react at the cathode with oxygen to form water (Equation 1-8).

Anode: $CH_3OH + H_2O \rightarrow CO_2 + 6H^+ + 6e^-$ .....(1-7)

Cathode: $6H^+ + 6e^- + 3O_2 \rightarrow 3H_2O$.....(1-8)

Full oxidation of methanol releases six protons and electrons per molecule and offers high energy density, making methanol a suitable fuel for fuel cells.[26]

Similar to other direct alcohol fuel cells (DAFCs), Pt and Pt-based materials are the most common catalysts for methanol oxidation due to their high reactivity.[24,27] The mechanism of methanol oxidation is more complicated than formic acid oxidation (because it is a multi-electron and multi-proton process) and is believed to go through several parallel pathways. The main drawback of DMFC is also the poisoning of the metal catalyst surface. Various surface intermediates are formed during methanol electro-oxidation. Methanol mainly decomposes to CO which is then further oxidised to CO_2. Other adsorbed species are also formed: COH_{ads}, HCO_{ads}, $HCOO_{ads}$[28] leading to the main by-products formaldehyde and formic acid. Some of these intermediates are not easy to be oxidised and remain strongly adsorbed on the catalyst surface. Consequently, they block methanol molecules from adsorbing and undergoing further reaction.[24,28] To prevent these poisoning effects, recent research has focused on finding or developing new materials to replace Pt and Pt-based catalysts. Although Pd has great activity toward formic acid oxidation since it can bypass the CO pathway, only very low activity was found when Pd was used as anode catalyst for a DMFC operating in acidic conditions.[29] Recently, a high activity toward methanol oxidation in alkaline conditions has been reported for a Pd-based anode.[30,31] This offers an opportunity for using Pd as the electrocatalyst for methanol oxidation in alkaline conditions.

In next section, the use of Pd as the catalyst for methanol oxidation in alkaline media and the concept of alkaline anion exchange membrane fuel cells (AAEMFC) and will be introduced.

1.1.4 Alkaline anion exchange membrane fuel cell

The PEMFCs introduced in the previous sections are usually operated in acidic solutions such as sulphuric acid (H_2SO_4) or perchloric acid ($HClO_4$). However, the corrosion of the fuel cell compartment is one of the big problems of PEMFC. Nowadays, because of the successful developments of alkaline anion-exchange membranes (AAEM),[32–34] it is possible to develop direct fuel cells which operate in alkaline conditions.[33–35] Moreover, it has been found that some of the noble metals also show much better activities for electro-oxidation of organic fuels in alkaline solution than in acidic solution.[35] Therefore, a type of fuel cell, the alkaline anion exchange membrane fuel cell (AAEMFC) has attracted significant research interest. This fuel cell is operated in alkaline solution, usually potassium hydroxide (KOH). Just like the typical dihydrogen PEMFC, dihydrogen acts as the fuel and dioxygen acts as the oxidant. Figure 1-2 shows a schematic representation of a typical dihydrogen AAEMFC, where the catalysed oxygen reduction reaction at the cathode can produce OH^- ions (Equation 1-9). When the OH^- ions pass through the AAEM to the anode, they react with H_2 to form H_2O and release electrons (Equation 1-10).

$O_2 + 2H_2O + 4e^- \rightarrow 4OH^-$.....(1-9)

$2H_2 + 4OH^- \rightarrow 4H_2O + 4e^-$.....(1-10)

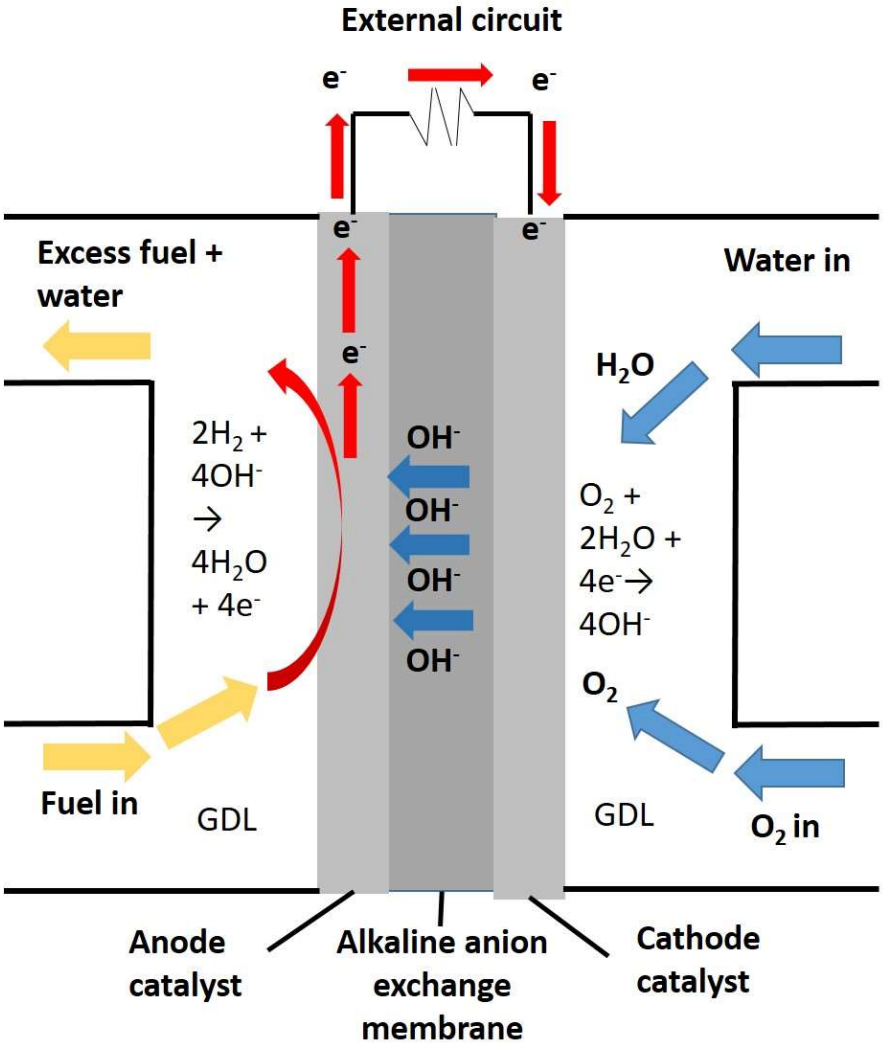


Figure 1-2 Schematic illustration of the H_2 / O_2 alkaline PEMFC's working mechanism.

The electrons released from H_2 oxidation will pass through the external circuit to be consumed in the reduction of dioxygen. This electric current between the anode and cathode is used to produce power.

The oxidation of methanol can be also used in AAEMFCs. In an alkaline direct methanol fuel cell, the half-cell reaction can be written as Equation 1-11 and Equation 1-12.

Anode: $CH_3OH + 6OH^- \rightarrow CO_2 + 5H_2O + 6e^-$ .....(1-11)

Cathode: $3/2O_2 + 3H_2O + 6e^- \rightarrow 6OH^-$ .....(1-12)

As discussed previously, for methanol oxidation in DMFCs, Pt and Pt-based catalysts show an excellent catalytic activity in acid electrolytes. However, typically, pure Pt catalysts are easily poisoned by by-products during methanol oxidation.[24,36] Unlike formic acid oxidation, Pd and Pd-based catalysts show very little activity toward methanol oxidation.[24] Interestingly, a high activity for methanol electro-oxidation in alkaline electrolyte was observed on Pd.[30,37] This offers a great opportunity for using Pd-based catalysts for alkaline direct methanol fuel cells.

There have been a limited number of mechanistic studies on methanol oxidation on Pd in either acidic or alkaline conditions. In chapter 5, the mechanisms of methanol oxidation on a supported Pd catalyst are studied in both acidic and alkaline conditions.

1.2 Electrocatalysis

In chemistry, the concept of catalysis is defined as the increase of the reaction rate of a certain chemical reaction due to the participation of an additional substance, without any chemical change to the substance. This substance is called a "catalyst". With a catalyst, reactions occur faster and require less activation energy. These definitions can be directly applied to electrocatalysis and electrocatalysts. An electrocatalyst is an electrode material that interacts with certain species during a Faradaic reaction, but still remains unchanged. Since most electrodes are metallic, so electrocatalysts are usually heterogeneous metallic catalysts. This means that the reactions take place on the metal surfaces of the catalysts, and there exist adsorption / desorption steps on the surfaces of electrocatalysts.

The basic concepts of the electrocatalysis on the heterogeneous metallic electrode surfaces are introduced and discussed in this section.

1.2.1 Adsorption

There are several possible outcomes when atoms or molecules collide with a metal surface. The first is "elastic scattering", in which the atom or molecule bounces back off the surface without any energy exchange between the surface and the incident atom or surface. The second possible outcome is that the atoms or molecules rebound from the surface and they lose or gain energy in an

"inelastic scattering" process. The third possibility is that the atoms or molecules stay on the surface spontaneously. Both of the second and third outcomes involve short or long periods when the atoms or molecules are bound to the metal surface. This is called "adsorption". Adsorption can occur either by physisorption, where the bond is weak with little or no change in the electronic structure, or more strongly through chemisorption. Chemisorption of a molecule to the surface involves a rearrangement of the valence levels of the molecule, resulting the formation of chemical bonds between the adsorbed species and the metal surface. Electrocatalysis occurs during the adsorption process since the electron transferred from the electrode can participate in the formation or dissociation of the chemical bonds, or the electrode acts as a platform for different atoms and molecules to be arranged close together. The atom or molecule that is adsorbed on the surface is usually described as the adsorbate and the adsorbing surface is usually called the adsorbent or the substrate. In this Thesis, to avoid confusion of the term "substrate" with general term of enzymatic reactant in later chapters, the adsorbent is used to describe the adsorbing surface.

1.2.2 Sabatier principle

A heterogeneous electrocatalyst accelerates a chemical reaction by binding the reagents onto the surface of the electrode. When the reagents are bound to the electrode surface, the chemical bonds of the reactants become weaker. This

offers the chance for forming new bonds or breaking chemical bonds. In addition, the probability that the reagents interact with each other is increased by binding them together on the catalyst surface.

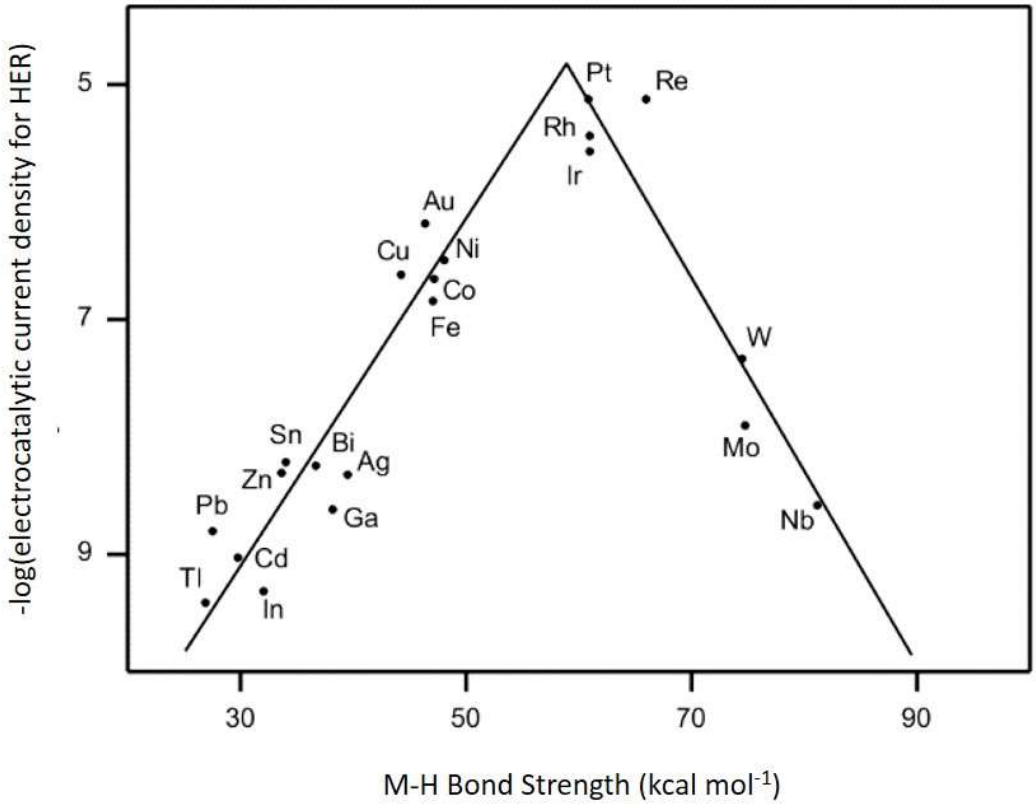


Figure 1-3 The original volcano plot made by Balandin shows the correlation between HER activities (determined from electrocatalytic current data) and M-H bond strengths for different metals. The Pt group metal shows the most optimal M-H bond strength toward hydrogen evolution. Reprinted from reference 37 with permission.

The affinity between the reagent (adsorbate) and adsorbent is known as the "reactivity" of the catalyst. The efficiency of the catalyst is called the "activity" of the catalyst. Because the products need to be released from the catalyst

surface once they are formed, the binding energies of the different intermediates to the surface are very important for the efficiency of the catalyst.

A good active catalyst needs to have a strong enough binding energy towards the key intermediates, so that the reagents will be likely to bind and react. However, it is also very important that the binding energy is weak enough that the products can easily be desorbed. This concept is known as the Sabatier principle and is well represented by plotting a catalyst's activity versus its strength of binding with hydrogen (M-H). The plot is known as a Sabatier plot or Volcano plot (Figure 1-3).[38,39] The original volcano plot (Figure 1-3) gives a triangular shaped curve, where the top corresponds to the most optimal binding energy. Figure 1-3 shows the volcano plot for the hydrogen evolution reaction (HER) on different metal surfaces (M) plotted by Balandin.[38] The only intermediate for this reaction is adsorbed hydrogen (H). Therefore, the bond strength between H and the metal surface determines the activity of the catalyst. The optimal materials are those close to the top of the volcano. The materials on the right side in Figure 1-3 have stronger M-H bond energies, so the products cannot be desorbed easily. Therefore, although they have the high reactivity (higher affinity to bind the reactant), the activity is still low. On the left hand side, the materials have too little binding energy, so the hydrogen cannot be adsorbed on the surface to be reduced into dihydrogen (low reactivity and activity). This clearly explains the difference between the reactivity and activity of a catalyst. The binding energy is a measure of the reactivity since it tells us

how much the catalyst interacts with the reactants. On the other hand, activity is the measured rate of the catalytic reaction and depends on the optimal catalyst reactivity.

1.2.3 Volcano plot of formic acid decomposition

As described in section 1.1, the anodic reaction of a direct liquid fuel cell is the electro-oxidation of the liquid fuel such as formic acid or methanol.

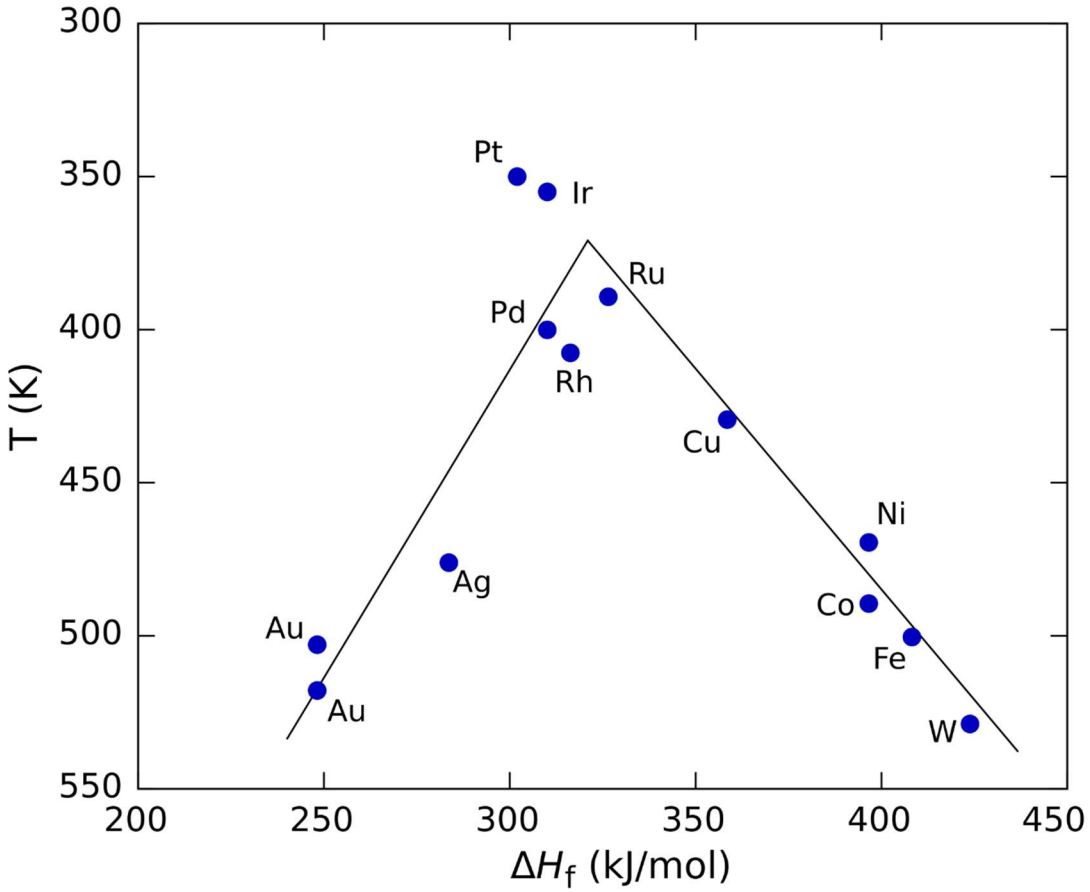


Figure 1-4 Volcano plot for the decomposition of formic acid on transition metals. Adapted from reference 39. The platinum group metals show the most optimal ΔH_f for formic acid decomposition.

Figure 1-4 shows a volcano plot for the decomposition of formic acid on different transition metals.[40] In this case, the heat of formation (ΔH_f) of the metal formate salt was used for the x axis because studies have shown that the reaction intermediate was a surface formate. For the y axis, the temperature at which the reaction reaches a specific rate was used (the y axis is plotted in reverse to preserve the conventional "volcano" shape). At low values of ΔH_f, the reaction is slow (in other words, it requires higher temperatures) because the rate of adsorption is slow and rate-limiting. At high values of ΔH_f, desorption becomes the rate-determining step. The maximum rate, which is observed for the platinum group metals in this case, requires intermediate values of ΔH_f, with the rate being a combination of the rate of adsorption and the rate of desorption.[40] However, the electro-oxidation of formic acid on a transition metal electrode in solution is far more complicated than in the gas phase under standard conditions. The reaction involves more than one intermediate including CO as a reaction poison. Moreover, the electrolytes and water molecules also play important roles on the electrode surface.

1.3 *In situ* Infrared spectroscopy for studying electrocatalysts

Conventional electrochemical techniques, such as cyclic voltammetry and potential step chronoamperometry, are of course very powerful and invaluable in studying electrocatalytic reactions. However, it is difficult to elucidate

reaction mechanisms at molecular and atomic scales only from information obtained from such electrochemical measurements.[41]

Infrared spectroscopy is one of the most popular techniques for studying liquid / solid interfaces.[42] This is particularly true for fundamental electrochemical studies, in which the molecular-level insight into the electrode process provided by infrared spectroscopy often allows the determination of the identity of adsorbed or solution species, the potential-dependent evolution of surface coverage, and the geometrical orientation of adsorbed species.

1.3.1 CO as a surface probe

Studies of carbon monoxide on catalyst surfaces are important in fuel cell chemistry since the formation of CO_{ads} is common in the electro-oxidation of organic fuels. Moreover, CO is widely used as a probe of the surface structure in IR spectroscopic study on metal surfaces. It gives rise to strong bands in the mid-IR region which do not overlap with other common IR signals such as strong bands from water and carboxylic groups. In addition, the stretching frequency of CO_{ads} not only reports on the C–O bond strength, but can also indirectly offer details about the electronic properties of the metal. This is because of the delocalisation of the M–C–O bonding orbitals. The simple Dewar-Chatt or Blyholder model was first proposed to describe the bonding of CO on the metals.[43]

In CO the electronic configuration in molecular orbitals is:

$1\sigma^2\ 2\sigma^2\ 3\sigma^2\ 4\sigma^2\ 1\pi^4\ 5\sigma^2\ 2\pi^*$

With the $2\pi^*$ orbital unoccupied.

Figure 1-5 shows a schematic representation of the molecular orbitals in CO. The three outer filled valence orbitals of a free CO molecule are sketched in Figure 1-5. These are the 5σ orbital, the doubly degenerate 1π orbital and the 4σ orbital, which have increasing binding energies. When CO is adsorbed on a metal surface, the highest occupied molecular orbital (HOMO), CO(5σ), is significantly hybridised with the substrate d-electrons. The chemisorption of CO on metal can be formed by overlap of the filled 5σ with an empty dσ orbital of the metal to form a M-C bond (CO(5σ) → M(σ)) and leads to a drift of electrons from the CO to the metal as shown in Figure 1-6A. As the lowest unoccupied molecular orbital (LUMO), the empty $2\pi^*$ antibonding orbital is also available to take part in the reaction with the surface. The partially-filled or full dπ orbitals of the metal M(dπ) can donate electron density into the empty $2\pi^*$ orbital of CO (M(dπ)→CO($2\pi^*$) to make a bond as shown in Figure 1-6B. The combination of σ and π orbitals of CO in the interaction with the metal surface is called synergic bonding as shown in Figure 1-6C. The IR band wavenumber is sensitive to the potential of the metal surface. At more negative potentials a build up of charge at the electrode results in increased back donation to the CO($2\pi^*$) orbital.

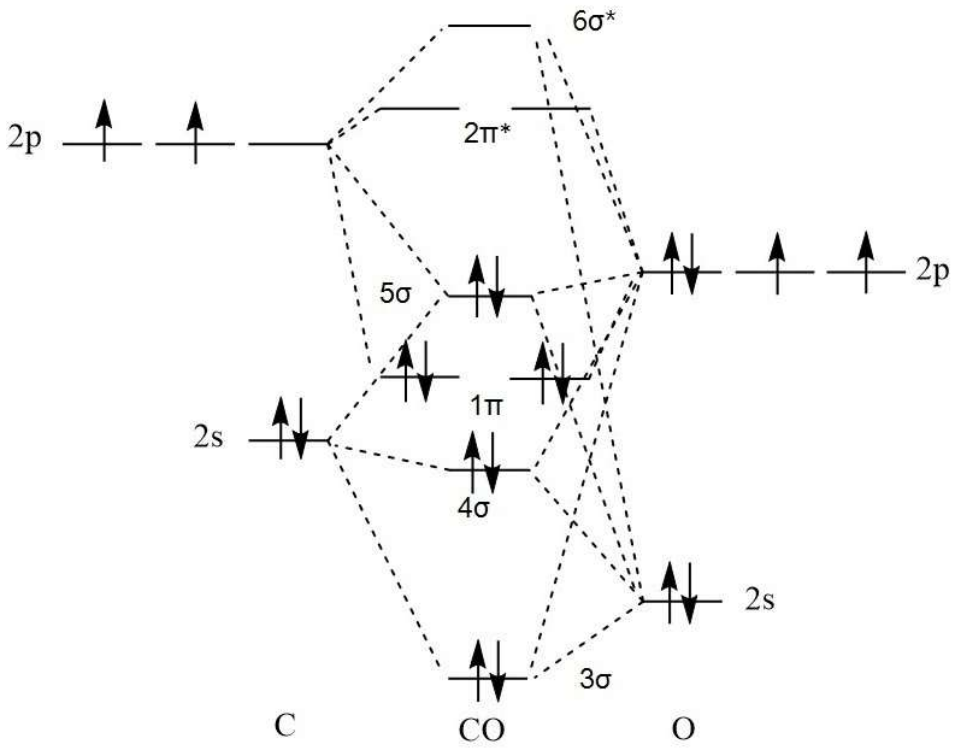


Figure 1-5 Molecular orbital diagram for carbon monoxide molecule.

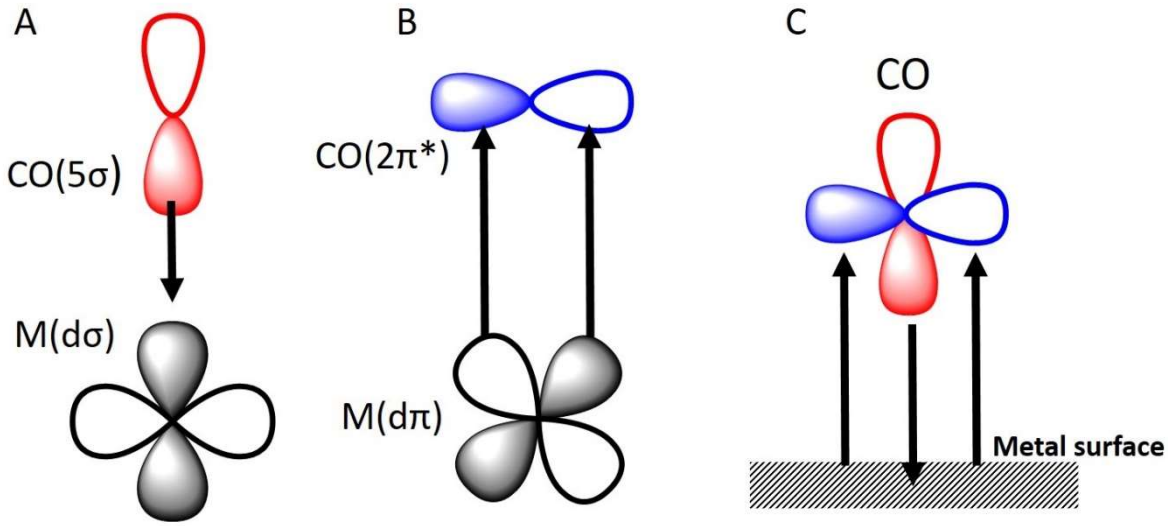


Figure 1-6 A schematic diagram of the synergic bonding of CO to the metal. A: The σ-donation from CO(5σ) to the M(dσ). B: The π-backdonation from M(dπ) to CO(2π*). C: The interaction of adsorbed CO with a metal surface.

This enhances the M–C interaction and decrease C–O interaction, the centre of the IR band shifts to lower wavenumber. Similarly at more positive potentials, the electron density is withdrawn from the CO(2π*) orbital and the peak centres would be expected to move to higher wavenumber. A different interpretation of the same observation is known as the electrochemical Stark effect. In this mechanism it is proposed that it is the strong electric fields that exist at the interface that are responsible for the shift, by their coupling to the dipole field of the adsorbate.

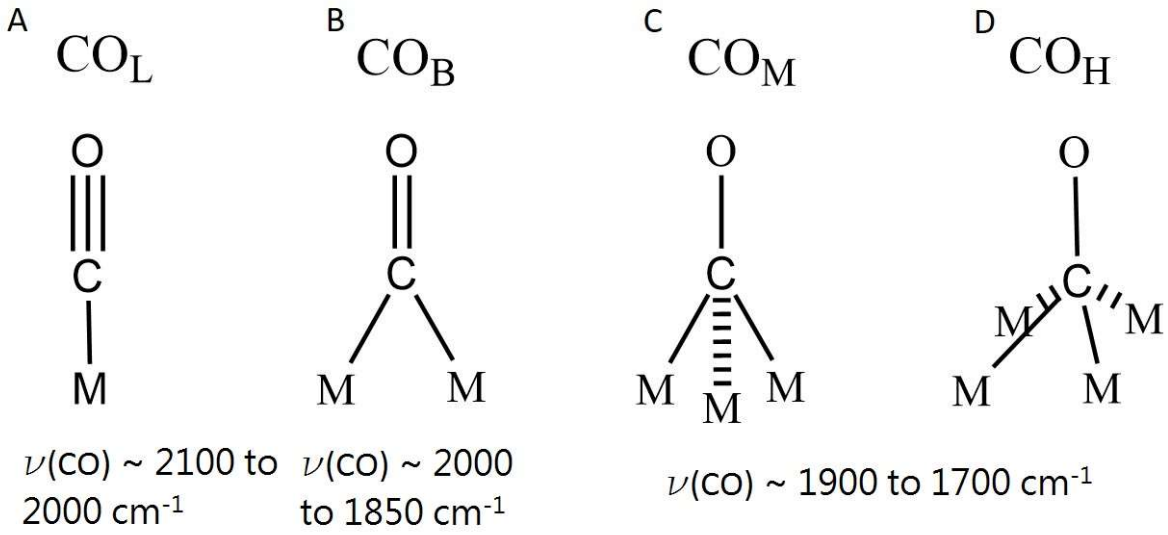


Figure 1-7 Typical frequency ranges for the CO stretching mode for carbon monoxide adsorbed in A: Linear-bonded, B: Bridge-bonded, C: Multiple-bonded and D: Hollow-bonded sites.

The adsorption strength of the CO with the surfaces is reflected in the vibrational frequency of CO bond-stretching vibrations. The weaker the adsorption on the surface, the stronger the CO bond and the higher the IR

wavenumber, and *vice versa*. Therefore, different numbers of metal sites binding CO give different ν(CO) peak wavenumbers in infrared spectroscopy. Figure 1-7 shows the different bonding modes by one or multiple sites and expected frequency ranges in wavenumber units for the ν(CO) stretching modes.

1.3.2 *In situ* IR spectroscopy of metal electrodes and nanoparticles

1.3.2.1 On Metal electrodes

Measuring IR spectra at a metal electrode is challenging. Since metal electrodes are not optically transparent, the spectrum is usually collected by IR light reflected from the surface of the electrode. There are two major reflection modes of infrared spectroscopy are widely used to investigate electrocatalysis on metal surfaces:

(i) External reflection mode

(ii) Internal reflection mode

In external reflection spectroscopy (also known as IRAS – Infrared reflection absorption spectroscopy), the electrode is pressed onto a IR transparent window (thus leaving a thin layer of electrolyte approx. 1-2 μm thick).[44] In this type of measurement, infrared radiation is shed on the electrode through an IR transparent window (e.g. CaF_2 in most cases) and the electrolyte solution, and

the reflected beam is detected, as shown in Figure 1.8A. One of the biggest advantages of IRAS is that the choice of material of the working electrode is flexible. It can be either well defined single crystals or polycrystalline materials as long as it reflects the IR beam.[45] Thanks to the development of Fourier transform infrared (FT-IR) spectrometers, IRAS has enough sensitivity to detect sub-monolayers on metal surfaces and has been used widely in surface science studies in the vacuum and gas phases. However, there are some disadvantages when IRAS is used to study a solid / solution interface: the presence of diffusion limitations in the thin layer separating the electrode and the window (for example, gas bubble formation can seriously disturb the acquisition of the IR signal), and the strong IR absorption bands of H_2O (a bending mode at ca. 1650 cm^{-1} and a stretching mode at ca. 3400 cm^{-1}), can overlap with and obscure the other signals. Furthermore, this technique poses a serious problem when it is used for *in situ* dynamic studies, which arises from the use of thin solution layer. One is the slow response of a thin layer cell with respect to the externally applied potential modulations due to the large solution resistance.[46] The other is the limited mass transport between the thin solution layer and the reservoir, which makes monitoring of real reactions difficult, because the reactant molecules in the thin layer are consumed quickly and the reaction products are accumulated during the recording of spectra.

The other mode is Internal Reflection mode. It is a variation of the experimental mode commonly known as Attenuated Total Reflectance (ATR). Figure 1-8B shows electrochemical cells and optical arrangements of the ATR setup.

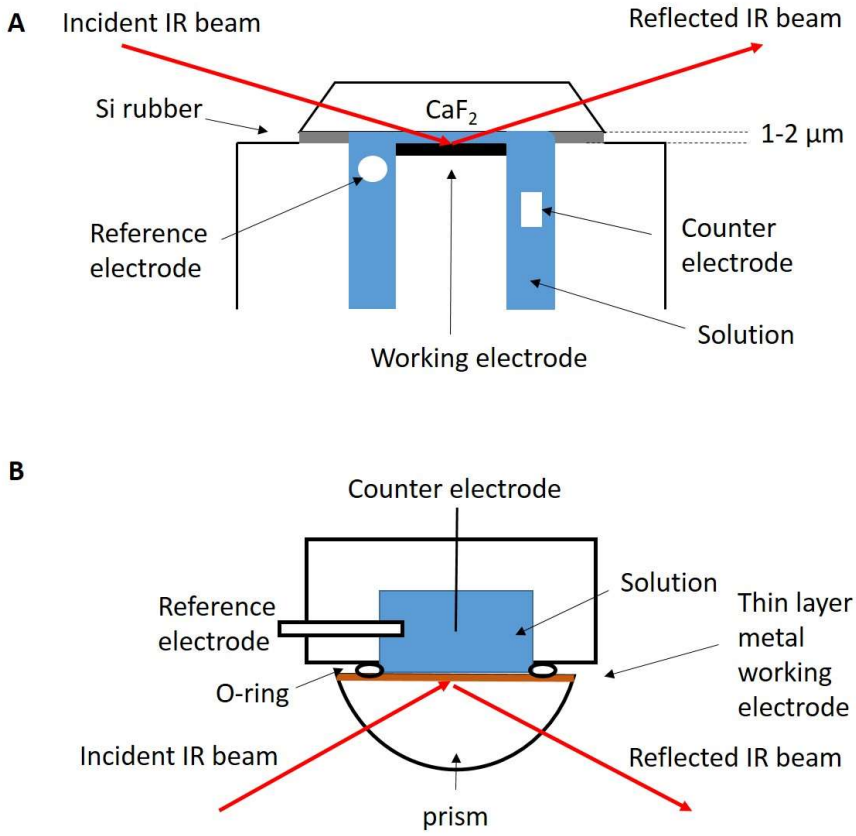


Figure 1-8 Electrochemical cells and optical arrangements used for *in situ* characterization of electrode / electrolyte interfaces with A) IRAS and B) ATR-SEIRAS. Reproduced from reference 46.

This technique uses the total internal reflection occurring when a light beam reaches the interface between two materials with different refractive indexes. An evanescent wave is then generated, which travels across the interface enabling the study of the external side of the internal reflection element (IRE) (also generally called a prism). If a thin metal layer (ca. 100 nm) with nanoscale

roughness deposited onto the IRE is used as the working electrode, a surface enhancement takes place, which increases the intensity of recorded signals.[47] In the mid-infrared region: molecules on metal surfaces show infrared absorption 10–1000 times more intense than would be expected from conventional measurements without signal enhancement from the nano-roughened metal.[48,49] This approach to ATR is called surface enhanced IR spectroscopy (SEIRAS). The main advantage of SEIRAS over IRAS is that only a very short time (sometimes in the nanosecond scale) is required for collecting the spectra for SEIRAS. IRAS spectra are averaged over many scans to improve the signal to noise ratio. With SEIRAS only a handful of scans are needed, and in certain cases just one scan can give the data one needs. This makes SEIRAS potentially useful for time-resolved *in situ* monitoring of electrochemical reactions. This means that structural information can be gathered for the species being formed in an electrochemical experiment, aiding the understanding of the mechanism of reaction. Besides, this technique features several other advantages: there are minimal contributions from bulk water and no diffusion limitations because a larger solution volume can be supplied in contact with electrode.

1.3.2.2 With nanoparticles

The techniques (IRAS and SEIRAS) used to study bulk metal electrodes can be extended for the study of nanoparticles by simply depositing the nanoparticles onto the bulk electrode surface. However, for studying *in situ*

spectroelectrochemistry of electrocatalytic reactions in aqueous solution such as formic acid or methanol oxidation in acidic or alkaline solutions, IRAS is not ideal. This is because the strong IR absorption by water may overlap with the other species either in solution or adsorbed on the nanoparticles. Furthermore, the slow diffusion in an IRAS cell also causes inefficient mass transport during catalysis.

SEIRAS seems like a promising technique for *in situ* dynamic IR studies. A nanocatalyst ink can be deposited on the underlayer electrode which is covered on the IRE surface by a simple drop-casting method for SEIRAS studies.[50,51] However, when using SEIRAS to study nanoparticles, it is very important to avoid contributions in the spectra from species on the underlayer metal electrode. By drop-casting the catalyst ink on an underlayer metal electrode, it is impossible to prevent contact between the electrode and the solution. Although, Au is mostly used as the material of electrode because it is not strongly adsorbing species such as CO and H_2O but many other species do adsorb on Au.[52] Furthermore, the large size of the support material means that the distance between the metal nanoparticles and the Au underlayer electrode is too great for the surface enhancement effect, and so the IR signal is very weak.

In this Thesis, a multiple-bounce ATR technique is used to overcome the limitations in *in situ* spectroelectrochemical investigation on supported nanocatalysts by IRAS and SEIRAS. This will be introduced in chapter 2.

1.4 Electrochemical conversion of carbon dioxide: enzymes and metals

1.4.1 Formation of hydrocarbons from electro-reduction of CO

Carbon dioxide (CO_2) is a significant contributor to the greenhouse effect. The increasing concentration of CO_2 in the atmosphere is causing global climate change and affects not only the biogeochemical carbon cycle but also human economies. Besides, carbon dioxide is a potential carbon resource and it is abundant on Earth. Therefore, the conversion of CO_2 into useful products and chemicals seems to be necessary and attractive. There are several ways to tackle the CO_2 issue including CO_2 capture[53], CO_2 storage[54,55] or conversion into valuable chemicals.[56–58] The fixation of CO_2 molecules by electrochemical reduction (artificial photo-synthesis), where electrical energy is supplied to establish a potential between two electrodes for reducing CO_2 into the hydrocarbon feedstock is one of the most popular options.[56,59–62] However, CO_2 reduction into hydrocarbons is expected to be very challenging, due to the necessary multiple number of proton-coupled electron transfer steps.[63] The electrochemical reduction of CO_2 by transition metal electrodes was studied for the first time by Royer and has been studied very intensively in the last two

decades.[57] These studies have been summarised into several review articles on CO_2 electrochemical reduction.[55,63–66]

Transition metals and their associated compounds, metal complexes, have been widely tested for their activities towards electrochemical reduction of CO_2. The rationale behind this choice lies in the vacant orbitals and high energy d electrons, which can participate in the bonding between the metal and the CO_2 for adduct formation and can cause the desorption of the reduction products.[66]

Table 1-2 Summary of thermodynamic potentials of CO_2 reduction to various products.[67]

$CO_2 + 2H^+ + 2e^- \rightarrow CO + H_2O$	E^0 = -0.53 V
$CO_2 + 2H^+ + 2e^- \rightarrow HCOOH$	E^0 = -0.61 V
$CO_2 + 4H^+ + 4e^- \rightarrow HCHO + H_2O$	E^0 = -0.48 V
$CO_2 + 6H^+ + 6e^- \rightarrow CH_3OH + H_2O$	E^0 = -0.38 V
$CO_2 + 8H^+ + 8e^- \rightarrow CH_4 + H_2O$	E^0 = -0.24 V

Electrochemical reduction of CO_2 can proceed through $2e^-$, $4e^-$, $6e^-$, and $8e^-$ reduction pathways in gaseous, aqueous, and non-aqueous phases at both low and high temperatures which is summarised in Table 1-2.[67] The major products from CO_2 reduction are carbon monoxide (CO), formic acid (HCOOH) or formate

($HCOO^-$) in alkaline solution. Oxalic acid ($H_2C_2O_4$) or oxalate ($C_2O_4^{2-}$ in alkaline solution), formaldehyde (CH_2O), methanol (CH_3OH), methane (CH_4), ethylene (CH_2CH_2), ethanol (CH_3CH_2OH), as well as others depending on the different material composition of the catalyst.[68–70]

1.4.2 Copper as CO_2 reduction catalyst

Among the various materials, copper (Cu) is one of the most promising metals for catalysing CO_2 reduction to form hydrocarbons.[66,71] A typical product distribution as a function of potential, as measured by Hori et al. with a Cu electrode, is shown in Figure 1-9.[72] Methane and ethylene, which can be used as the precursors for chemical synthesis in industry, are the main products at sufficiently negative potentials.

At less negative potentials, dihydrogen, formic acid, and carbon monoxide are dominant products (Figure 1-9). The products of CO_2 reduction by Cu catalysts have a very wide distribution. The product distribution is not only dependent on the potentials but also on the electrolyte composition, the temperature and the surface structure as summarised in Table 1-3 from a survey of the literature.[73] As reported by Hori and coworkers, the CO_{ads} intermediate was first detected by infrared spectroscopy at a Cu electrode at -0.9 to -1.0 V in CO_2 saturated electrolyte solution.[74] That is so far the only report of CO adsorption during reduction of CO_2 by copper, as measured by IR spectroelectrochemistry. This suggests that CO_2 is first reduced to CO on the Cu surface as an intermediate.

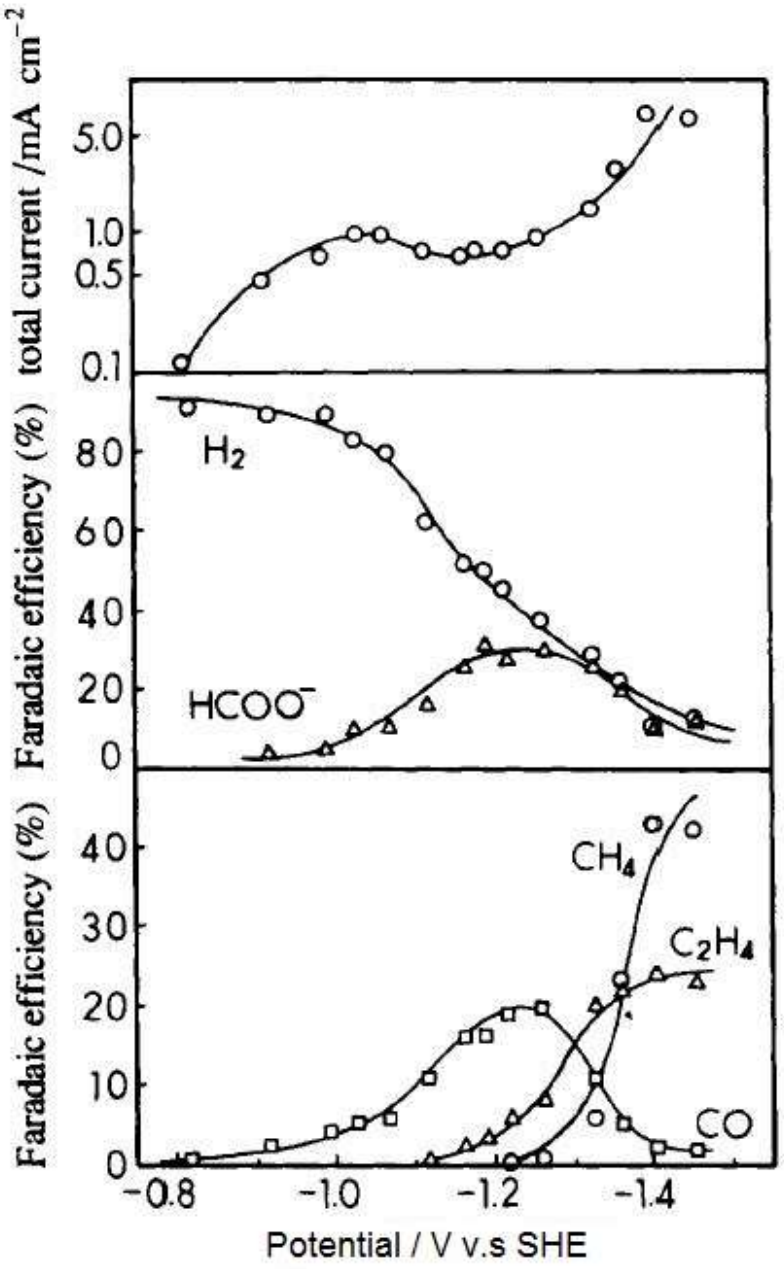


Figure 1-9 Experimentally determined current and product distribution at a copper electrode. Product distribution and total current produced as a function of applied potential (*vs* reversible hydrogen electrode, RHE) in the electrochemical reduction of CO_2 at a copper electrode in 0.1 M $KHCO_3$ (pH 6.8) at 18.5 C, as measured by Hori et al.[72] Reprinted with permission.

A similar CO_{ads} species was also found by surface-enhanced Raman spectroscopy (SERS) in the low potential region in CO_2 saturated solution by Ito and the coworkers.[75]

This confirmed that CO is formed at a copper electrode during CO_2 reduction as the reactive intermediate and further reduced to hydrocarbons and methanol.

Table 1-3 Faradic efficiencies of various products from electrochemical reduction of CO at a Cu electrode. Reprinted from reference 72 with permission.

Electrolyte	pH	Potential V vs. SHE	Faradaic efficiency/ %						
			CH_4	C_2H_4	EtOH	n-PrOH	HCHO	H_2	Total
Current density: 2.5 mA cm^{-2}									
Phosphate[a]	6.1	−1.18	9.3	2.3	0.0	0.0	0.2	81.1	92.9
$KHCO_3$[b]	9.6	−1.40	16.3	21.2	10.9	1.5	0.1	45.5	95.5
Current density: 5.0 mA cm^{-2}									
Phosphate[a]	6.0	−1.21	16.8	1.7	0.0	0.0	0.02	75.4	93.9
$KHCO_3$[b]	9.6	−1.45	16.2	5.5	2.7	0.3	0.03	65.4	90.1
KOH[c]	12.9	−1.47	1.0	14.1	5.8	1.1	0.05	70.7	92.8

[a]Phosphate buffer solution containing KH_2PO_4 (0.17 mol dm^{-3}) and K_2HPO_4 (0.03 mol dm^{-3})
[b]$KHCO_3$ (0.1 mol dm^{-3}).
[c]KOH (0.1 mol dm^{-3})

Moreover, CO electro-reduction has shown a similar potential dependence and hydrocarbon distribution as for the CO_2 electro-reduction.[72,74,75] The results suggest that CO is an intermediate of the electro-reduction of CO_2 to hydrocarbons and that the reduction of CO_2 to CO is the rate-determining step. The thermodynamic potential of CO_2 reduction to CO is close to -0.53 V (Table 1-2).[67] However, as suggested by spectroelectrochemical results, the formation

of CO from CO_2 electro-catalytic reduction on a copper electrode requires around -0.9 V or even more negative overpotential. Therefore, the efficiency of CO_2 reduction is mainly limited by the slow rate for the formation step of CO on Cu.

1.4.3 CO_2 reduction catalysed by a biological catalyst: carbon monoxide dehydrogenase

CO_2 reduction to hydrocarbons has been introduced in the previous section. Despite the fast reduction rate of CO to hydrocarbon chemicals, because of the high overpotential requirement for CO_2 reduction to CO, copper is not efficient enough to act as a catalyst for converting CO_2 into useful carbon feedstocks. In nature, a group of enzymes called carbon monoxide dehydrogenases (CODHs) have been reported as very active catalysts for CO / CO_2 conversion with nearly zero overpotential.[76–78] Carbon monoxide dehydrogenases are a group of bidirectional enzymes that can oxidise carbon monoxide to carbon dioxide or reduce carbon dioxide to carbon monoxide.[79] From previous crystallography studies, CODHs are known to contain five FeS clusters. One D-cluster is shared between two CODH monomers in the middle of two subunits. At about 10 Å from this centre, each monomer binds a B-cluster that is also located at the subunit interface. C-clusters (the catalytic centres) are buried deeper, being located at the interface of the three domains that compose each CODH monomer and lie at about 11 Å from the closest B-cluster that is located in the other subunit (Figure 1-10).[80–82] Unlike the B-clusters and D-clusters which are standard

[4Fe–4S] cubanes, the structure of the C-cluster is unprecedented: it contains a Ni and an atypical Fe ion that is not a part of the FeS cluster and is thought to correspond to the spectroscopically unusual Fe_u, also known as Ferrous Component II or FCII (Figure 1-10).[80–82]

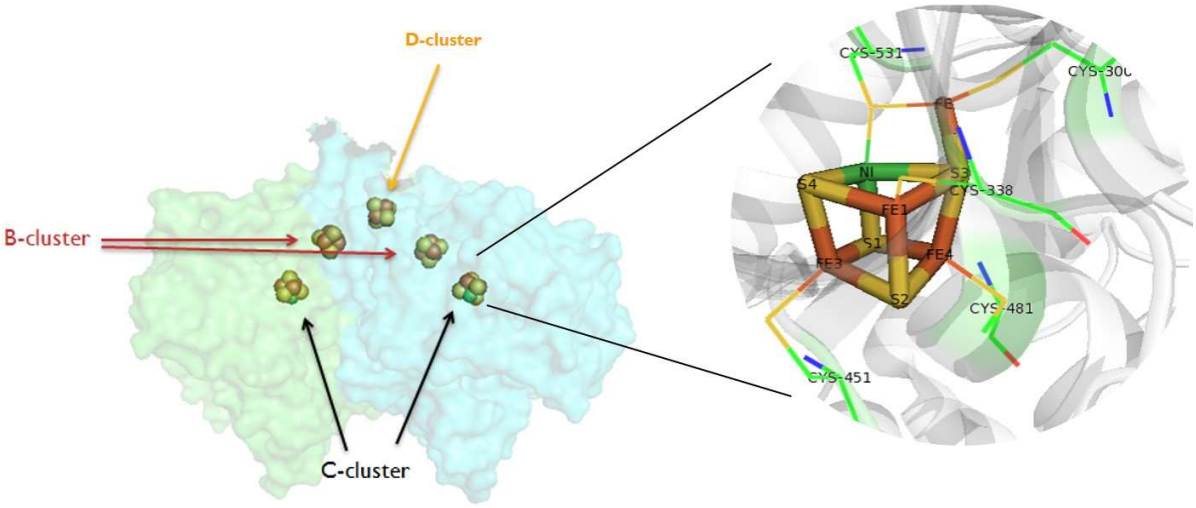


Figure 1-10 Overall architecture of the homodimeric CODH, highlighting the locations of all 5 cofactors. Figure prepared using pymol from data in PDB file 3I39 for the X-ray crystallographic structure of CODHII from *Carboxydothermus hydrogenoformans*.

The anaerobic C-cluster has been shown, by means of electron paramagnetic resonance (EPR) spectroscopy, to exist primarily in one of three mechanistically significant electronic states, interchangeable upon varying the solution potential - C_{ox}, C_{red1} and C_{red2}.[77,78] It has been shown that CO_2 and H^+ substrates bind to C_{red2}, and following reduction of CO_2 to CO, the two electrons are transferred from the C-cluster, resulting in the C_{red1} state with CO. The

midpoint potential of C_{red1} / C_{red2} states is close to -530 mV which is very close to the thermodynamic potential of CO_2 reduction to CO.

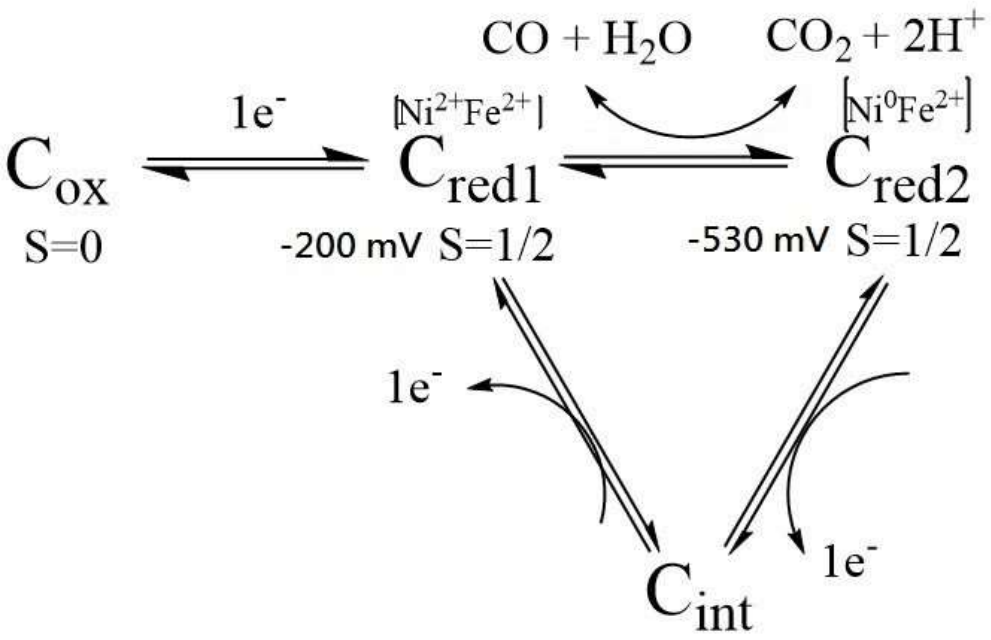
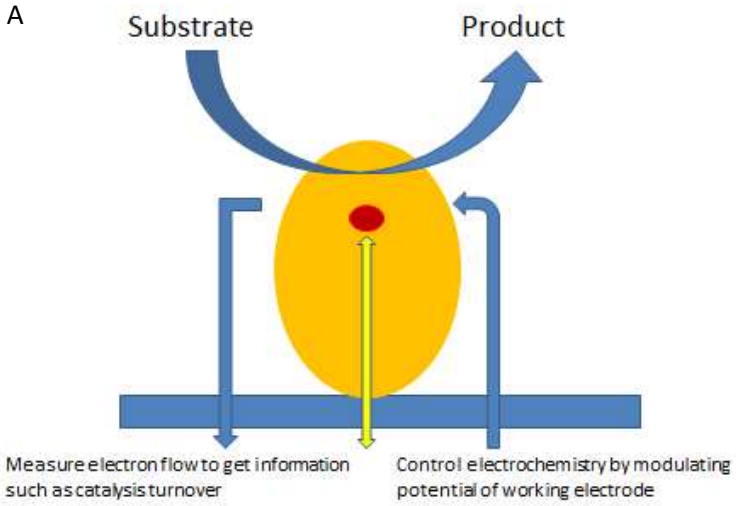


Figure 1-11 States proposed to be involved in the catalytic cycle of CODH I*Ch*. The C_{ox} state is an inactive, oxidised state that is reduced at potentials below -200 mV to the catalytically active C_{red1} state.

Besides, the midpoint potential of C_{ox} / C_{red1} is at -200 mV where CO can react with C_{red1} for oxidation of CO, resulting CO_2 and C_{red2} (Figure 1-11). A possible strategy for using CODHs as electro-catalysts for conversion of CO_2 to CO has been illustrated by Armstrong and coworkers.[83] They have discussed the immobilization of CODH enzymes on pyrolytic graphite "edge" (PGE) electrodes and shown that the electro-catalytic conversion of CO_2 on these electrodes is reversible. This technique is called protein film electrochemistry (PFE) (Figure 1-12A).

A



B

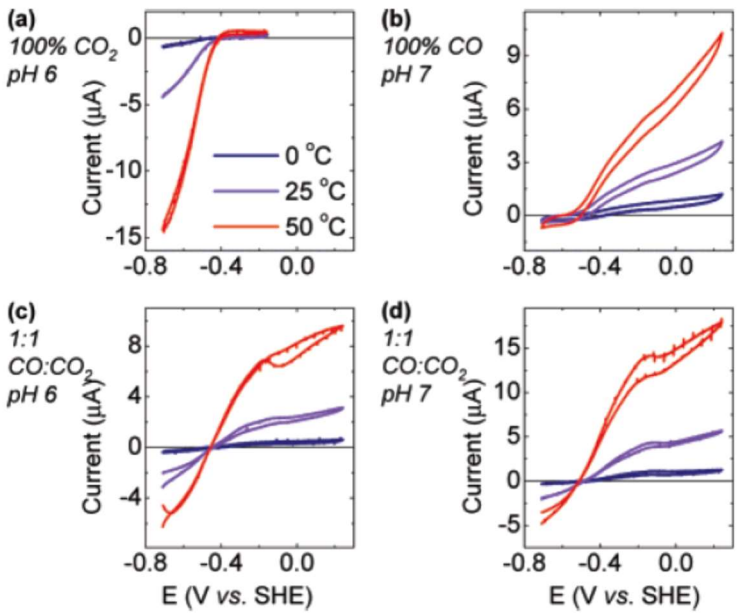


Figure 1-12 A: Protein film electrochemistry involves immobilisation of proteins by adsorbing a sub mono-layer of protein on the working electrode. By measuring electronic current and controlling electrochemical potential, the enzyme catalytic chemistry can be studied. B: The protein film voltammograms (shows the correlation between catalytic current measured and the potential (E) applied at working electrode. SHE stand for standard hydrogen electrode) of CODH electro-catalysing CO / CO_2 conversion. Reprinted from reference 83 with permission.

PFE allows potential control of the enzymes and direct electron transfer between the electrode and the enzymes. By measuring changes of current with applied potential, we can get many clues about the catalytic behaviour of the enzymes (Figure 1-12A). For example, CODH immobilized on an electrode can reduce CO_2 to CO by applying a potential lower than the midpoint potential of C_{red1} / C_{red2}.[84] Unlike metal surfaces, these highly efficient active sites can bind and stabilise the intermediate due to the precisely positioned functional groups and thereby lower the overpotential, or kinetically couple the formation and onward reaction of the intermediates. Moreover, CODH seems to avoid the well-known problem of CO poisoning, which could inspire the development of designed biomimetic materials for CO_2 reduction.

The CODH I studied in this Thesis is CODH I from *Carboxydothermus hydrogenoformans*. Prior electrochemical characterisation of this enzyme is summarised in the voltammograms of CO oxidation and CO_2 reduction by CODH I (Figure 1-12B).[84] This offers a reference for the electrochemical application of CODH I in the later chapters

1.4.4 Design of a cascade system for hydrocarbon formation via CO_2 reduction

Copper is the most promising metal that is able to catalyse CO_2 and CO reduction to favour hydrocarbons such as methane, ethylene, formic acid and methanol. As discussed in section 1.4.2, the conversion between CO_2 and CO on

a Cu electrode requires a high overpotential which limits the turnover rate of CO_2 electro-reduction.

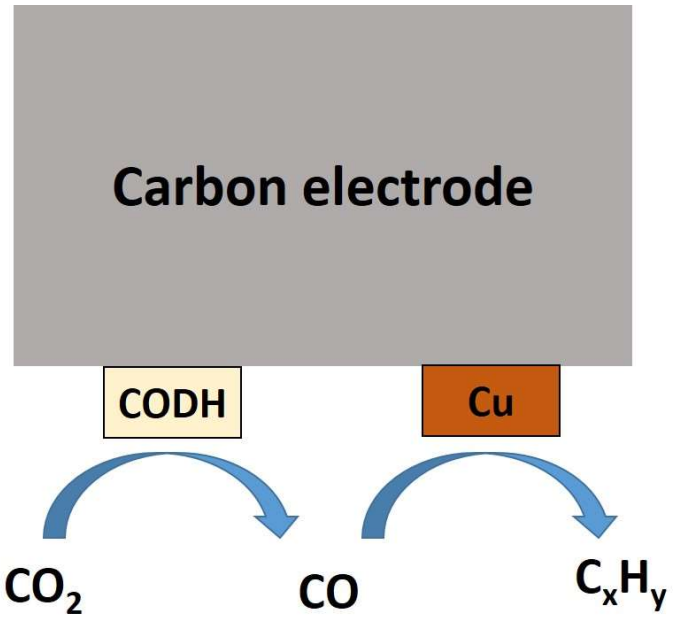


Figure 1-13 A schematic illustration for the composite electrocatalyst system for CO_2 reduction to hydrocarbons. CODH accelerates the rate of CO formation from CO_2 reduction, then relays CO to Cu for hydrogenation to hydrocarbons.

On the contrary, CODH has a high catalytic activity for CO_2 / CO conversion with midpoint potential around -0.53 V vs SHE, which is very close to the thermodynamic potential of CO_2 reduction to CO. The idea here is to assemble a composite system combining Cu nanoparticles and CODH enzymes. This allows the rate-determining step, CO_2 reduction to CO, to be accelerated by CODH and hopefully increase the whole turnover rate of CO_2 reduction to the final products. The details of this system will be introduced in chapter 6.

1.5 Aim of this Thesis

In this study, the use of a new Attentuated Total Reflectance (ATR)-IR spectroelectrochemical approach for studying supported metal nanocatalysts was demonstrated to investigate methanol and formic acid electro-catalytic oxidation (CO activation plays as an important role in both reactions) on carbon supported Pd catalysts. In chapter 6, the possibility of a new composite catalyst system for electrochemical reduction of CO_2 to hydrocarbons is demonstrated by combining metal nano-particle and enzymatic catalysts.

Overall this Thesis provides insight into the formation and activation of CO at metal sites during electrocatalytic reactions which are relevant to energy technologies.

Chapter 2

Theory and Methodology

2.1 Electrochemical Theory and Methods

Electrochemistry is the branch of chemistry that studies chemical reactions involving transfer of electrons at the interface of an electrode and an electrolyte. Therefore, electrochemical techniques are widely used to study electrocatalytic reactions since the reactions are relied on electrons transfer between the reactants, electrocatalysts and the electrode. This section introduces the fundamental theory of electrochemistry and the electrochemical methods used in this work.

2.1.1 Three electrode system

An electroactive species is one that can be oxidised or reduced at an electrode. The potential of the working electrode (WE) controls which electroactive species will react and which will not. Metal working electrodes are recognised to be polarisable, which means that the potentials of them can be easily changed when a small current flows. Reference electrodes (RE) such as calomel (SCE) or silver / silver chloride (Ag / AgCl) are considered as nonpolarisable since their potential does not vary much unless a significant current is flowing.

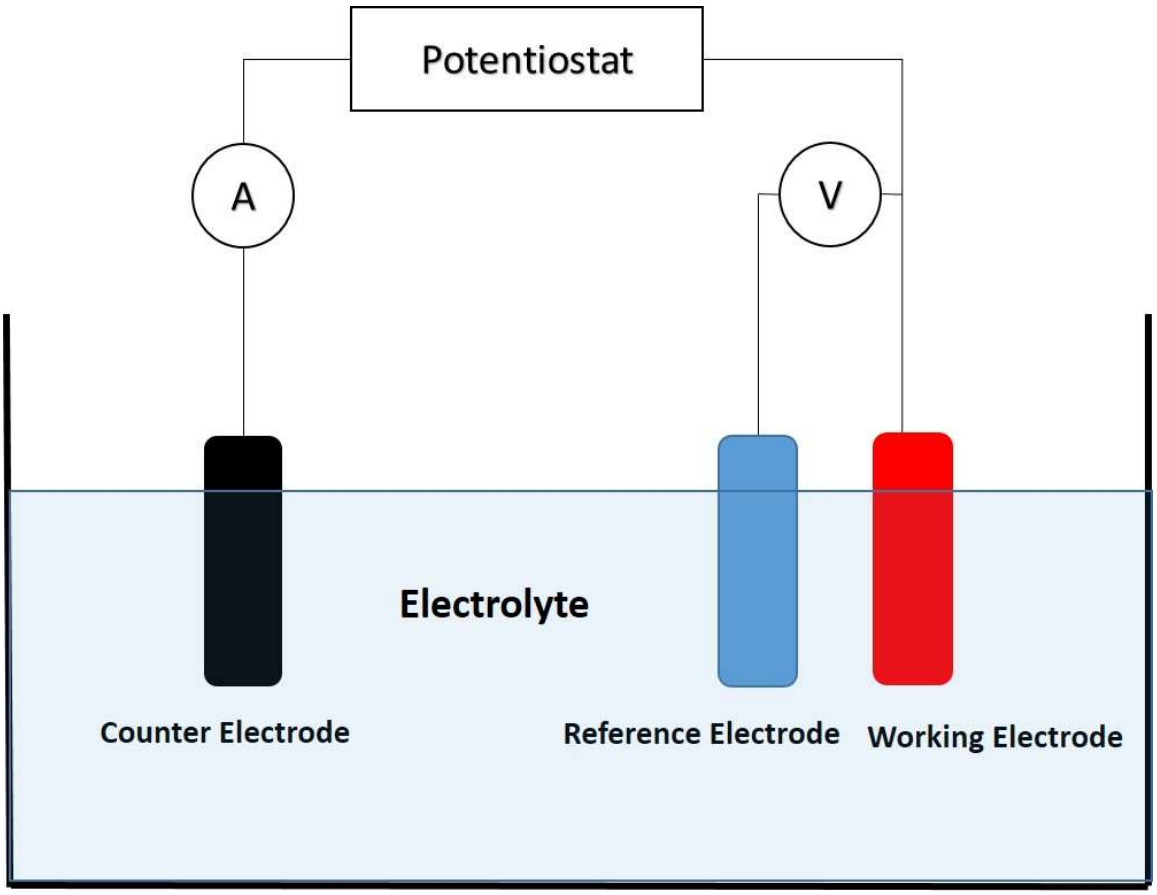


Figure 2-1 A schematic circuit diagram of a three electrode system. In a three-electrode system, a potential at the working electrode is imposed with respect to the reference electrode and the counter electrode is allowed to equalise the current from the reaction at the working electrode.

Ideally, we want to measure the potential of a polarisable working electrode with respect to a nonpolarisable reference electrode. When electrocatalysis occurs at the working electrode, the significant catalytic current will pass from the working to the reference electrode. Therefore, the potential between the working electrode and the reference electrode will be affected by the ohmic potential drop between these two electrodes due to the current and the solution resistance, R, of the electrolyte in the electrochemical cell (Equation 2-1).

Moreover, the reference potential will deviate from the standard potential caused by changing concentration of the redox pair in the RE if current flows through the RE. To avoid the potential of the working electrode being affected, a third electrode is required. The third electrode, known as the auxiliary electrode or counter electrode (CE) is used as the current-supporting partner of the working electrode as shown in Figure 2-1. Current flows between the working electrode and the counter electrode.

Only negligible current flows through the reference electrode. In controlled-potential electrochemical experiments, the voltage difference between the working and reference electrodes in a three electrode system is regulated by an external electronic device called a potentiostat.

$$E_{ohmic} = IR \quad \text{.....(2-1)}$$

2.1.2 Electrochemical responses

Electrochemical responses (signals) are divided into two types:

(i) Faradaic signals are caused by changing of the redox state of the reactant, and follow Faraday's law (for reaction of 1 mole of analyte, the amount of charge required is equal to n x 96485 C, where n is a number of electrons involved in a single electrochemical reaction). The Faradaic current equals the rate of the electrode reaction dN / dt (change of the number of electrons with time), which is on the other hand proportional to the concentration of the investigated

substance (in solution or at the electrode surface if the substance is adsorbed). Faradaic current is measured when charge is flowing across the electrode–solution interface. An investigated substance releases electrons by oxidation, while it accepts electrons from the electrode to undergo reduction. Since the current, I is the rate of electron flow, the number of moles, N of generated product from the reaction can be calculated using this relation (Equation 2-2):

$$I = nF\frac{dN}{dt} \quad \text{(2-2)}$$

Where F is the Faraday constant and n is a number of electrons involved in a single electrochemical reaction.

(ii) A non-faradaic signal could arise from different incidents such as adsorption / desorption, movement of ionic species in solution and structural changes at the interface. Double-layer charging on the electrode surface is commonly responsible for the non-faradaic current observed in voltammetric measurements. When a potential is applied across the interface, different charges will accumulate on the electrode and solution sides, called the electrical double layer as shown in Figure 2-2. Several layers of solution can be formed on the electrode surface and this electrode-solution interface can act as a capacitor. The capacitive current is derived from the structure of the electrode-solution interface, which is considered as capacitor constituted of two charged surfaces

(metal-solution) separated by dielectric medium (e.g. water layer). The charge of this capacitor is given by Equation 2-3.

$$Q = EC_d \quad \text{(2-3)}$$

where C_d is a differential capacitance of the interface and E is a potential difference of capacitor.

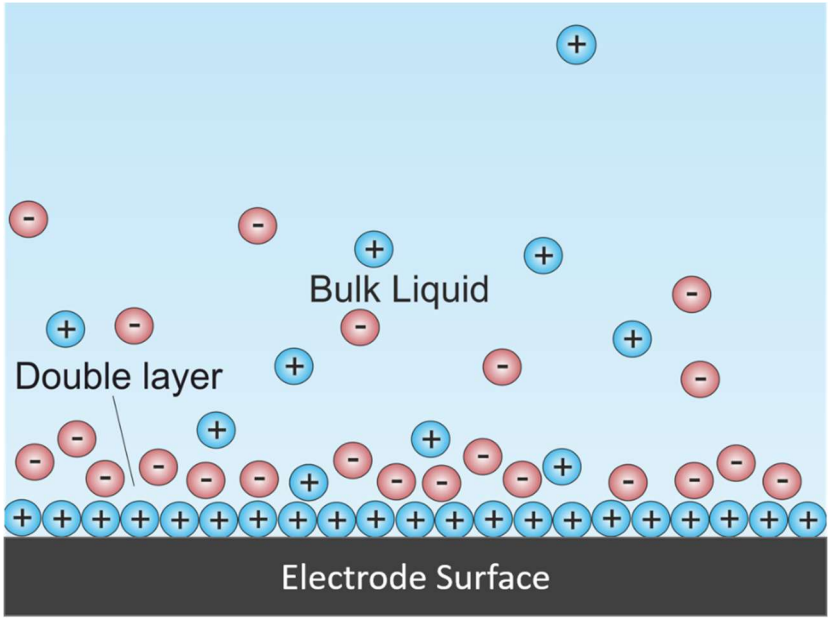


Figure 2-2 A diagram representative of double layer on the electrode-solution interface. Positive charge reflects deficiency of electron on electrode.

At a given potential, the electrode current can be given as the sum of two factors: capacitive current (non-faradaic) and the faradaic current. Faradaic current is equivalent to zero when at a given potential electron transfer does not occur to or from the electrode. The other current observed is capacitive current, caused

by different processes that do not involve electron transfer across the electrode surface, so called non-faradaic processes.

2.1.3 Cyclic voltammetry

In cyclic voltammetry, a triangular waveform of the type shown in Figure 2-3 is applied to the working electrode.

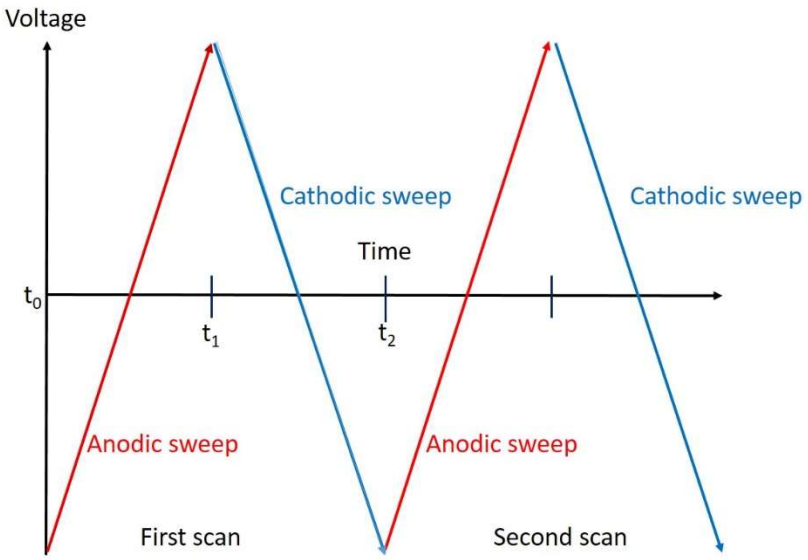


Figure 2-3 Waveform for cyclic voltammetry. The potential is applied as a function of time during cyclic voltammetry.

After the application of a linear voltage ramp between t_0 to t_1, the ramp is reversed to bring the potential back to its initial value at time t_2. The cycle may be repeated many times.

Figure 2-4 shows a cyclic voltammogram of 1 mM $K_3Fe(CN)_6$ in water on a glassy carbon working electrode recorded at a rate of 50 mV s^{-1} as an example of a typical cyclic voltammogram of a reversible redox couple. The result shows the

redox couple of $Fe(CN)_6^{3-}$ / Fe $(CN)_6^{4-}$. It can be seen that the anodic current increases in magnitude as the reduced species ($Fe(CN)_6^{4-}$) of the redox couple in solution is oxidised as the potential approaches the anodic peak potential (E_{pa}). At the anodic peak, the rate of the oxidation is maximised and the current measured at this point is i_{pc}.

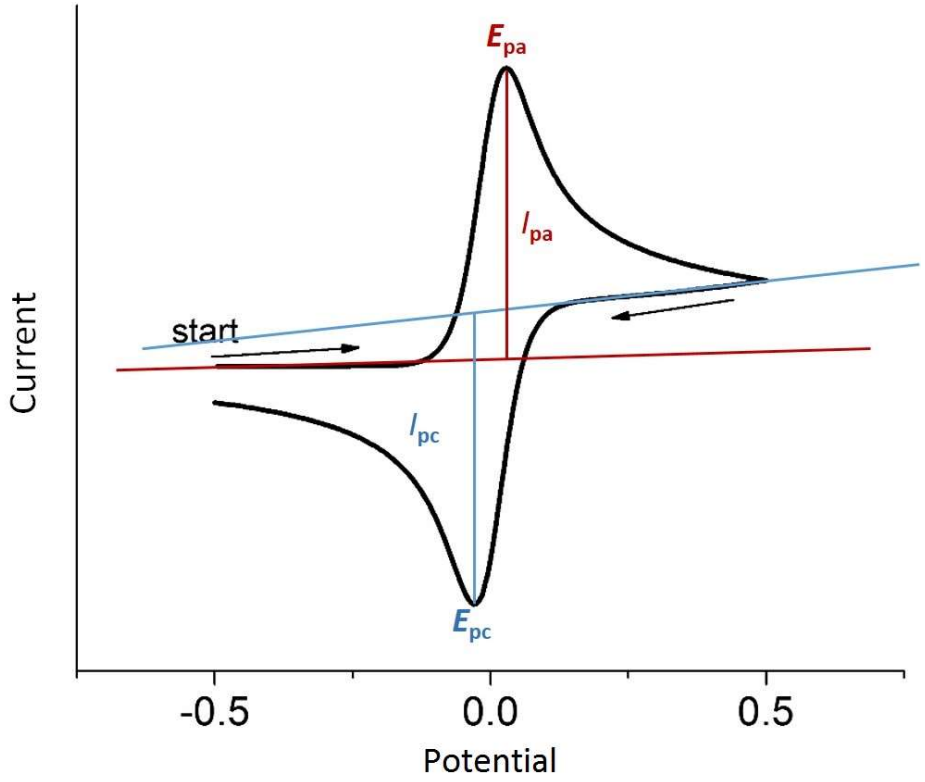


Figure 2-4 A cyclic voltammogram of 1 mM $K_3Fe(CN)_6$ in water on a glassy carbon working electrode recorded at a rate of 50 mV s^{-1}.

After E_{pa}, the oxidation current decreases due to effects of diffusion control. At this point the concentration of the electroactive species near the electrode has decreased to zero and the rate of diffusion to the electrode is slower than the rate of electron transfer. Further current flow requires diffusion of species from

further and further away, at a correspondingly slower and slower rate, leading to a fall-off in the current. When the applied potential ramp is switched back, the process is reversed. The oxidised species ($Fe(CN)_6^{3-}$) is reduced and a cathodic current is measured. A midpoint potential can be determined in between E_{pa} and E_{pc} which corresponds to the standard reduction potential.

Cyclic voltammetry can therefore give information on the reduction potential and redox nature of the analyte. In a reversible system, the ratio of current from reduction and oxidation is nearly unity (i_{pa}/i_{pc} ~1) and the difference between E_{pc} and E_{pa} depends on the number of electrons passed in the process, n as shown in Equation 2-4:

$$\left|E_{pc} - E_{pa}\right| = 2.218\frac{RT}{nF} \quad \text{or} \quad \frac{57}{n}\ \text{mV at 298 K} \qquad \text{(2-4)}$$

2.1.4 Catalytic voltammetry and the rotating disk electrode experiments

In this work, cyclic voltammetry is used for investigating electrocatalytic reactions such as formic acid oxidation (FAO), methanol oxidation reaction (MOR) and CO_2 / CO interconversion. In catalytic voltammetry, the magnitude of the current is proportional to the concentration of electroactive species (reactant) and catalytic turnover rate (over a range of concentrations). The turnover rate depends on the relationship between driving force (dependent on the potential) and catalyst activity.

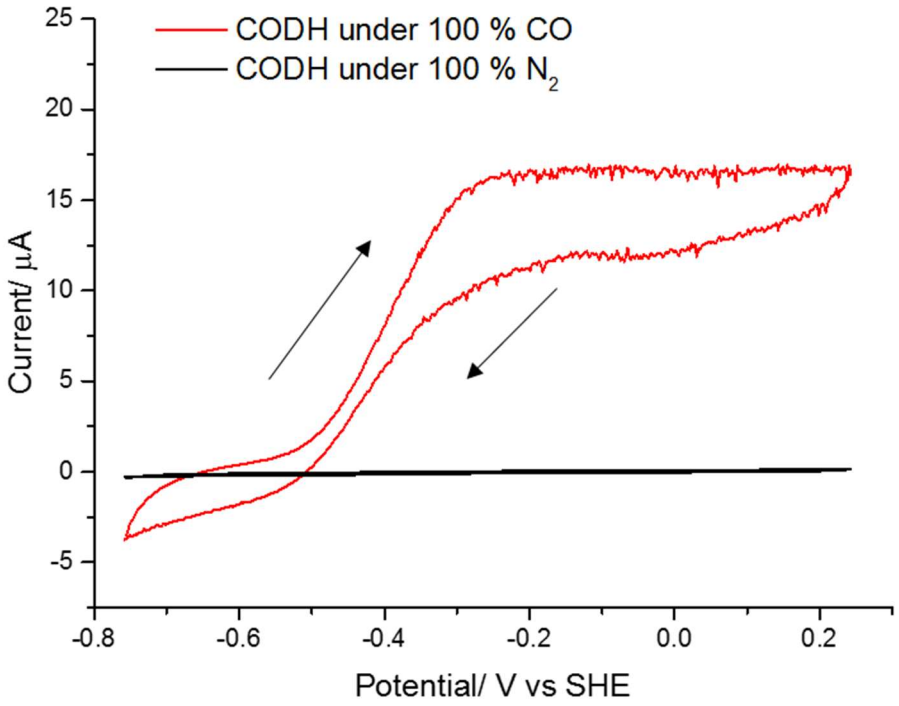


Figure 2-5 A catalytic cyclic voltammogram of carbon monoxide dehydrogenase (CODH) under a 100 % CO atmosphere at an electrode rotation rate of 1000 rpm and a scan rate of 10 mV s^{-1} . The potential dependent positive current comes from the electro-oxidation of CO to CO_2 by CODH. The catalysis is limited by mass transport when the potential is scanned above about -0.1 V, shown by the plateau in current.

Close to the onset potential for catalysis, the catalytic current magnitude should increase with electrochemical driving force. For the CODH electrode shown in Figure 2-5, the catalytic current increases with potential initially in the positive-going scan, but stops increasing once the potential reaches ca. -0.1 V because of mass transport limitations: the turnover rate becomes high enough to allow the rate of reactant (CO) consumption to be faster than the rate of reactant transport to the surface of electrode.

There are three ways for a reactant molecule to reach the surface of an electrode:

(i) diffusion through a concentration gradient

(ii) convection, which is the movement of the bulk fluid by physical means such as stirring or bubbling

(iii) migration, which is the attraction or repulsion of an ion by a charged surface.

In this Thesis, the working electrode used for electrochemical measurement is the rotating disk electrode (RDE) as shown in Figure 2-5, for which convection and diffusion control the flux of reactant to the electrode surface.

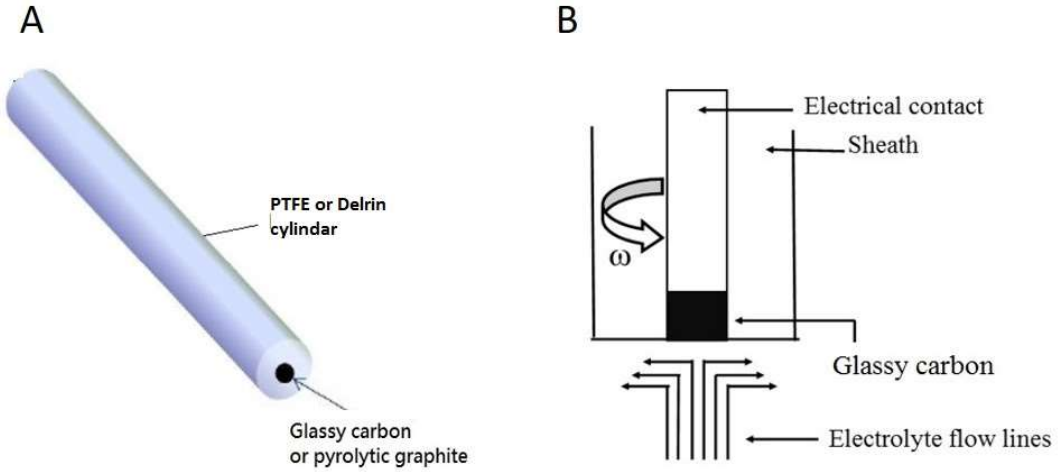


Figure 2-6 A: A schematic image of the rotating disk electrode. B: Laminar flow lines at the rotating disk during electrode rotation.

The inner black circle is the conductive electrode comprised of glassy carbon rod or pyrolytic graphite. The white surrounding material is the insulating sheath

made of Delrin or PTFE. The supported active metal under investigation is placed on the tip of the rotating disk electrode (Figure 2-6A).

When the electrode is spinning at about 1000 rpm, a vortex is established that brings analyte near the electrode very rapidly by convection (Figure 2-6B). At the peak potential, the reactant reacts very rapidly at the electrode, reducing the concentration right at the electrode surface near to 0. This resulting concentration gradient is shown schematically in Figure 2-7.

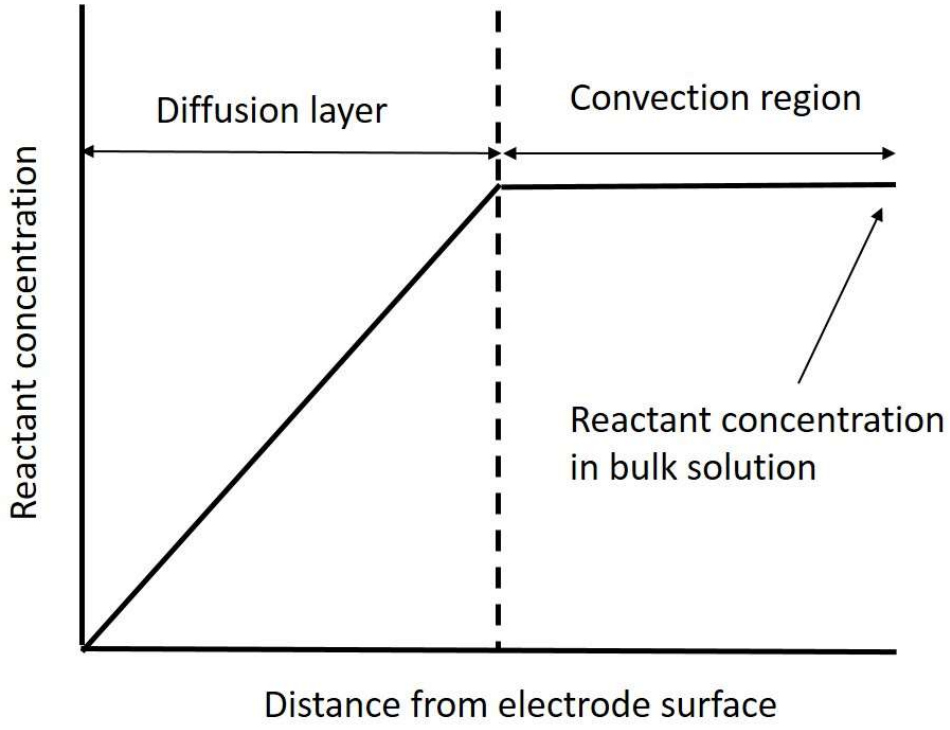


Figure 2-7 Schematic concentration profile of analyte near the surface of the rotating disk electrode when the potential is great enough to reduction the concentration of analyte near 0 at the electrode surface.

The reactant must travel the final short distance (usually 10 to 100 μm, depending on the solution) by diffusion. The faster the rotation rate, the thinner

the diffusion layer in Figure 2-7 and the greater the catalytic current. This increase in the rate means mass transport is less of a contributing factor to the overall reaction rate and leads to a change in the observed voltammogram as shown in Figure 2-8.

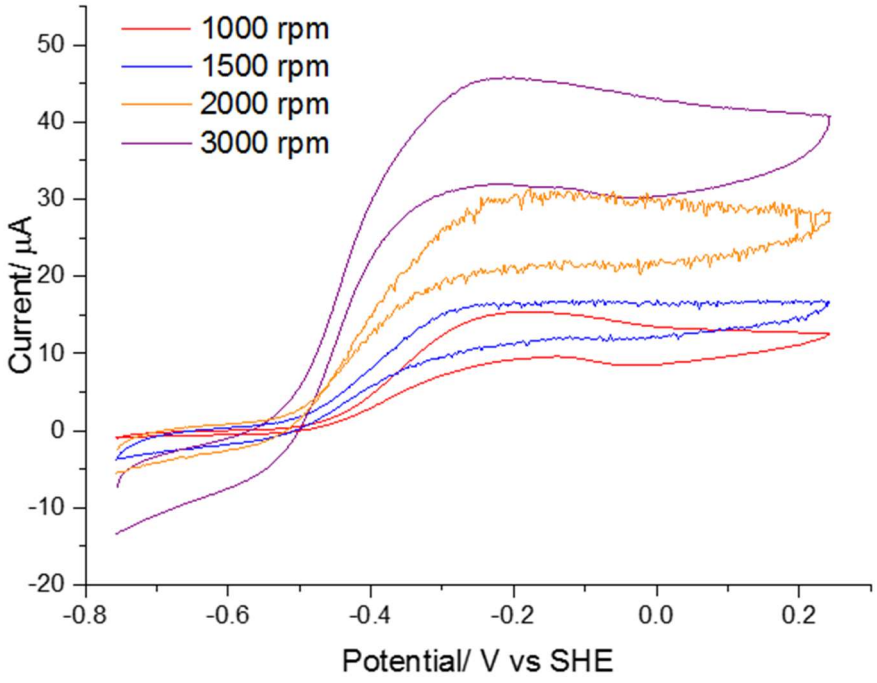


Figure 2-8 Cyclic voltammograms of CODH on a rotating disk electrode under a 100 % CO atmosphere at 10 mV s^{-1} scan rate with different electrode rotation rates.

Figure 2-8 shows cyclic voltammograms of CO oxidation by CODH with different rotation rates. The scans recorded with higher rotation rates show higher catalytic currents implying that the increase of rotation rate of the working electrode overcomes the mass transport limitation and results in higher turnover rates.

2.1.5 Electrochemical cell preparation

Figure 2-9 shows a schematic diagram of the apparatus used for electrochemical measurements in this Thesis. A 200 mL glass cell has three necks to hold each of the electrodes and two screw thread openings for gas inlet and outlet for saturating the electrolyte with gas. In the electrochemical experiments of Pd / XC-72, a glassy carbon working electrode (glassy carbon rod, 7mm diameter, Alfa Aesar) was used. A Pt wire counter electrode (0.127 mm diameter, Alfa Aesar) was used with a high enough surface area to support the current generated at the working electrode. Potentials were determined using a saturated calomel electrode (SCE) or a Ag / AgCl (3 M KCl) electrode as a reference, (both from ALS Co. Ltd). All potentials in this study refer to that of the standard hydrogen electrode (SHE), the relations being:

$$E_{SHE} = E_{\frac{Ag}{AgCl}} - 0.212 \text{ V at } 25\ ^{\circ}C$$

and $E_{SHE} = E_{SCE} - 0.244 \text{ V at } 25\ ^{\circ}C$.

For the experiments on CODH and Cu nanoparticles (details in chapter 6), a pyrolytic graphite edge (PGE) electrode is used as the working electrode. The mercurous sulfate electrode (MMSE) and Au wire were used as reference and counter electrodes respectively.

The potential of MMSE relative to SHE is as:

$E_{SHE} = E_{MMSE} - 0.640\,V.$

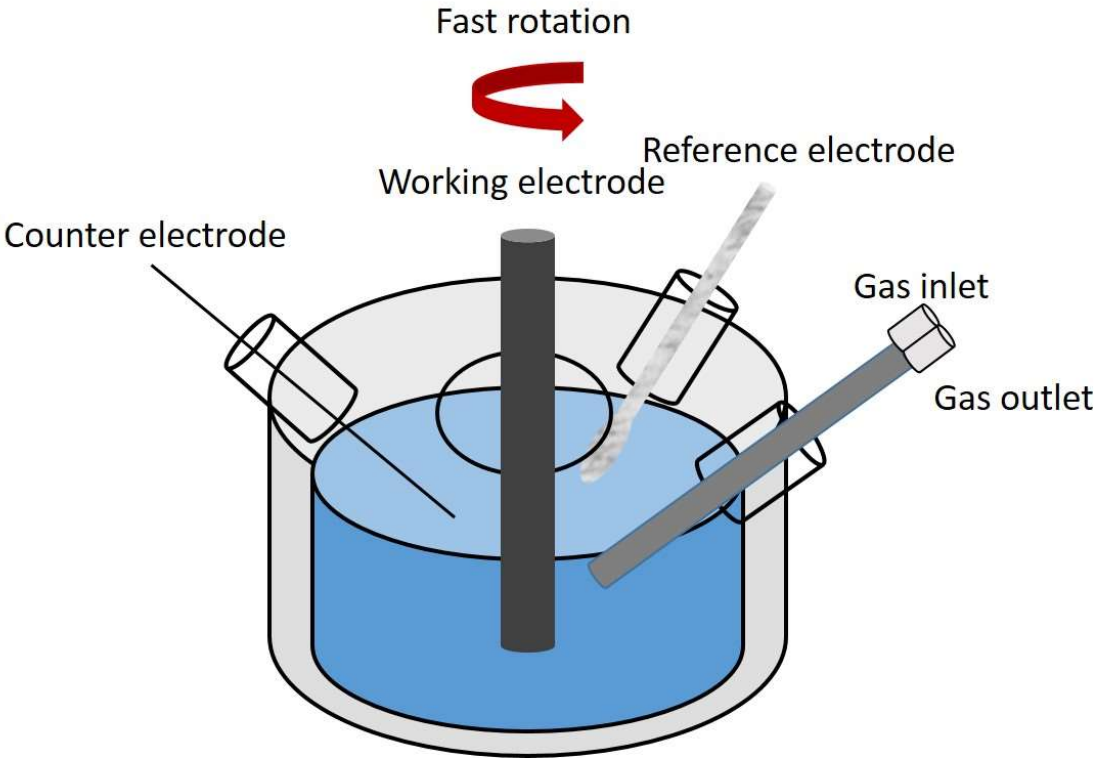


Figure 2-9 A schematic diagram of the apparatus used for electrochemistry experiments.

Experiments are carried out by using a potentiostat (Autolab PGSTAT 128N, EcoChemie, Netherlands) manipulated by GPES software (EcoChemie) or a VersaSTAT 3 (Princeton Applied Research) potentiostat. An electrode rotator from Autolab (Metrohm) was used for controlling the rotation rate.

Gas mass flow controllers (Brooks Instrument) are attached to with the cell to provide accurate and constant concentration of gases in the electrolytes.

Because CODH is extremely sensitive to O_2, all CODH experiments were carried out in a glovebox under an anaerobic atmosphere.

2.2 Fourier transform infrared spectroscopy

2.2.1 Introduction to Infrared spectroscopy

The mid-Infrared (IR) spectral range covers the electromagnetic frequency regime from approx. 4000 - 400 cm^{-1}, which enables excitation of vibrational or vibrational-rotational transitions of molecules involving transitions from / to rotational and / or vibrational levels in the same ground electronic state. IR spectra are frequently used to characterise various functional groups within a molecule, particularly in the so-called "fingerprint" regime (ca. 4000 - 400 cm^{-1}), the vibrations of the related specific bonds show absorption patterns that are highly substance specific. Therefore, IR spectra can be used to determine the chemical nature and molecular structure of a constituent. Since its introduction, IR spectroscopy has increasingly been recognized as an important analytical technique, and has been applied widely in qualitative and quantitative analysis of materials including organic, inorganic, and biological substances.

Commonly, IR spectra are measured in transmission-absorption mode with gas, liquid, or solid phase samples. During the measurement, radiation propagates directly through the sample and is absorbed at frequencies where resonant energy transfer occurs. The wavelength-dependent light reduction is calculated and defined as transmittance (T):

$$T = \frac{I}{I_0} \quad (2\text{-}5)$$

where I_0 is the intensity of incident radiation, and I is the intensity of radiation after passing through the sample.

For quantitative applications of IR spectroscopy, Equation 2-6 is usually rearranged and expressed as absorbance (A):

$$A = \log I_0 - \log I = \log\left(\frac{I_0}{I}\right) = -\log(T) \quad \text{(2-6)}$$

For quantitative measurements, absorbance may also be defined by the Beer-Lambert law:

$$A = \varepsilon c l \quad \text{(2-7)}$$

where ε is the extinction coefficient of the sample, c is the concentration and l is the thickness of sample (optical path length of light through the sample). Therefore, Equation 2-7 shows a linear dependence of absorbance on the thickness of the sample, or more generally, the absorption path length.

The term optical density (O.D.) is normally used as the unit to describe absorbance in practice.

2.2.2 Selection rule

As mentioned previously, the principal of IR spectroscopy is based on vibrations of a molecule. In vibrational spectroscopy, the bonds between atoms in a molecule are modelled as oscillating masses connected by springs. According to

Hooke's law, the frequency of the vibration of the bond is a function of the force constant, k, and reduced mass, μ (Equation 2-8):

$$\nu = \frac{1}{2\pi}\sqrt{\frac{k}{\mu}} \quad \text{(2-8)}$$

Where v is the frequency of vibration and μ is the reduced mass of two atoms m_1 and m_2 as Equation 2-8.

$$\mu = \frac{m_1 m_2}{m_1 + m_2} \quad \text{(2-9)}$$

From the relation between frequency (v) and wavelength (λ) (Equation 2-10):

$$v = \frac{c}{\lambda} \quad \text{(2-10)}$$

The energy difference between two quantised states of the molecule that gives rises to emission or absorption can be written as Equation 2-11:

$$\Delta E = hv = hc\tilde{\nu} \quad \text{(2-11)}$$

Where h is Planck's constant and wavenumber ($\tilde{\nu}$) is 1/v reflects a specific vibrational mode of a molecule. The number of vibrational modes of a molecule containing N atoms can be determined as 3N–5 modes for a linear molecule and 3N–6 modes for a non-linear molecule. For example, the H_2O molecule contains three atoms with a non-linear structure and therefore has 3 vibrational modes, while CO_2 consists of 3 atoms with a linear structure and so has 4 vibrational modes (Figure 2-10). The vibrational mode is infrared-active only if the net

electric dipole moment of a molecule is changed. Therefore, the number of IR active modes depends on the symmetry of the molecule. For example, the symmetric stretching mode of CO_2 is IR inactive, because the electric dipole moment of the molecule does not change during vibration (Figure 2-10).

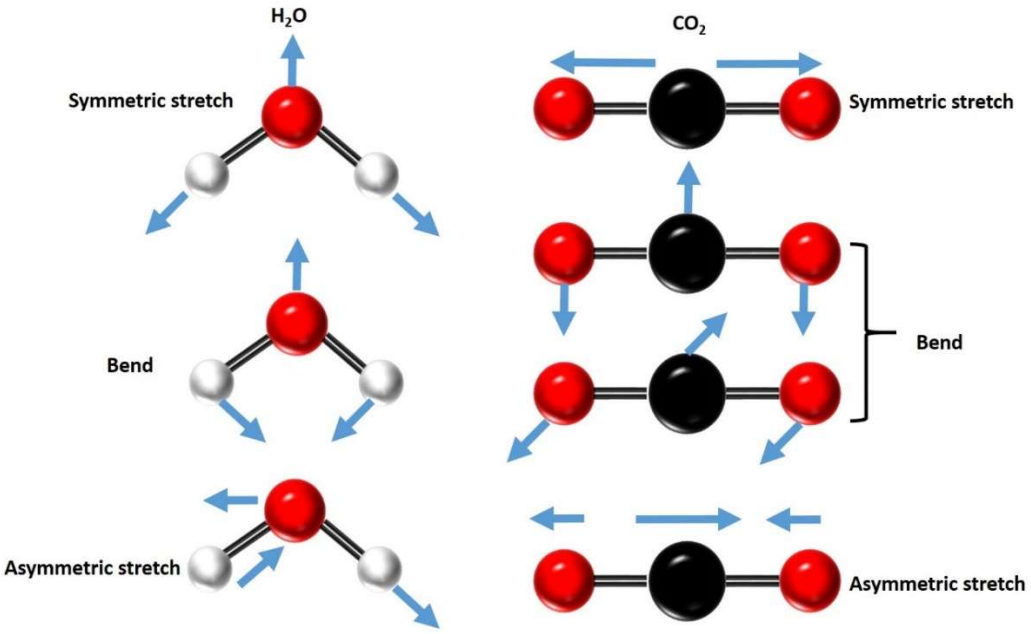


Figure 2-10 Vibrational modes of molecules of H_2O and CO_2.

2.2.3 Surface selection rule

When examining IR spectra for species adsorbed on a surface, the surface selection rule is applied to identify the peaks observed in vibrational spectra. When a molecule is adsorbed on an adsorbent, the molecule induces opposite image charges in the adsorbent. The IR signal is active only when the electric dipole moment of the adsorbate (μ) and the electric dipole moment of the image charges (μ') do not cancel each other as shown in Figure 2-11.[85]

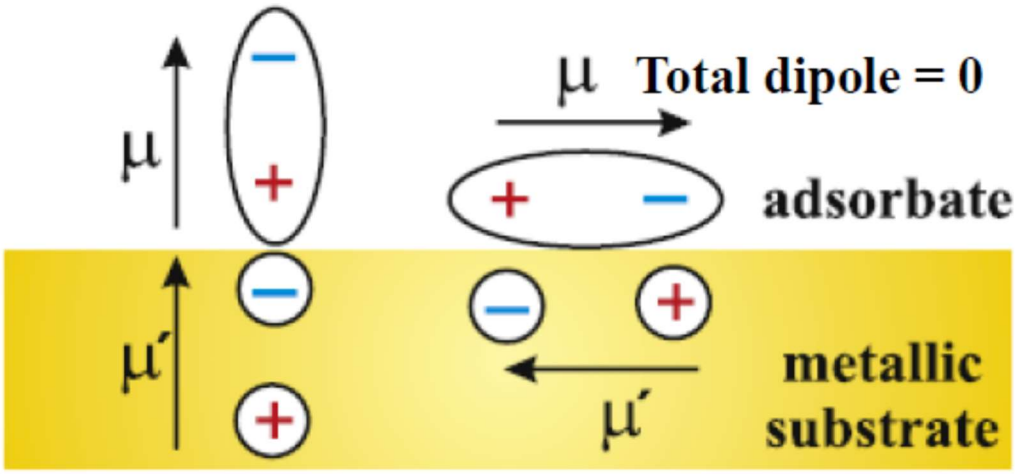


Figure 2-11 The image dipole moment within the adsorbent compensates the effect of the adsorbate's dipole moment for the parallel orientation but enhances the effect of dipole moment for a perpendicular orientation. Adapted from reference 84.

In contrast, when the dipole moments of the molecule is parallel to the image charges of the surface, they cancel out each other (Figure 2-10). Therefore, only molecular vibrational peaks giving rise to a dynamic dipole moment perpendicular to the surface will be observed in the vibrational spectrum.[85]

Figure 2-12 shows an example of applying the surface selection rule to some of the molecules relevant to this Thesis, on a surface. Formate in solution exhibits two characteristic IR bands ascribed to symmetric and asymmetric O-C-O stretching modes, which each yield a dynamic dipole moment. If formate is adsorbed through two oxygen atoms as shown in Figure 2-12, the asymmetric O-C-O mode cannot be detected in IR spectrum since the sum of the dipole moment is cancelled by the image dipole moment.

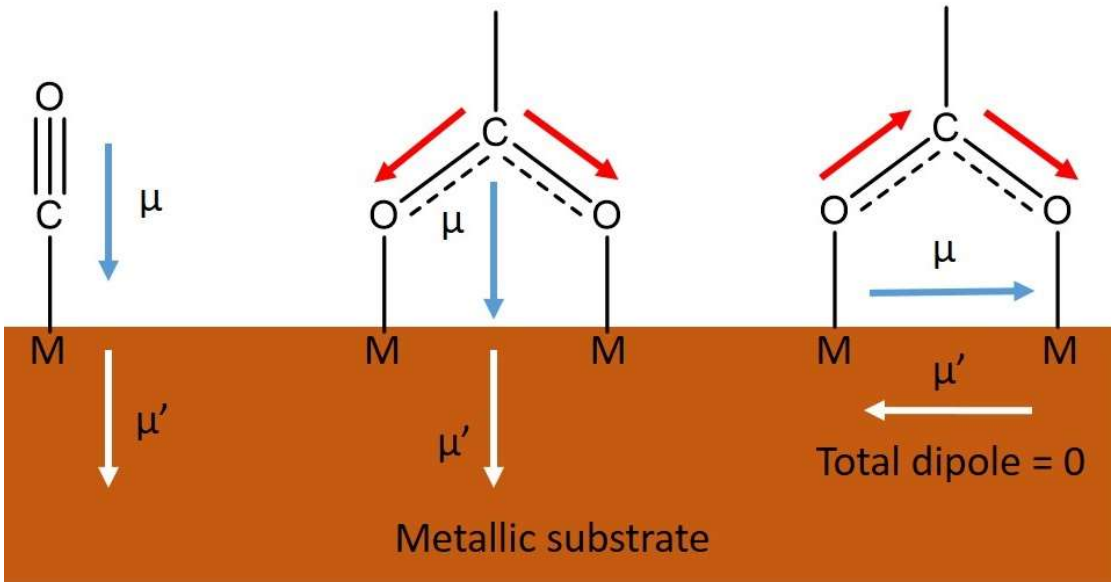


Figure 2-12 The schematic representation surface selection rule on the metal substrate for CO and formate.

The symmetric stretching O-C-O mode can be detected because the dipole moment is not paralleled by the image dipole moment from the adsorbent. For the same reason, the C-O stretching mode of adsorbed CO is therefore also can be detected.

2.2.4 Fourier transform infrared spectroscopy

Fourier transform infrared (FTIR) spectroscopy is a measurement technique for collecting infrared spectra. Instead of recording the amount of energy absorbed when the frequency of the infra-red light is varied (monochromator), the IR light is guided through an interferometer (Figure 2-13). The interferometer consists of an IR source, beam splitter, two mirrors, a laser and a detector. IR radiation from the source is transmitted to the beam splitter, which splits the beam into

two. One of the split beams is reflected at a 90° angle onto a flat fixed mirror, while the other beam is transmitted to a flat mirror which moves back and forth at a constant speed (Figure 2-13).

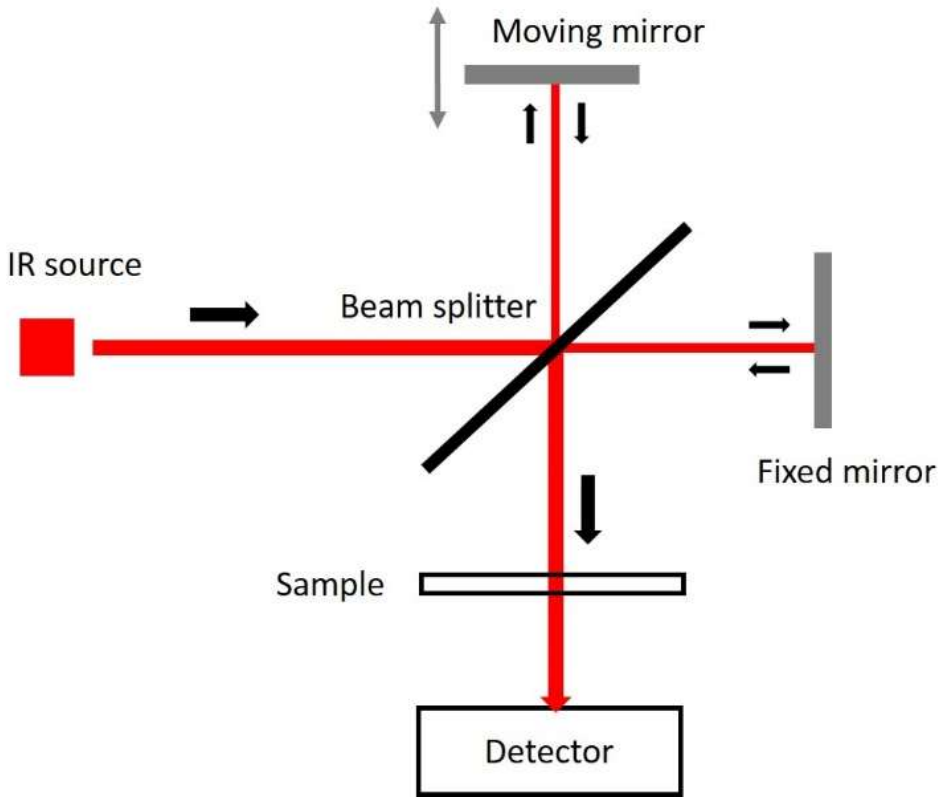


Figure 2-13 A schematic view of the setup of an interferometer.

The two beams are ultimately reflected from their respective mirrors and are recombined as they re-join at the beam splitter. After passing the sample the measured signal is the interferogram. Performing a mathematical Fourier transform on this signal results in a spectrum identical to that from dispersive infrared spectroscopy. FTIR spectrometers are cheaper than dispersive spectrometers because building of interferometers is easier than the fabrication of a monochromator. In addition, measurement of a single spectrum is faster for

the FTIR technique because the information at all frequencies is collected simultaneously. This allows multiple spectra to be collected and averaged together resulting in an improvement in sensitivity.

2.3 Attenuated total reflectance IR spectroscopy and the spectroelectrochemical cell design

2.3.1 Attenuated total reflectance IR spectroscopy

When radiation propagating in a medium of high optical density of refractive index n_1 reaches the interface of a second medium of lower optical density, refractive index n_2 the angle at which the radiation is refracted can be described by Snell's law,[86] as Equation 2-11:

$$n_1 \, sin\theta_1 \; = \; n_2 \, sin\theta_2 \qquad (2\text{-}11)$$

Here θ_1 and θ_2 are the angle of incidence and refraction, respectively, with respect to the normal of the interface. In accordance with Figure 2-14, if $n_1 > n_2$ (n_1 is more optically dense), the angle of refraction θ_2 is larger than the angle of incidence θ_1 as shown in Figure 2-14. As n_1 and n_2 are fixed variables, Snell's law suggests that it is possible that θ_2 can become large enough and becomes equal to 90^0; travelling along the interface between the two media. Instead of this, or transmission through the interface, a phenomenon called total internal

reflection occurs. In total internal reflection, at the angle θ_c or greater, the incident radiation reflects off the interface back into the denser medium.

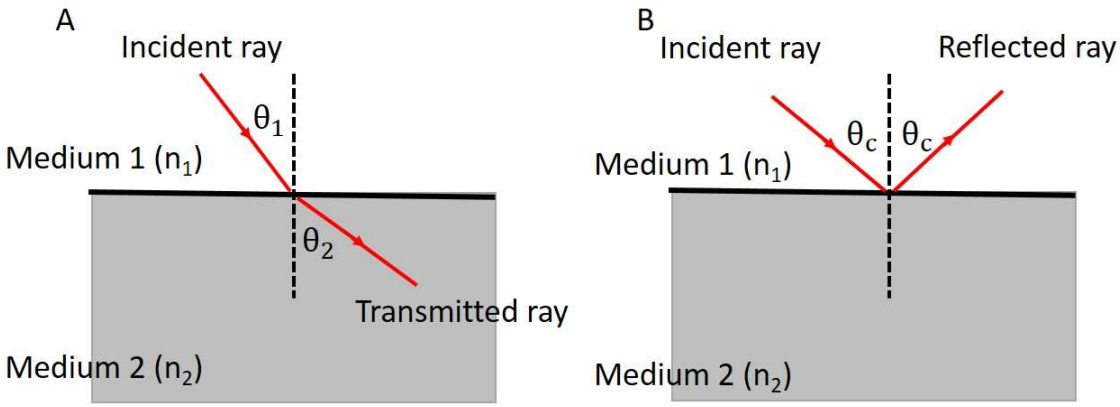


Figure 2-14 A: Diagram of Snell's law when an incident ray travels from one medium to another medium. B: When θ_2 becomes larger than 90^0 and total internal reflection occurs.

The angle at which this happens is called the critical angle, θ_c, and is defined using Equation 2-12, and the result: $\sin 90^0 = 1$,

$$\theta_c = \sin^{-1} {}^{n_2}/_{n_1} \quad \text{(2-12)}$$

An optic allowing internal reflection is known as an internal reflection element, (IRE). A Si IRE is used in this work because it has a high refractive index ($n_1 = 3.41$) and is good for collecting spectra over almost the whole mid-IR range; 4000 to 400 cm^{-1}.

In ATR, the interaction of the infrared radiation with the sample on top of the IRE occurs through the phenomenon of the evanescent wave. The evanescent

wave stems from the fact that the incident radiation consists of photons, each having electromagnetic fields perpendicular to its direction of propagation. This field extends past the interface and into the less optically dense medium, $\boldsymbol{n_2}$, perpendicular to the plane of the IRE.

As expected, the strength of this field, E, decays exponentially with distance into the medium, n_2, following Equation 2-13

$$E = E_0 e^{-\lambda z} \quad \text{.....(2-13)}$$

Here, E_0 is the field strength at the surface, z the distance, and λ a constant. This field extending into n_2 is called the evanescent wave.

The distance to which the electric field strength, E, decays to 1/e of its intensity in n_2 is called the penetration depth, d_p. It is the approximate maximum distance in which there is effective interaction of the evanescent wave with the medium, n_2; which is the sample of interest on the IRE. As well as depending on n_1, n_2, and angle of incidence θ_1, it also is a function of the wavelength of the incident radiation, as shown in Equation 2-14.

$$d_p = \frac{\lambda}{2\pi n_1 \sqrt{sin^2\theta - (\frac{n_2}{n_1})^2}} \quad \text{.....(2-14)}$$

As can be seen from Equation 2-14, the penetration depth depends on the wavelength of the radiation, the ratio of the two refractive indexes and the angle of incidence. These are all factors that go into choosing a suitable IRE for the

experiment. For an experiment investigating a bulk sample the penetration depth needed is large, so a smaller angle of incidence is desired. In this work, as the study is centred on studying a thin layer of Pd-based nanoparticles, the penetration depth need not be too large. In this case a higher angle of incidence (39°) and a high refractive index material is used.

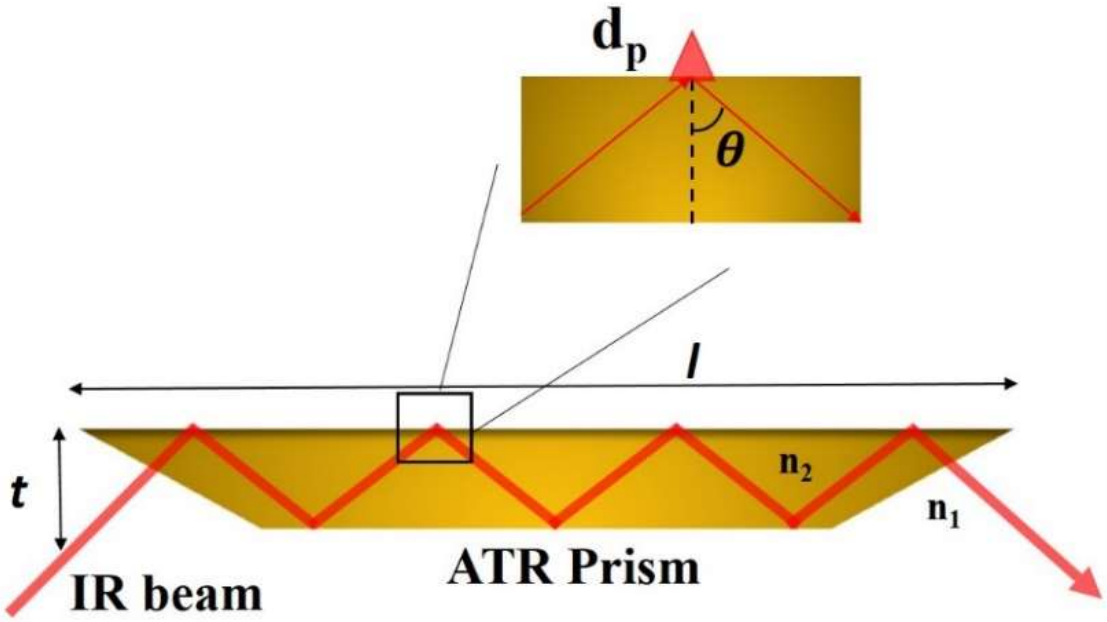


Figure 2-15 A schematic representation of the evanescent wave penetrating through a certain thickness of the sample dispersed on the IRE.

2.3.2 Cell design for studying supported nanocatalysts

As introduced in Section 1.3, the ATR configuration is widely used for spectroelectrochemical studies. However, studying supported nanoparticles by ATR-SEIRAS is limited by many factors such as the inefficient surface enhancement effect due to the size of the support and lack of spectral

information in bulk solution and possible competing electrochemical reactions at gold underlayer electrode. Therefore, a multiple-bounce ATR method is used to study supported nanocatalysts. Figure 2-16 shows a schematics illustration of the configuration used in SEC experiments.

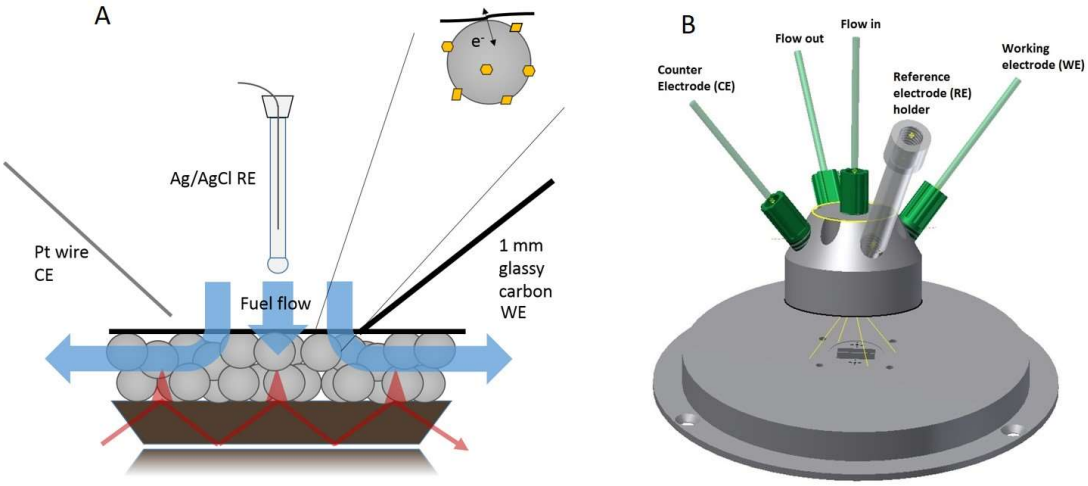


Figure 2-16 A: A schematic representation of the flow ATR SEC cell. A supported catalyst film deposited on the IRE for IR measurement. The flow of fuel overcomes the mass transport limit, allowing efficient electrocatalytic reaction as at a RDE electrode B: A 3D representation (made by Autodesk inventor) of the spectroelectrochemical flow cell showing a baseplate, relative positions of the three electrodes, flow inlet and outlet.

A Si IRE (39^0 Si trapezium, Crystal GmbH, 8.39 × 5 × 1 mm^3) is used for multiple-bounce ATR. The number of reflections for horizontal ATR is determined by Equation 2-15; where N is number of reflections, l is the prism length, t is the prism thickness and θ is the incidence angle (Figure 2-14). In this case, the number of reflections is calculated ca. 5.

$$N = \frac{l}{2t.\tan\theta} \quad \text{(2-15)}$$

The prism is then sealed into the polyether ether ketone (PEEK) baseplate with silicone sealant to avoid solution leakage during an *in situ* measurement. A catalyst film is deposited onto the surface of the IRE by drop-casting method for IR measurement as shown in Figure 2-17.

A rectangle of carbon paper (Toray, TGP H-0-30) is put on the catalyst film on the prism to ensure electrical contact between the WE and catalyst. This is also for ensuring the nanoparticles did not get flushed away under the high flow of electrolyte. The spectroelectrochemical (SEC) cell body (designed by the Vincent group as shown in Figure 2-16 B was then screwed into place on the base plate.



Figure 2-17 A photo of a typical catalyst film made by drop-casting method on a Si IRE.

The cell has 5 different openings, three of them are used for holding the WE, RE and CE. The other two are used as an electrolyte inlet and an electrolyte outlet respectively (Figure 2-16B). Each one of the five openings that are sealed with

an o-ring, to ensure that each of the openings is gas tight. The electrolyte inlet is at 90^0 to the plane of the IRE, directly flowing electrolyte onto the carbon paper. This is to ensure a uniform flow over the entire surface. The outlet is at ~60^0 to the plane of the IRE, as well as all the electrodes. During the IR experiments, the SEC cell was connected to a peristaltic pump (Williamson Manufacturing Company Ltd), with allows an electrolyte flows from solution bottle to waste bottle via the SEC cell with the flow rate 12 mL min^{-1} to allow efficient electrolyte / reactant flow. This allows the desired chemicals or gases to be introduced during an experiment readily and also minimises the effect of mass transport limitation during electrocatalytic reactions.

The spectroelectrochemical measurements were collected using an infrared spectrometer (Agilent Technologies, Cary 600 Series FTIR Spectroscopy) which was connected to an Autolab potentiostat (PGSTAT 128N or μAutolab II / FRA2, Metrohm). A mercury cadmium telluride (MCT) detector was used as it offers higher sensitivity than a deuterated triglycine sulfate (DTGS) detector, and boasts a greater signal to noise ratio. It offers better sensitivity for investigating adsorbed species and is good at collecting spectral data over the whole range mid-IR range 4000 – 600 cm^{-1}. A KBr beam splitter was used.

The spectra collected in this work are reported in absorbance units, $A = -log(R/R_0)$, where R is the reflected intensity of the sample and R_o the reflected intensity of the background.

2.4 Experimental

2.4.1 Pd / XC-72 (Premetek) catalyst ink preparation

For both the electrochemical and spectroelectrochemical experiments on Pd / XC-72 (Premetek, USA, 60% Pd / XC-72), a nanoparticle suspension was dispersed into a water and Nafion™ (10 % wt. dispersion in water, Sigma-Aldrich) mixture solution (49:1) at a loading of 5 mg cm^{-2}.

The loading of 5 mg mL^{-1} was selected as a compromise to ensure that the film is thick enough to show an appreciable electrochemical response and avoid being lost through fast rotation of the RDE experiment or fast flow rates in the SEC cell, but thin enough to allow *in situ* spectrospectroscopic measurement under electrochemical control (details in chapter 3).

Before use, the nanoparticle suspension was sonicated in an ultrasonic bath for a minimum of 60 minutes to ensure that the particles were fully dispersed. This ensured that a uniform thickness film layer was created and subsequent films were made as consistently as possible.

2.4.2 Chemicals

The supporting electrolytes for metal nanocatalyts were perchloric acid (98% Laboratory Reagent Grade, Fisher Scientific) and 0.5 M KOH (98% Laboratory Reagent grade, Sigma-Aldrich). Both of the electrolytes made using ultrapure

(Milli Q) water and saturated with pure N_2 or CO (BOC, 99.9 %). Two different purities of formic acid were used in this Thesis. The HPLC grade formic acid (Fluka, puriss. p.a., for HPLC, 50% in water, 49-51%) was used for making ultrapure formic acid sample and "spiked" sample with impurities (detail in chapter 3 and 4). A reagent grades formic acid (Fluka, 98% (T)) was used for the study of reagent grade formic acid oxidation in chapter 4. Methanol (HPLC grade, ≥99.9%, Sigma-Aldrich) was used for the methanol oxidation study. The 50 mM MES (Fisher) buffer was made with Milli Q water, and was used for the study of CO_2 electro-reduction in chapter 6.

2.4.3 Electrodes and IRE cleaning

In electrochemistry experiments, the glassy carbon surface and PGE electrode was cleaned by polishing with 1 μm and 50 nm alumina slurries, and rinsed with Milli Q water before use.

Before the IR experiments, the Si IRE was cleaned by sonicating in concentrated sulphuric acid for 30 mins to remove the trace silicone sealant remaining from the previous experiment. The IRE was then immersed into "Piranha solution" prepared by mixing concentrated sulphuric acid and 30 % hydrogen peroxide (ACS reagent 29 – 32 % wt. %, Sigma-Aldrich) at 3:1 ratio) for 15 minutes to remove all organic impurities and make the IRE surface to be hydrophilic. The IRE was then rinsed with Milli Q water and dried in air before use.

Chapter 3

Abstract

In this chapter, the new type of multi-bounce ATR-IR spectroelectrochemical approach introduced in chapter 2 (section 2.3) is applied to the mechanistic study of formic acid oxidation on two different commercial carbon supported palladium catalysts (Pd / C, Sigma-Aldrich and Pd / XC-72, Premetek). The different cyclic voltammograms and *in situ* spectra recorded in formic acid solution with the SEC cell suggest that the supporting materials play important roles on *in situ* spectroelectrochemical measurement and a very thin sample film thickness is critical for this technique. In the *in situ* spectroelectrochemical experiment of Pd / XC-72, the υ(CO) cannot be observed in the potential range between 0 V to 1.2 V v.s SHE. This indicates no or only very small amount of CO_{ads} is produced during formic acid oxidation and this is consistent with the general proposed mechanism.

Chapter 3

In situ ATR-IR spectroelectrochemical approach for formic acid oxidation on supported nanoparticles

Palladium is considered as an excellent option to replace platinum-based electrocatalysts for formic acid oxidation due to the reported lack of CO_{ads} arising from the dehydration pathway (refer to section 1.1.2). [12,15,20,21] However, the mechanism on Pd-based catalysts is remain unclear. Infrared spectroscopic techniques such as surface enhanced absorption IR spectroscopy (SEIRAS) and infrared reflection absorption spectroscopy (IRAS) have been widely used to study oxidative reactions of small organic chemicals on thin layer bulk metal surfaces for several years (details in section 1.3.2).[19,20] However, it is difficult to study supported nanoparticle catalysts using these techniques because it is hard to distinguish signals from the metal underlayer electrode from signals coming from the nanoparticle catalyst (refer to section 1.3.2). In this chapter, a study of the formic acid oxidation on the commercial carbon supported Pd catalysts by a new ATR-IR spectroelectrochemical approach developed by the Vincent group for studying supported metal nanocatalysts will be introduced and discussed.

3.1 Catalyst sample preparation of for ATR-IR SEC studies

3.1.1 Electrochemical studies of Pd / C (Sigma-Aldrich)

Before the *in situ* IR SEC measurement, the conventional electrochemical measurement was used to offer a reference of the electrochemistry in SEC cell. The rotating disk electrode (RDE) measurement described in section 2.1.4 and 2.1.5 was used for electrochemical characterization of a carbon supported Pd (Pd / C) catalyst (Sigma-Aldrich, 10 wt % loading, matrix activated carbon support). The cyclic voltammetry was performed in N_2 saturated 0.5 M perchloric acid with a 7 mm diameter glassy carbon working electrode, an Ag / AgCl reference electrode and a Pt wire counter electrode. To make the catalyst ink, 5 mg of the Pd / C was dispersed into 200 μL of ethanol (70 % *v.v.*) by 60 minutes sonication. The film was then formed on the surface 7 mm wafer after 4 μL of the catalyst ink was completely dried out. The cyclic voltammetry (CV) between 0 V and 1.2 V vs SHE shows three regions including hydrogen region, double layer and oxygen region, typical for Pd (Figure 3-1).[87,88] In the low potential region of the forward scan, H desorption occurs on the different faces of the Pd surface and giving positive peaks (Figure 3-1 and Equation 3-1). The two peaks in the hydrogen region suggest Pd (111) and Pd (100) surfaces exist in the Pd / C nanoparticles as discussed in the literature.[89–91] When the potential reaches around 850 mV, the Pd surface is oxidised to Pd-O and this gives an anodic peak as reported in the literature.[88] A negative peak around 680 mV during the

backward scan is caused by the Pd-O bond breaking and oxide desorption (Equation 3-2).[88] As the potential becomes more negative, H adsorption takes place (Figure 3-1 and Equation 3-1).[88,89]

$$Pd\text{-}H \leftrightarrows Pd + H^+ + e^- \quad \text{.....(3-1)}$$

$$Pd + H_2O \leftrightarrows Pd\text{-}O + 2H^+ + 2e^- \quad \text{.....(3-2)}$$

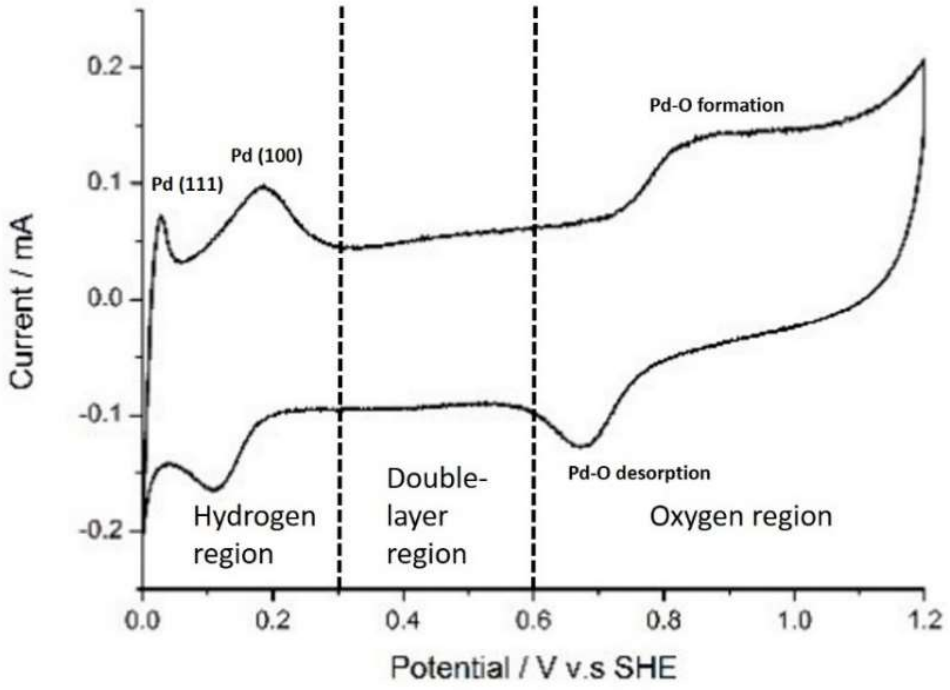


Figure 3-1 Cyclic voltammogram of 100 μg Pd on matrix activated carbon in N_2-saturated 0.1 M $HClO_4$ at a GC electrode rotation rate of 1000 rpm and a scan rate of 10 mV s^{-1}.

Cyclic voltammetry was also applied to investigate formic acid oxidation on the Pd / C catalyst (Sigma-Aldrich) in 0.1 M formic acid (HPLC grade in perchloric acid).

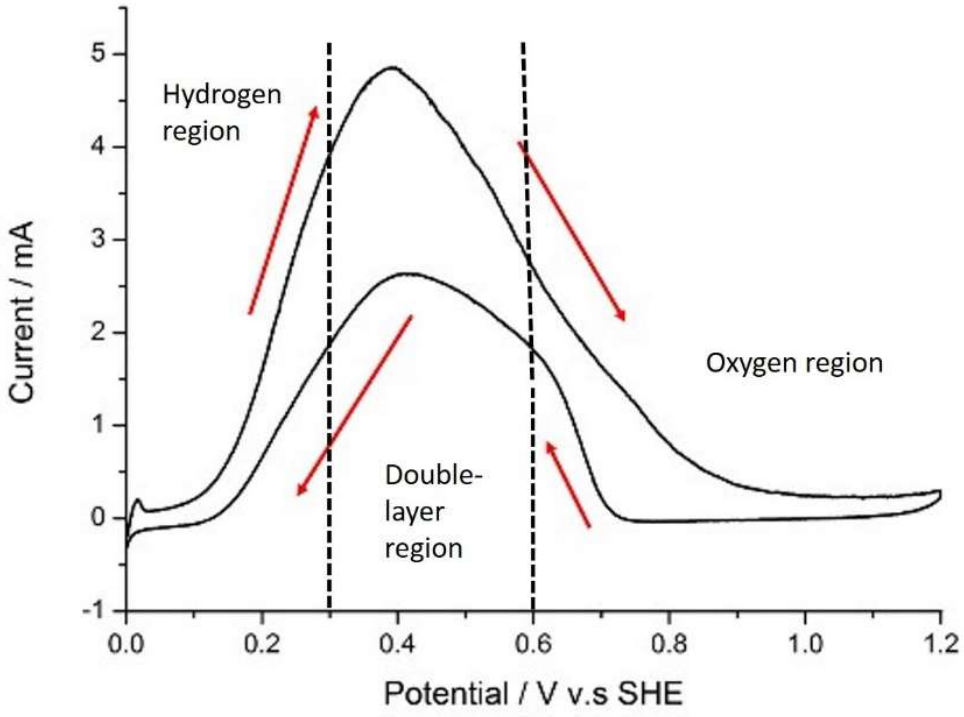


Figure 3-2 A cyclic voltammogram of 10 % Pd on matrix activated carbon in N_2 saturated 0.5 M $HClO_4$ with 0.1 M HCOOH. The measurement was carried out with the electrode rotating at 1000 rpm and at a scan rate of 10 mV s^{-1}

The CV shows an oxidative current increased rapidly on the forward potential sweep from the potential around 0.1 V and reached a maximum current at around 0.4 V. However, at more positive potentials the current drop to zero. This is consistent with some of the studies reported under similar conditions.[92–94] The potential of 0.4 V is well below the potential for Pd oxide formation which suggests that the loss of oxidative activity is not simply caused by oxide blocking the surface sites (Figure 3-2).

Recently, the slow deactivation of Pd during operation in the direct formic acid fuel cell (DFAFC) has also been observed by a number of research groups and the reason for deactivation is still controversial.[25,95,96] The proposed reasons for deactivation of Pd catalysts include surface poisoning adsorbates such as formate, bicarbonate, carbon dioxide and sulphuric anions,[13,97,98] but none of them has strong evidence to support the proposal. To understand more details of the formic acid oxidation mechanism on the Pd / C catalyst, *in situ* spectroelectrochemistry was then used for further studies.

3.1.2 *In situ* IR spectroelectrochemistry of a Pd / C (Sigma-Aldrich)

The similar electrochemical characterisation was done within the spectroelectrochemical (SEC) cell. The drop-casting method described in chapter 2 is used to make a catalyst film on the IRE. A piece of carbon paper is put on the film to make electrical contact across the film of particles with glassy carbon working electrode. A piece of Pt wire and a commercial Ag / AgCl electrode are used as counter electrode and reference electrode respectively (details in section 2.3.2). By connecting with a peristaltic pump, electrolyte and fuel can be flowed into the cell with flow rate at 12 mL min^{-1} to prevent reaching a mass transport limit under catalytic conditions. Figure 3-3A shows electrochemical data collected in the SEC cell for formic acid oxidation with a slow scan rate at 1 mV s^{-1}. The slower scan rate was used for higher potential resolution during

recording spectroscopic data. The similar shapes of cyclic voltammogram at the forward scan compared with the one at an RDE suggests good electrochemical control can be gained from the spectroelectrochemical cell (Figure 3-3A and Figure 3-3B). Surprisingly, the significant lower current at the backward scan suggests that the catalyst was poisoned or being deactivated after high potential had been reached.

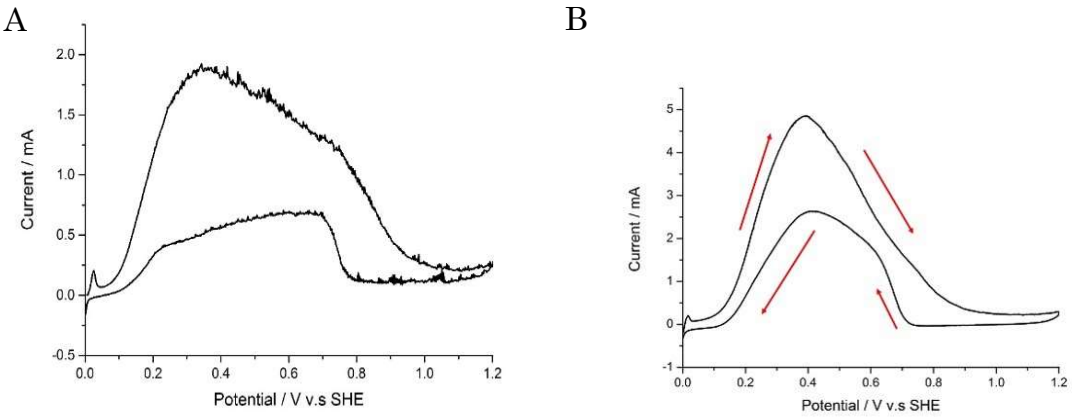


Figure 3-3 A: Cyclic voltammograms for Pd on matrix activated carbon (Sigma-Aldrich) in N_2 saturated 0.5 M $HClO_4$ with 0.1 M HCOOH was collected in SEC cell solution flow rate at 12 mL min^{-1} and at scan rate 1 mV s^{-1}. B: CV recorded at an RDE measurement reproduced from Figure 3-2.

Figure 3-4 shows the *in situ* IR spectra with during cyclic potential scan. All spectra in this chapter are averaged over 100 mV steps. Two IR peaks were found during formic acid oxidation. The one at 2341 cm^{-1} can safely be assigned to solution phase of CO_2 produced as a product of formic acid oxidation. The other IR peak was found around 1957 cm^{-1} when the potential sweep reached

about 1.1 V and this peak then shifted to lower wavenumbers during the negative-going potential scan.

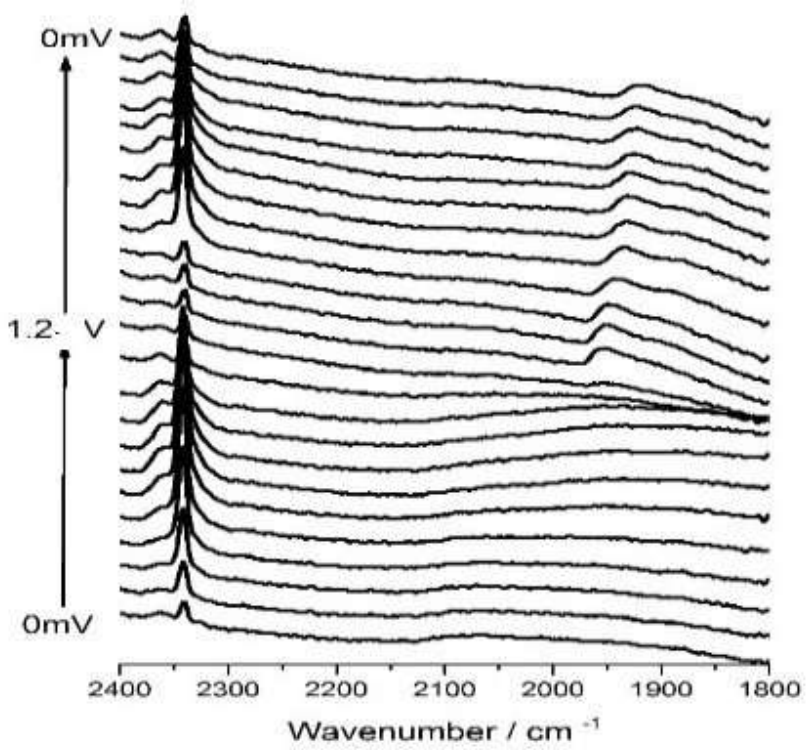


Figure 3-4 *In situ* IR spectra recorded simultaneously with the voltammogram in Figure 3-3A. The peak at 2341 cm^{-1} is assigned to solution phase CO_2 as the product of formic acid oxidation. The peak at lower wavenumber appears at high potential and shifts to lower wavenumber on the backward scan.

The wavenumber shift can be explained as due to the Vibrational Stark Effect (VSE) caused by the change of electric field during a potential scan. [99–101] Bridge-bonded carbon monoxide (CO_B) on a Pd thin layer surface has been reported to give a strong IR signal between 1900 cm^{-1} and 1955 cm^{-1} in SEIRAS studies.[97,102] To confirm whether the 1957 cm^{-1} peak is CO_B on the Pd / C catalyst, the CO-saturated perchloric acid solution was introduced into the flow SEC cell under

open circuit potential (OCP) after the background spectrum was taken in CO-free $HClO_4$. A decrease of the open circuit potential was observed and can be interpreted as arising from CO adsorbing on the surface. A difference spectrum was then taken using a background spectrum recorded in CO-free $HClO_4$ solution. A derivative shape peak at 1956 cm^{-1} was observed. The abnormal shaped IR peak has been reported with reflectance spectroscopic measurement on metal surfaces in the literature[103,104] and also has been observed for CO on Pt in the ATR-IR cell by other group members.[105] It probably arises from a reflective component in the ATR spectra, which might vary with film preparation or surface changes on the metal.

This position of the ν(CO) peak on the CO-exposed catalyst (Figure 3-5A) is similar to the position of the peak in Figure 3-4 (expanded in Figure 3-5B) and this suggests the 1957 cm^{-1} peak comes from CO_B on Pd. The formation of CO on the catalyst at high potentials can also explain the lower current during the backward scan.

The pathway involving formation of CO is generally accepted as not favourable for formic acid oxidation on Pd surfaces.[15,22,23] However some very recent research has found weakly bound CO when very high loading of carbon supported Pd[106] or Pd metal thin layer[107] are under high concentration of formic acid oxidation in low potential region.

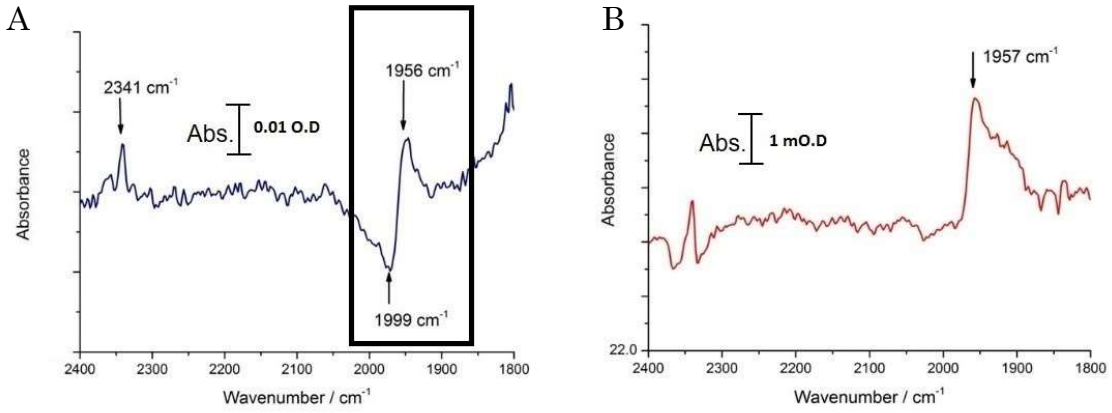


Figure 3-5 A: Pd on matrix activated carbon exposed to CO-saturated electrolyte at open circuit potential B: The average of spectra recorded between 1050 mV and 1150 mV v.s SHE during the potential sweep towards positive potentials in formic acid 0.1 M.

This was detected by different infrared techniques and the CO peak could be oxidatively removed at high potential.[106,108] In the spectra shown in Figure 3-4, CO appears only at very high potential (ca. 1.1 V v.s SHE) which is much higher than the overpotential requirement for CO oxidation on Pd. Therefore, the existence of CO-bound Pd at such a high potential should not be possible. In addition, the catalyst used in this study is relatively much lower loading compared with the one used in the other literature.[106] Therefore, the appearance of a 1957 cm^{-1} peak in the very high potential range is very difficult to explain. One possible reason for this could be that electrochemical control is not effective throughout the whole catalyst film, and would be worst at the lower part of the film on the prism where ATR-IR sampling is most effective, meaning that all the CO cannot be electrochemically removed. This may be causing poor *in situ* electrochemical control during spectroscopic measurements. Therefore, the

thickness of the catalyst film will be ideally around the penetration depth of the ATR evanescent (refer to section 2.3) wave for an *in situ* spectroelectrochemical measurement. Another possibility for the source of the CO might be from the oxidation of the supporting material or a small amount of ethanol from the catalyst suspension absorbed in small pores of the supporting carbon material. In this case, solvents containing alcohol should be avoided for a "cleaner" catalyst ink preparation.

3.1.3 Film thickness analysis for Pd / C (Sigma-Aldrich)

As discussed in the previous section, the thickness of the catalyst film should be similar to the penetration depth of the evanescent wave. The penetration can be calculated by Equation 2-14. In this study the Si IRE (8.39 x 5 x 1 mm^3 with an incidence angle of 39°), has calculated penetration depth (d_p) in aqueous solution of ca. 500 nm. Therefore, a thin and uniform film thickness (ideally around 500 nm) will be important for *in situ* electrochemical and spectroscopic measurements. The film thickness was determined by Scanning Electron Microscopy (SEM) measured by Jonathan Quinson (DPhil student, Oxford) at Begbroke Science Park (Oxford). The SEM sample was made by the same drop-cast method used for ATR measurement but on a Si crystal. The thickness of the film was determined to be about 30 μm from the SEM images (Figure 3-7) which is much thicker than the evanescent penetration depth.

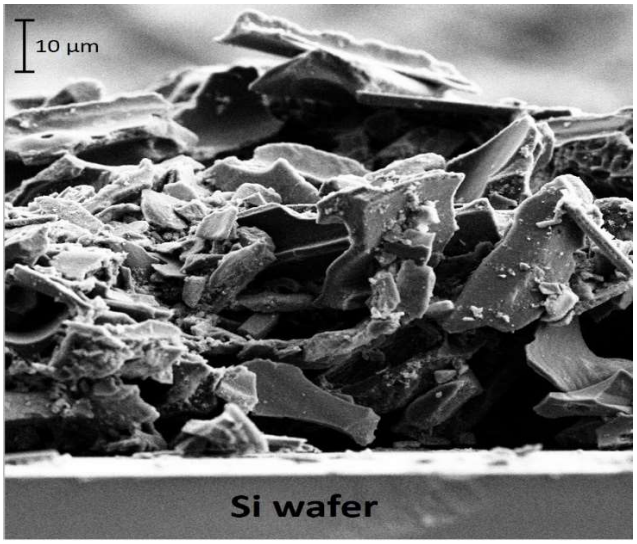


Figure 3-6 Scanning electron microscope image of a 60% Pd / C (Sigma-Aldrich) film collected on a Si surface showing the thickness is around 30 μm.

This could be the reason of improper *in situ* measurement of formic acid oxidation with the ethanol dispersed Pd on matrix activated carbon catalyst. Also the carbon support has a large particle size which tend to cause non-uniform film thickness, and the large particles could completely block the IR penetration.

3.2 Spectroelectrochemical study on Pd / XC-72 (Premetek)

3.2.1 Thinner and cleaner catalyst film

As discussed in the previous section, making a thinner and "cleaner" catalyst film in essential to ensure good *in situ* spectroelectrochemical control over a catalyst film.

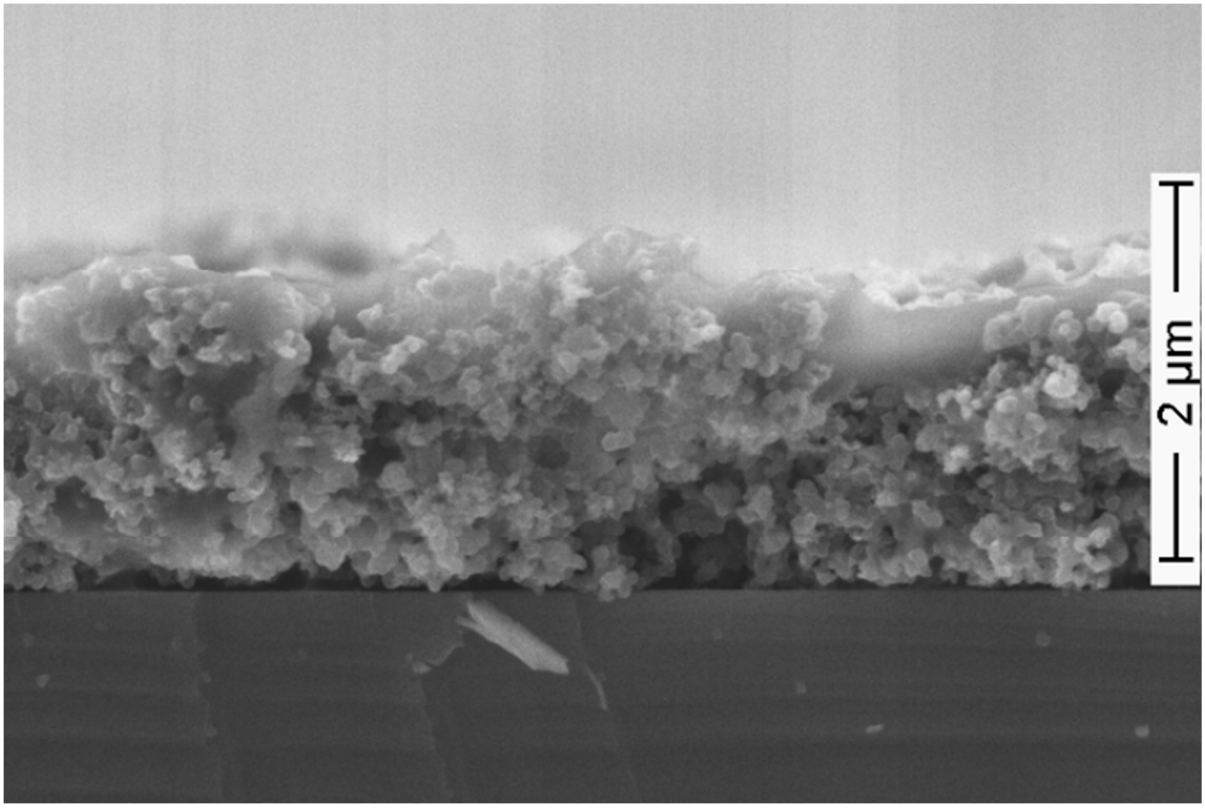


Figure 3-7 The scanning electron microscope image of a Pd / XC-72 catalyst (Premetek) film collected on a Si surface showing the thickness is < 2 μm.

For making this, different alcohol-free solvents (water, aqueous Nafion™ and toluene) and different "concentrations" of the suspension (5 mg mL^{-1}, 10 mg mL^{-1} and 15 mg mL^{-1}) were tested to make comparisons with the 25 mg mL^{-1} ethanol dispersion. However, because of the very large size of carbon support material (Figure 3-6), none of them gave a significant difference in the film thickness measured from SEM images.

Hence, an alternative carbon supported catalyst Pd / XC-72 (Premetek, USA, 60% loading on Vulcan carbon XC-72) with much smaller support particle was then purchased and used in the future experiments in the rest of the chapters

in this Thesis. For the best result of catalyst film formation, the particles were dispersed into a water and Nafion™ (10 % wt. dispersion in Water) mixture solution (49:1) at a loading of 5 mg cm^{-2}. The film was then made by allowing the 10 μL ink to dry out in a 50 °C heating oven. The film thickness was then measured using SEM (Figure 3-7). The thickness of the film is < 2 μm, much closer to the penetration depth of the ATR evanescent wave.

3.2.2 Electrochemical characterization of Pd / XC-72 (Premetek)

Cyclic voltammetry between 0 V and 1.2 V in 0.5 M perchloric was performed with this Pd / XC-72 catalyst on a RDE.

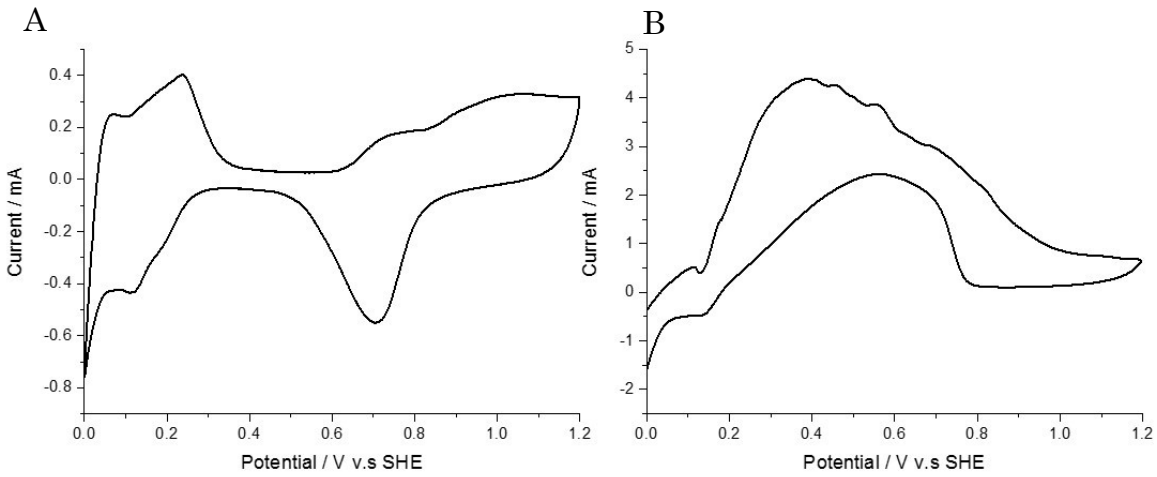


Figure 3-8 A: Cyclic voltammogram of Pd / XC-72 in 0.5 M $HClO_4$ with 10 mVs^{-1} scan rate B: Cyclic voltammogram of Pd / XC-72 in 0.5 M $HClO_4$ and 0.1 M formic acid with 10 mVs^{-1} scan rate. Both of the two experiments were conducted at a RDE with the Pd / XC-72 deposited on the surface with the electrode rotating at 1000 rpm.

The clear hydrogen adsorption / desorption and oxide formation / desorption features are found with this catalyst (Figure 3-8A) as discussed previously. The different shapes of peaks in the hydrogen region (compared to Figure 3-1) are due to the different distribution of Pd surfaces.[90,91,102] The narrower double layer region is consistent with the lower carbon percentage, because larger capacitance usually comes from the supporting material. In formic acid oxidation (Figure 3-8B), the cyclic voltammetry showed similar features to the Pd / C (Sigma-Aldrich) catalyst.

3.2.3 *In situ* IR spectroelectrochemical study for Pd / XC-72 (Premetek)

The cyclic voltammogram of formic acid oxidation on this small catalyst Pd / XC-72 (Premetek) in SEC cell (Figure 3-9) has similar feature with RDE measurement. Interestingly, unlike the cyclic voltammetry with the Pd / C (Sigma-Aldrich), the catalytic current on the negative-going scan did not decrease much compared with the forward scan suggesting the electrochemical control was more similar to the RDE condition (Figure 3-9). The 2341 cm^{-1} solution phase CO_2 peak was again found in spectra recorded during a potential sweep (Figure 3-10). Because the cell is connected with a high flow rate peristaltic pump, all the solution species are expected to be able to be removed at the potential where are not produced.

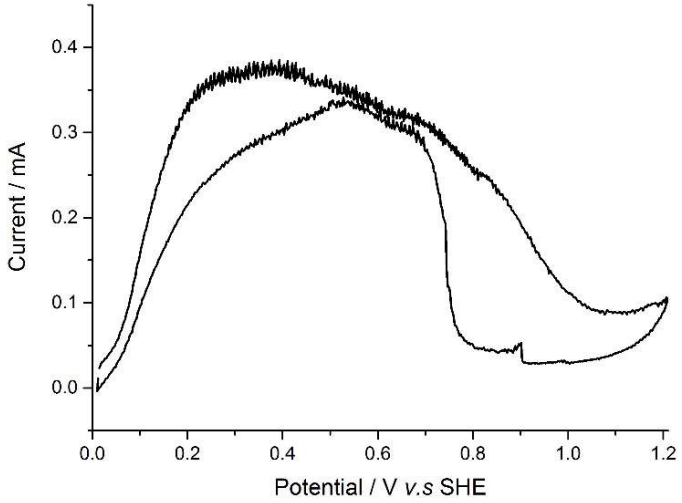


Figure 3-9 Cyclic voltammograms for Pd / XC-72 in N_2 saturated 0.5 M $HClO_4$ with 0.1 M HCOOH was collected in SEC cell with flow rate: 12 mL min^{-1} and at scan rate 1 mV s^{-1}.

Therefore, the intensity of $\nu(CO_2)$ is should be greatest in region where catalysis occur and disappear when catalysis is switched off since CO_2 is the final product of formic acid oxidation. Consistent with this, the intensity of the solution CO_2 peak at 2343 cm^{-1} tracks catalytic current in cyclic voltammetry, which also implies good *in situ* spectroscopic and electrochemical control as well as good mass transport (Figure 3-11). No IR signal at 1957 cm^{-1} was found during the whole CV (Figure 3-10), indicating no CO was produced by the formic acid oxidation in the experiment. This can also explain why the catalytic current did not decrease on the negative-going.

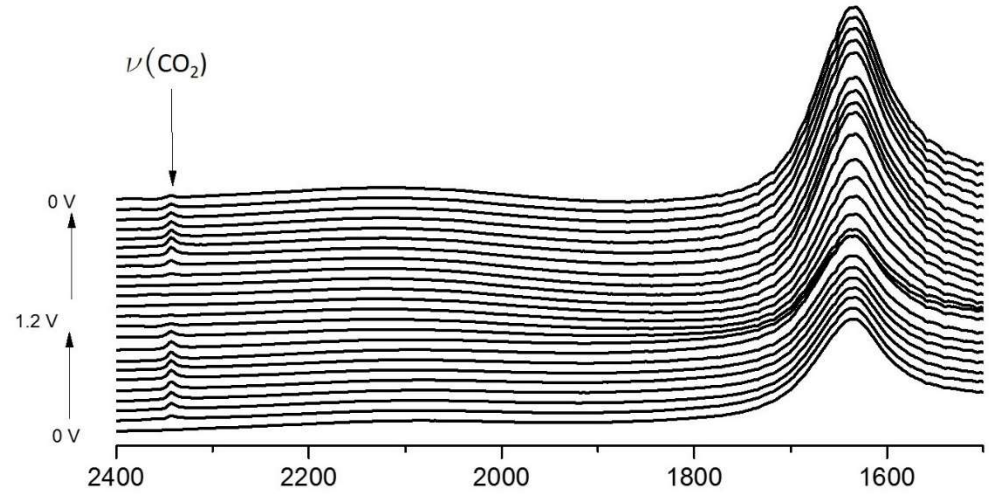


Figure 3-10 *In situ* IR spectra recorded simultaneously with the voltammogram in Figure 3-9. The peak at 2341 cm^{-1} is assigned to solution phase CO_2 as the product of formic acid oxidation.

As discussed in the previous section, the formation of CO at high potential discovered is not easy to be explained. The absence of CO IR signal and higher current at backward scan suggest no carbon monoxide was formed during formic acid oxidation on the Pd / XC-72 catalyst.

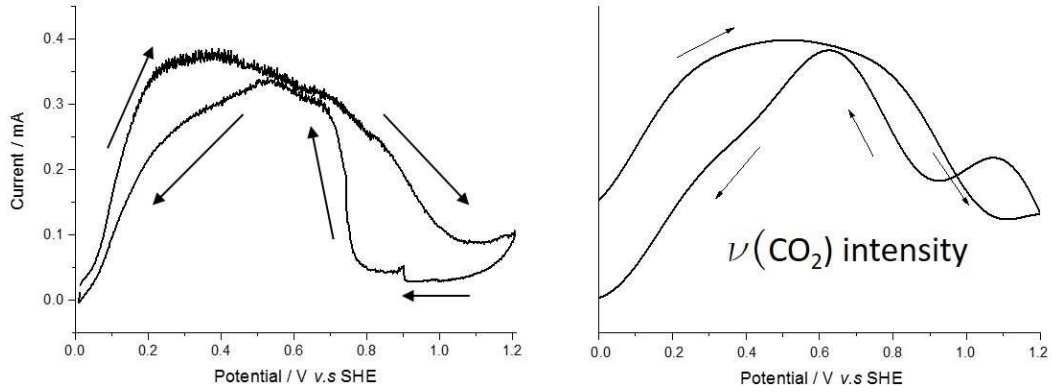


Figure 3-11 A: The cyclic voltammogram recorded during formic acid oxidation on Pd / XC-72 B: The IR peak intensity of $\nu(CO_2)$ from the spectra over potential scan

3.3 Discussion

The reason of different behaviours on formic acid oxidation catalysed by the two different carbon supported palladium catalysts can be very complicated. Although, the formation of CO during high concentration of formic acid oxidation has been reported by a few authors, the observation of the CO peak in formic acid solution at high potential is still not usual for matrix activated carbon supported Pd. The formation of CO may be caused by the side chemical reactions such as supporting carbon oxidation or remained alcohol containing solvent oxidation. The fact that the CO peak is not electrochemically removable suggest inefficient electrochemical control due to the thick film. The thickness was not able to be lower due to the large size of the supporting carbon material. The Vulcan carbon support has much smaller particle size and can be dispersed into alcohol-free solvent, giving a catalyst film thickness < 2 μm. The electrochemistry of Pd / XC-72 catalyst and the catalytic tracking CO_2 peak in the IR suggest a reliable *in situ* measurement. Therefore, Pd / XC-72 catalyst was then used for *in situ* spectroelectrochemical studies in the rest of this Thesis. The absence of a CO peak in IR suggests the CO pathway is not favourable on the Pd / XC-72 and that CO formation from formic acid is not causing the deactivation of formic acid oxidation.

Chapter 4

Abstract

This chapter presents results that demonstrate deactivation of the Pd catalyst due to common impurities in industrial and reagent grade formic acids such as acetic acid, methanol and ethanol. IR peaks which have previously been assigned as multi-bonded CO (CO_M) and hollow-bonded CO (CO_H) were observed during oxidation of reagent grade formic acid, and CO_{ads} was also observed during potential scan in HPLC grade formic acid 'spiked' with 100 ppm ethanol and methanol. This supports the suggestion from literature that deactivation of Pd-based catalysts during formic acid oxidation arises from the impurities in the fuel. Therefore, the use of Pd-based catalysts in DFAFC is not realistic since it is impractical to use high purity of formic acid for industrial use.

Chapter 4

In situ spectroelectrochemical study of the deactivation of Pd / XC-72 particles during formic acid oxidation

4.1 Introduction: Formic acid oxidation and CO poisoning on Pd

4.1.1 Pathway review of formic acid oxidation on metals

The prospective application of direct formic acid fuel cells and the importance of mechanistic study of formic acid oxidation were described in the previous chapters. The dual pathway mechanism is generally recognised as the reaction path of formic acid oxidation on precious metal surfaces. Proposed by Capon and Parsons in the 1970s, this mechanism has two different routes by which the molecule can be oxidised to CO_2. In the original proposal, the direct pathway, involves dehydrogenation of HCOOH, forming CO_2, protons and electrons without a detectable intermediate.[19] It favours high turnover efficiencies at low overpotentials through a direct conversion of formic acid to the carbon dioxide product (Equation 4-1).[19] The indirect dehydration pathway forms a strongly

adsorbed carbon monoxide (CO_{ads}) reaction intermediate on the metal sites (M) via an initial non-Faradaic step (Equation 4-3). To complete further oxidation of CO_{ads}, an additional activated hydroxyl species (OH_{ads}) is required. OH_{ads} is typically formed on a separate catalytic surface site (Equation 4-4; M(1) and M(2) present two different metal sites) at higher overpotentials. The two adsorbed intermediates diffuse across the catalyst surface to combine and complete the conversion sequence (Equation 4-5).[12] The limited availability of OH_{ads} results in the accumulation of CO_{ads} that blocks the catalyst surface, limiting the turnover efficiency.

Direct Pathway:

$HCOOH \rightarrow CO_2 + 2H^+ + 2e^-$ (Dehydrogenation)……(4-1)

Reactive intermediate:

$HCOOH \rightarrow HCOO_{ads} + H^+ \rightarrow CO_2 + 2H^+ + 2e^-$……..……..(4-2)

Indirect Pathway:

$HCOOH + M\ (1) \rightarrow M(1)\text{-}CO_{ads} + H_2O$……..……(4-3)

$H_2O + M\ (2) \rightarrow M(2)\text{-}OH_{ads} + H^+ + e^-$……..……..(4-4)

$M(1)\text{-}CO_{ads} + M(2)\text{-}OH_{ads} \rightarrow M(1) + M(2) + CO_2 + H^+ + e^-$……..…….(4-5)

Pt and Pd are two of the most popular metal catalysts for catalysing the electro-oxidation of formic acid. In the past decade, fundamental studies of formic acid oxidation (FAO) on Pt and Pd mainly focused on three aspects:

(i) clarifying the chemical nature of the active intermediate in the direct pathway,

(ii) how to diminish CO adsorption on Pt electrodes

(iii) understanding whether and how CO_{ads} form on Pd catalysts.

It has been long assumed that the formation of adsorbed carboxylic acid ($COOH_{ads}$) is the main rate determining intermediate of formic acid electro-oxidation on the metal surfaces.[17] However, the assumption lacks spectral evidence.[17] Until reported by Osawa et al, the detection of adsorbed formate ($HCOO_{ads}$) by ATR- SEIRAS on a chemically deposited Pt thin layer electrode suggested that a third reaction pathway through a bridge-bonded formate ($HCOO_{ads}$) intermediate is possible (Equation 4-2).[109,110] The indirect pathway of formic acid oxidation on Pt electrode has also been studied by several IR spectroscopic approaches.[18] The adsorbed carbon monoxide (CO_{ads}) is identified as the major poisoning species formed through the dehydration pathway on Pt.[18] It has been widely recognized that the dehydration pathway of formic acid oxidation is not much favoured on the Pd-based electrode surfaces and the absence of CO poisoning leads to a much higher initial catalytic activity on Pd at lower potentials as compared to that on Pt surfaces.[19] No IR signal for CO_{ads}

was found on thin layer Pd on Pt[15] or Au[111] electrodes during the oxidation of formic acid in both IRAS and ATR-SEIRAS studies respectively. Furthermore, in the previous chapter of this Thesis, the spectroelectrochemical study (chapter 3.2.2) on Pd / XC-72 (Premetek) also showed no CO_{ads} formation during formic acid electro-oxidation which is consistent with the previously reported studies and supports the hypothesis that the formic acid oxidation mainly goes through the direct pathway on Pd.

4.1.2 Deactivation of Pd catalysts in formic acid oxidation

In 2005, Masel's group [9] used Pd black particles as an alternative anode catalyst for DFAFCs and demonstrated significant performance enhancements compared with Pt particles. However, several research groups have then reported that the activity of Pd catalysts decreases over time under fuel cell operation.[25,112] The proposed reasons for deactivation of Pd catalysts include surface poisoning by adsorbates such as CO-like species,[95] weakly bound formate,[89] sulphuric anions in the electrolyte[97] and other anions.[15] Recently, adsorbed formate ($HCOO_{ads}$) was found during formic acid oxidation by an *in situ* Infrared spectroelectrochemical technique in formic acid oxidation.[97] However, similar to the case on Pt surfaces, adsorbed formate is detected only when formic acid oxidation is suppressed in the high potential range suggesting adsorbed formate as a short-lived reactive intermediate involved in the direct pathway of formic acid oxidation on Pd.[16,97] Weak bands of CO_{ads} have also been

found under formic acid oxidation. Nevertheless, the very low coverage of CO suggests the formation of CO was very slow and would not be main the reason causing deactivation of Pd surfaces. More recent IR studies have detected CO infrared bands on a Pd thin layer in concentrated formic acid (5 molar)[108] and at a particularly high loading of supported Pd catalyst,[106] but both of these studies were in very different conditions to the real life DFAFC.

The impurities of formic acid have been proposed as the main cause of deactivation of Pd catalysts by Blair and co-workers.[113] The most common method for industrial production of formic acid is through hydrolysis of methyl formate. In this method, methanol is first being carbonylated with carbon monoxide to form methyl formate. ($HCOOCH_3$). Methyl formate is then hydrolyzed to produce formic acid and methanol, which are then separated by solvent extraction. Therefore, methyl formate and methanol are two of the most common organic impurities in formic acid. Acetic acid is also common in commercial formic acid due to the difficulty of separation.

The reagent grade of formic acid was examined by ^{1}H NMR. The 50 - 3000 ppm of methyl formate and acetic acid were detected in different brands of reagents by Blair's group.[113] The performance of a Pd black anode DFAFC was tested with the HPLC grade formic acid containing different concentrations of acetic acid, methanol or methyl formate. The cell potential of the DFAFC containing 500 ppm of methanol and methyl formate decreased by about 50 % within 2

hours of operation, suggesting methanol and methyl formate cause deactivation of the Pd catalyst. In contrast, the cell potential of a DFAFC in which the formic acid contained acetic acid remained stable for at least 3 hours.[113] The similar deactivation by organic impurities in formic acid on carbon supported nano-Pd catalysts was also reported by another research group, supporting Blair's conclusion.[98] The partial oxidation of methanol or other impurities offer the possibility of producing CO_{ads} to poison the Pd surface (Equation 4-6 and 4-7).

$$CH_3OH \rightarrow CO_{ads} + 4H^+ + 4e^- \quad (4\text{-}6)$$

$$HCOOCH_3 + H_2O \rightarrow CO_{ads} + 6H^+ + 6e^- \quad (4\text{-}7)$$

Here in this chapter, the new ATR-IR spectroelectrochemical approach is used to investigate electro-oxidation of formic acid of varying purity on a Pd / XC-72 catalyst (Premetek).

4.2 *In situ* IR spectroelectrochemical study of Pd / XC-72 catalyst in formic acid containing different impurities

In the previous chapter, the CO_{ads} was not detected during HPLC grade formic acid oxidation on Pd / XC-72 catalyst, consistent with the CO pathway not being favourable. As suggested in the previous studies, the organic impurities in reagent grade of formic are highly likely to cause deactivation of the Pd catalyst in the DFAFC.[98,113] In this chapter, the ATR-IR spectroelectrochemical approach introduced in chapter 2 and chapter 3 was used to investigate electro-

oxidation of formic acid of varying purity on a Pd / XC-72 catalyst. The spectroelectrochemical (SEC) cell setup has been described in previous chapters. All the solutions were saturated by N_2 for 20 minutes to remove dissolved O_2 gas before use to avoid the CV to be affected by the signal from O_2 reduction at low potential region.[114] The SEC cell is connected with a peristaltic pump (Williamson Manufacturing Company Ltd) with 12 mL min^{-1} flow rate to provide efficient mass transport during formic acid oxidation as described in chapter 2 and chapter 3.

4.2.1 CO poison surface

Before studying formic acid oxidation with the *in situ* IR spectroelectrochemical technique, it is very important to make sure the *in situ* measurement is sensitive enough for detection of surface adsorbates in the catalyst ink. Carbon monoxide is one of the most common small molecule probes for studying metal surfaces, especially for vibrational spectroscopic studies. Depending on the nature of the metal surface, CO can physisorb or it can chemisorb on non-dissociatively or dissociatively. As discussed in section 1.3.1, the CO molecule has several orbitals that can take part in bonding the surface. In addition, it can occupy different adsorption sites on the surface. The vibrational modes of CO_{ads} on different surface sites can offer very useful information on surface properties, such as structure changes and electrochemically active surface area (ECSA). Therefore, CO was used as a probe to the Pd catalyst for this study not only because of its

strong vibrational signals when adsorbed on metal surface sites but also it is one of the possible intermediates / poisons of formic acid oxidation.

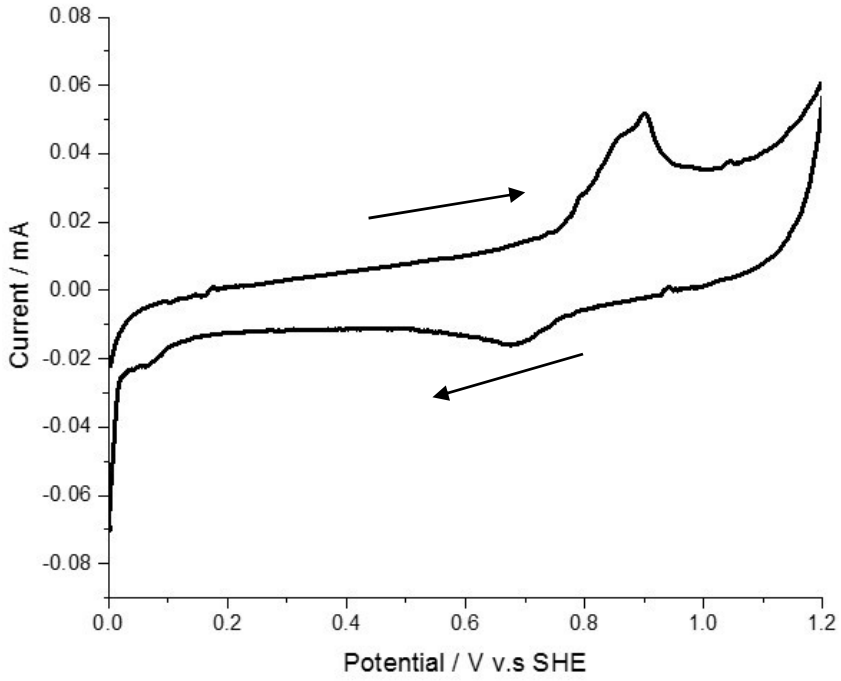


Figure 4-1 Cyclic voltammogram of CO-bound Pd / XC-72 in the SEC cell in N_2 saturated 0.5 M $HClO_4$. The CO-saturated acid was first flowed in and out of the SEC cell for 300 seconds and then the catalyst film was washed by pumping N_2-flushed acid in and out of the SEC cell for another 300 seconds before and during the measurement. Scan rate: 1 mVs^{-1}. Flow rate: 12 mL min^{-1}.

To understand CO adsorption and activation on the Pd surface, CO-saturated perchloric acid was first introduced into the SEC cell by a peristaltic pump for 5 minutes at open circuit potential to make a CO poisoned surface. The CO-saturated $HClO_4$ was then removed by pumping in CO-free $HClO_4$ for another 5 minutes. Figure 4-1 shows the cyclic voltammogram of CO-poisoned Pd / XC-72

in SEC cell with continuous flow of CO-free $HClO_4$. The potential was then scanned between 0 V and 1.2 V. The peaks in the hydrogen region (refer to Figure 3-1) were absent, indicating that CO poisoned the Pd surface and blocked its reaction with protons in the $HClO_4$ solution. The double layer region (around 0.3 V to 0.6 V) remained flat and narrow which was consistent with the CV in CO-free $HClO_4$. Once the potential was scanned into the oxygen region (> 0.6 V), there was an obvious increase of the anodic current which reached a maximum at around 0.9 V. The potential range of high current coincides with the potential window where Pd-O and Pd-OH formation takes place. Therefore, the surface adsorbed CO is very liked to be oxidised with assistance from Pd-OH as described in Equation 4-4 and Equation 4-8.

$$Pd\text{-}CO_{ads} + Pd\text{-}OH \rightarrow CO_{2\,(aq)} + 2Pd + H^+ + e^- \quad (4\text{-}8)$$

Figure 4-2 shows the *in situ* ATR-IR spectra of the Pd on XC-72 recorded simultaneously with the voltammogram in Figure 4-1 (Positive-going scan). The adsorption of CO on Pd surfaces can be also be found in *in situ* IR spectra recorded during the potential scan. Two major ν(CO) peaks were found in the low potential range. The derivative shape peak between 1900 cm^{-1} to 1950 cm^{-1} can be assigned to bridge-bonded CO (CO_B) since it has been reported in the literature (Table 4-1) and also been found in the previous experiment (Figure 3-5) in this Thesis. The other band around 2040 cm^{-1} has been reported in the

literature and has been assigned as linear-bound (CO_L) on Pd. Both of the peaks can be oxidatively removed at high potential region (Figure 4-2).

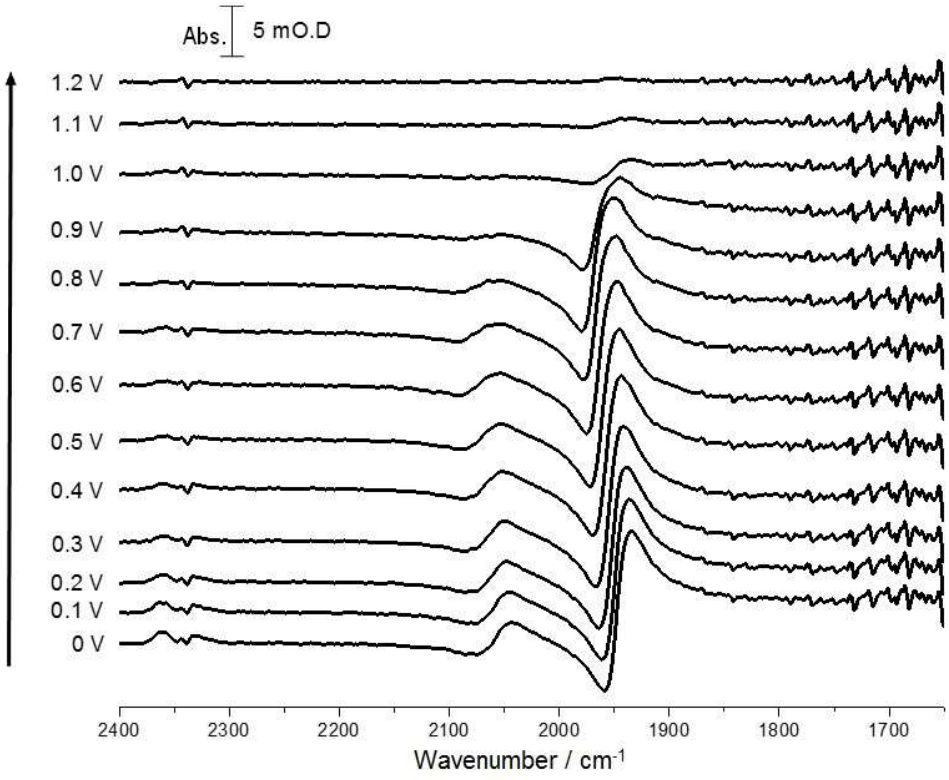


Figure 4-2 *In situ* ATR-IR spectra of the Pd / XC-72 recorded simultaneously with the voltammogram in Figure 4-1 (Positive-going scan). Two ν(CO) IR peaks, CO_L and CO_B were found after the CO-saturated solution flowed into SEC cell. The spectrum that was recorded at 0 V before CO-saturated solution introduced into SEC cell is used as the background.

From the spectra, the CO_L was completely removed at around 0.9 V and the CO_B required higher potential to be completely removed. This suggests CO_B has stronger adsorption than CO_L. The IR signal of CO_L is at higher wavenumber

than CO_B can be explain as that CO can access electron density from multiple metal sites as discussed in section 1.3.

Table 4-1 Wavenumbers of CO-bound Pd reported by literatures.[97]

Wavenumber / cm^{-1}	Species
2341 cm^{-1}	Solution phase $CO_{2\ (aq)}$
2050-2058 cm^{-1}	Linear-bonded CO (CO_L) [97]
1900-1955 cm^{-1}	Bridge-bonded CO (CO_B) [97]
1815-1870 cm^{-1}	Hollow-bonded (CO_H) [97]
1700-1740 cm^{-1}	Mulitiple-bonded (CO_M) [97]

The observation of CO_{ads} IR peaks shows that spectroscopic information on surface species on the Pd / XC-72 catalyst can be detected by the ATR-IR technique used in this study. The potential for oxidative removal of CO_{ads} observed by IR spectra is consistent with the oxidative peak in the voltammogram indicating good potential control in the *in situ* measurements in the SEC setup.

4.2.2 Oxidation of reagent grade formic acid

The ATR-IR spectroelectrochemical experiment was also carried out to examine formic acid oxidation in reagent grade formic acid. For this study, reagent grade formic acid (Fluka, 98% (T)) was used to make 0.5 M formic acid solution for spectroelectrochemical study. Cyclic voltammetry between 0 V to 1.2 V was performed in the SEC cell in 0.5 M reagent grade formic acid. Figure 4-3 shows the cyclic voltammogram from reagent grade formic acid. The CV shows similar features to the CV in HPLC grade formic acid.

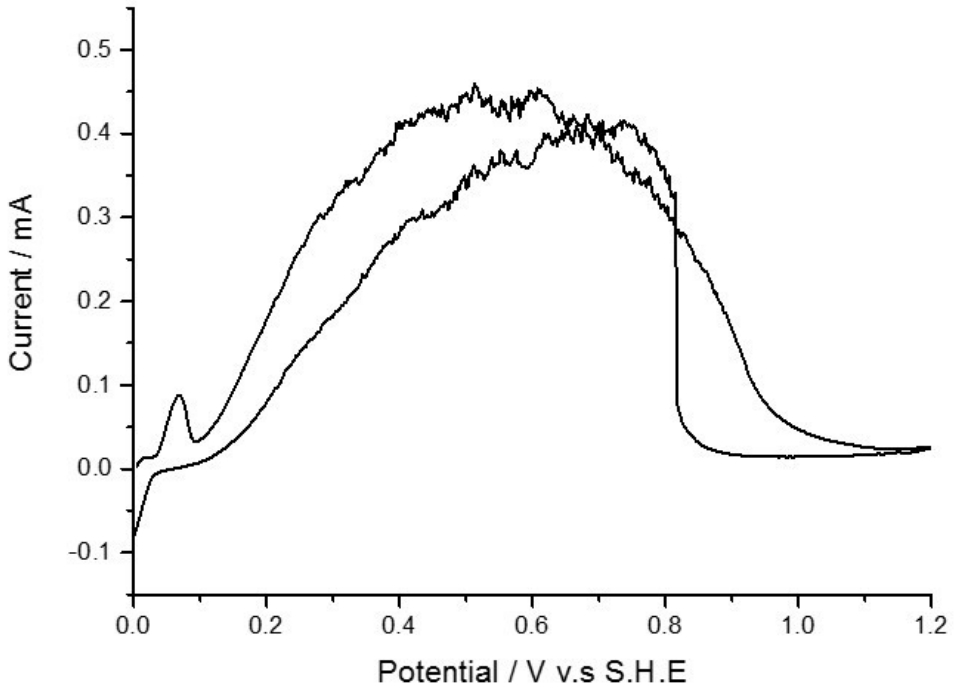


Figure 4-3 Cyclic voltammogram recorded in 0.1 M reagent grade of formic acid oxidation in the SEC cell. Scan rate: 1 mV sec^{-1}. Solution flow rate: 12 mL min^{-1}.

Figure 4-4B shows the spectra recorded during the potential scan. The solution phase of CO_2 IR peak at 2341 cm^{-1} can be found at the potentials where catalytic currents indicate formation of CO_2 as the product of formic acid.

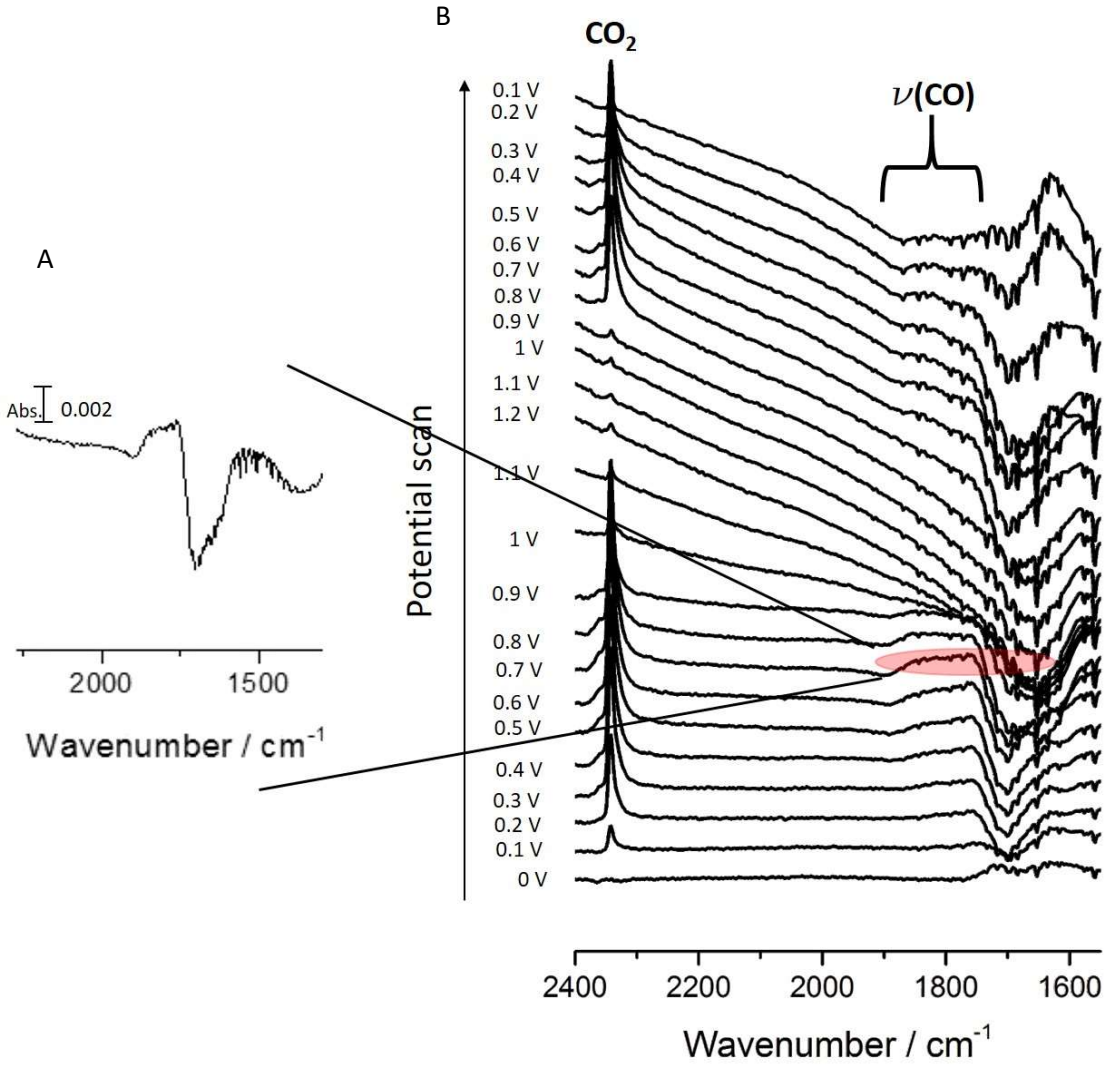


Figure 4-4 A: Zoomed-in spectrum of the spectrum at 0.7 V B: *In situ* ATR-IR spectra of the Pd / XC-72 recorded simultaneously with the voltammogram Figure 4-3.

At the potentials more negative than 400 mV, no IR signal was detected from solution CO_2 indicating the formic acid oxidation was not dominated by the indirect pathway in low potential range.

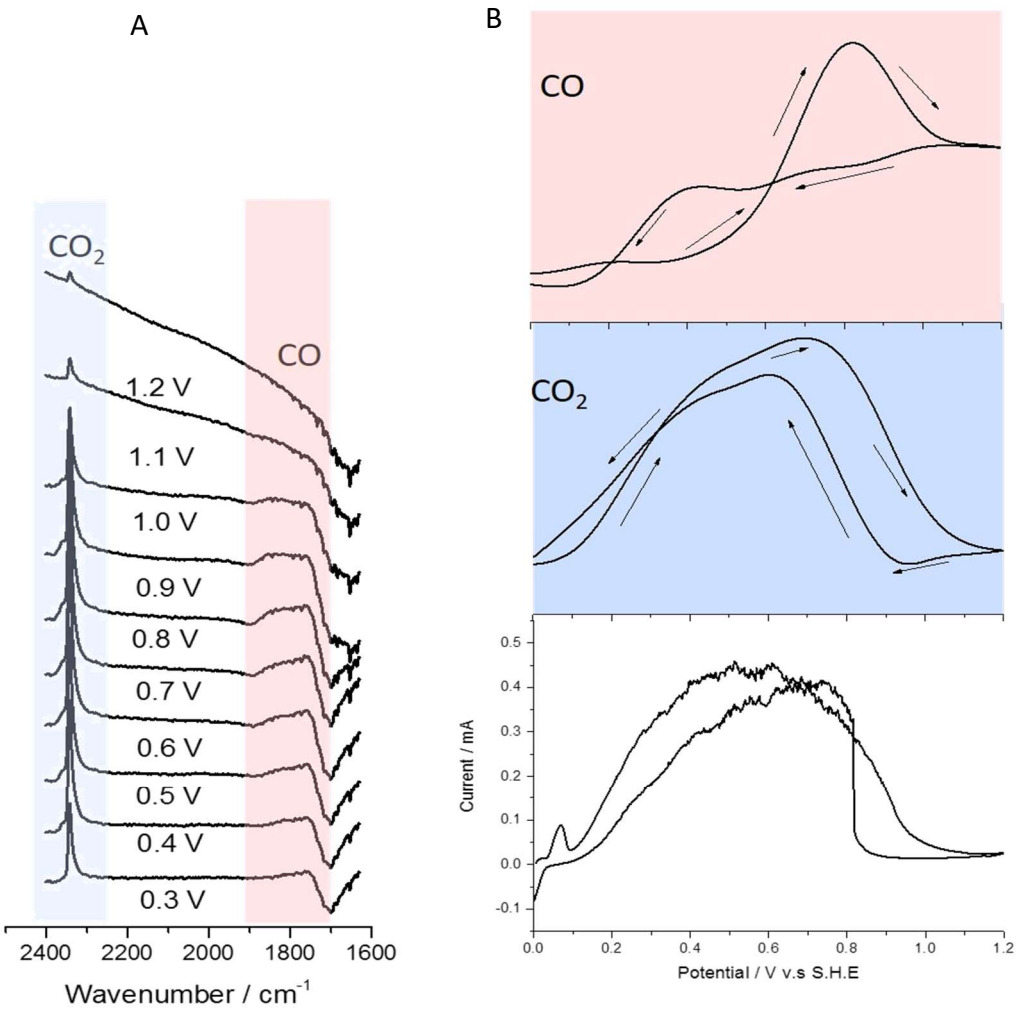


Figure 4-5 A) Time-resolved ATR-IR spectra of the Pd / XC-72 recorded simultaneously with the voltammogram in Figure 4-3A (Positive scan) B) Top: the integrated area between 1700-1870 cm^{-1} as CO peak intensity. Middle: peak intensity of CO_2. Bottom: The cyclic voltammogram record under reagent grade of formic acid oxidation in the SEC cell.

A very broad band between 1740 cm^{-1} and 1850 cm^{-1} can be found when the potential is swept more positive (Figure 4-4B). This broad shape is quite common when multiple similar peaks are overlapped. The intensity of this band continues to increase during the positive-going potential scan until it reached maximum intensity at around 800 mV. The peak then decreased in intensity at the potentials higher than 800 mV and it was completely be removed by around 1.0 to 1.1 V (Figure 4-4). It has been reported the hollow-bound CO (CO_H) on Pd surfaces has its ν(CO) an IR peak between 1815 cm^{-1} and 1870 cm^{-1} and the multi-bound CO (CO_M) has the its ν(CO) IR between 1700 cm^{-1} and 1740 cm^{-1} (Table 4-1 and Figure 1-7).[97] The broad band found here then can be considered as the overlap of CO_H and CO_M. The bands started to decrease when the potential was raised above to 0.8 V (Figure 4-4), is consistent with the potential of CO oxidation from the CO-poisoned surface (Section 4.2.1). This also offers another evidence to support assignment of these two peaks as the CO_{ads} signals.

Figure 4-5A presents a more detailed view of the CO_2 band and ν(CO) bands from spectra recorded during the positive-going sweep of the CV. Figure 4-5B presents the change of peak intensity of CO_2 peak and ν(CO) bands. Because of the broad unusual peak shape of the CO bands, the peak intensity cannot be easily to be determined by peak high like the CO_2 peak. In this work, the integrated area of these two bands (1700 cm^{-1} and 1870 cm^{-1}) were used as the peak intensity. Besides, the intensity of CO reaches its highest intensity when

the catalytic current and solution CO intensity start to decrease, indicating that CO is a poison (Figure 4-5B).

4.2.3 HPLC grade formic acid spiked by small organic chemicals

The small organic chemicals with methyl groups have been detected by nuclear magnetic resonance (NMR) spectroscopy in industrial and reagent grades of formic acid and have been believed to be one of the main reasons of degradation of fuel cell performance. HPLC grade of methanol, ethanol and acetic acid were used to spike HPLC formic acid for making model impure formic acid samples. Concentrated HPLC grade ethanol, methanol and acetic acid were added into 0.5 M formic acid (Fluka, puriss. p.a., for HPLC, 50% in water, 49-51%) to final concentration of 100 ppm. Spectroelectrochemistry experiments were done using HPLC grade formic acid spiked by 100 ppm CH_3COOH, CH_3OH and C_2H_5OH individually.

Figure 4-6 shows the *in situ* spectra during potential scan from 0 V and 1.2 V in formic acid containing 100 ppm methanol. Similar to the experiment in reagent grade formic acid, a broad band between 1740 cm^{-1} and 1850 cm^{-1} can be found when the potential was stepped more positive than 0.4 V (Figure 4-6). This broad band decreased when the potential was raised above 0.8 V (Figure 4-6).

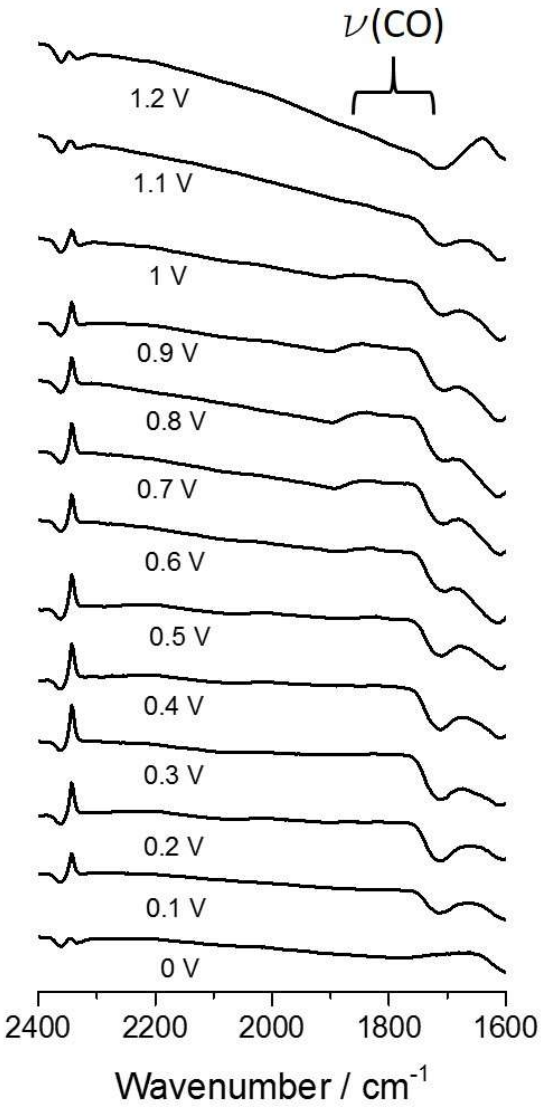


Figure 4-6 *In situ* ATR-IR spectra of the Pd / XC-72 recorded during potential scan from 0 V to 1.2 V in 0.5 M $HClO_4$ with 0.1 M HPLC grade formic acid and 100 ppm methanol. Scan rate: 1 mVs^{-1}. Flow rate: 12 mL min^{-1}.

Both of the peak position and the potential oxidative removal are consistent with the result found in the similar experiment using reagent grade formic acid. Therefore, this broad band can be assigned as the overlap of CO_M and CO_H in

section 4.2.2. The result indicates that the formation of CO_{ads} by only ppm level of methanol in pure formic acid is possible.

Figure 4-7 summarises the difference spectra of Pd / XC-72 in formic acid with different impurities at 0.8 V. All spectra were calculated using the spectrum recorded at 0 V under the same condition as background.

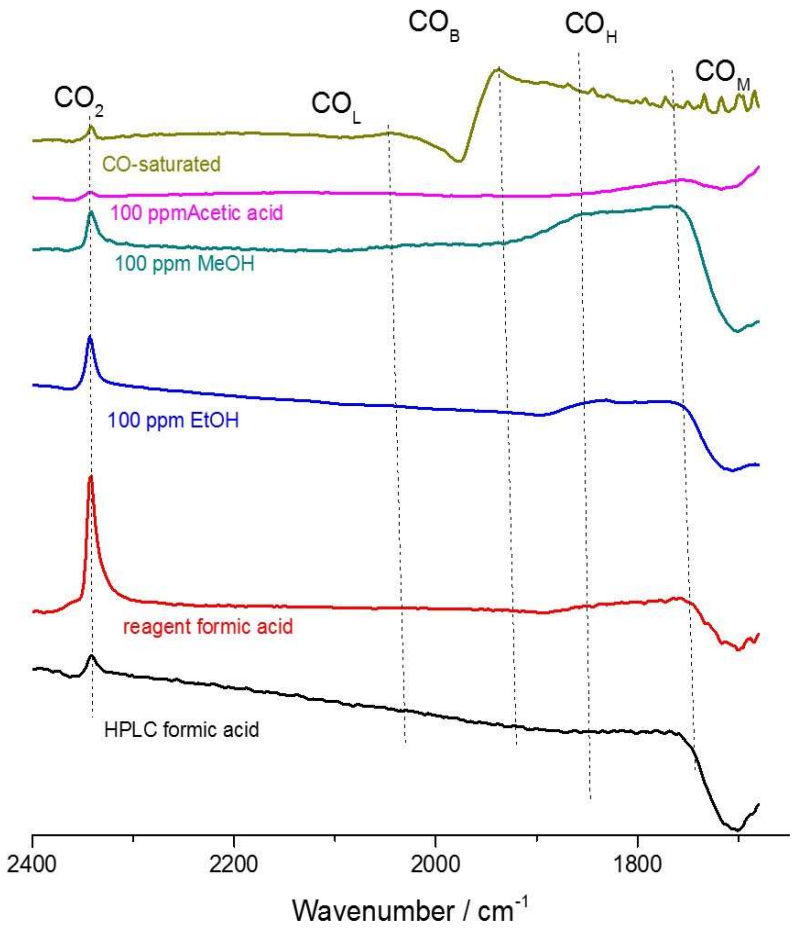


Figure 4-7 Difference spectra of Pd / XC-72 in formic acid with different impurities at 0.8 V. All the different spectra uses the spectrum recorded at 0 V under the same condition as background.

In the formic acid containing methanol and ethanol the ν(CO) can be found in the spectra, this implies both of the methanol and ethanol can cause formation of CO_{ads} in the certain potential range.

Interestingly, in the formic acid containing acetic acid, the 1740 cm^{-1} and 1850 cm^{-1} band was absent or less intense. This suggest low concentration of acetic acid in formic acid might not able to form CO_{ads} or only undetectable amount of CO_{ads} are formed. This is consistent with the observation of no obvious decrease of fuel cell performance when the DFAFC was operated with formic containing acetic acid, as reported by Blair et al.[113] Besides, the CO_M and CO_H were not found in the experiment using CO-saturated perchloric acid solution (Figure 4-7). The can be explained as the binding of organic chemical such as acetic acid, methanol and ethanol on Pd catalyst requires multiple surface sites and cause different binding modes after the chemical bond breaking.

4.3 Discussion

Impurities in formic acid have been suggested as a cause of deactivation of Pd catalysts by formation of CO_{ads} from trace acetic acid, methanol and ethanol in industrial and reagent grade formic acid. In this chapter, the use of a new Attenuated Total Reflectance (ATR)-IR spectroelectrochemical approach has been demonstrated to investigate electro-oxidation of different purities of formic acid on Pd / XC-72. Poisoning by CO was not observed during electrocatalytic

oxidation of HPLC grade formic acid. However, IR peaks which have previously been assigned as multi-bonded CO (CO_M) and hollow-bonded CO (CO_H) were observed during oxidation of reagent grade formic acid, and CO_{ads} was also observed for HPLC grade formic acid 'spiked' with 100 ppm ethanol, methanol. This supports the suggestion that deactivation of Pd catalyst during formic acid oxidation arises from alcohol impurities in the fuel. Interestingly, in the formic acid containing acetic acid, the CO_{ads} was not found. This suggests that low concentration of acetic acid in formic acid does not form CO_{ads}, or that the level of CO_{ads} is too low to be detected. This is consistent with the observation of no obvious decrease of fuel cell performance when the DFAFC was operated with formic containing acetic acid, as reported by Blair et al.[113]

In conclusion, the use of Pd-based catalysts in DFAFC is not realistic since it is impractical to use high purity of formic acid for industrial use.

Chapter 5

Abstract

In chapter 5, the IR SEC method is applied to study methanol oxidation on the Pd / XC-72 in both acidic and alkaline conditions. In acidic conditions, the Pd / XC-72 shows very low catalytic current for methanol oxidation in the potential range between 0 V to 1.2 V. A strong ν(CO) can be also found in this potential range. This suggests that the electrooxidation of methanol in acidic conditions is dominated by the CO pathway.

The observation of ν(CO), ν_{as}(OCO) and ν_{as}(OCO) bands of dissolved formate during the potential scan in alkaline conditions suggests CO and formate both act as the intermediates in electrooxidation of methanol at the Pd / XC-72 catalyst in alkaline media. The ν_s(OCO) band of $HCOO_{ads}$ around 1320 cm^{-1} was detected for the first time for Pd by an *in situ* IR technique in this work. This indicates that bridge-bonded formate is one of the main reaction intermediates during methanol oxidation on Pd in alkaline solution.

Chapter 5

In situ spectroelectrochemical study of ethanol oxidation on Pd / XC-72 particles

5.1 Introduction to methanol oxidation on Pd

5.1.1 Pathways of methanol oxidation

The oxidation of methanol to carbon dioxide involves transfer of 6 electrons (Equation 5-1 and Equation 5-2) and offers a great opportunity for developing direct liquid fuel cells using methanol as the fuel.

In acid solution: $CH_3OH + H_2O \rightarrow CO_2 + 6H^+ + 6e^-$.....(5-1)

In alkaline solution: $CH_3OH + 6OH^- \rightarrow CO_2 + 5H_2O + 6e^-$.....(5-2)

The anode of the common direct methanol fuel cells (DMFCs) presently uses expensive and rare Pt-based catalysts for methanol oxidation under acidic conditions. However, the formation of CO_{ads} poisoning species during methanol oxidation via an indirect pathway in acid media poses a major challenge for use of Pt as the fuel cell catalyst (Figure 5-1).[115–117] It has been reported that Pt shows relatively good activity for catalysis of methanol oxidation in alkaline conditions due to weaker CO adsorption on the Pt surfaces.[36,118] Nowadays,

because of the successful development of alkaline anion-exchange membranes (AAEM),[32,34] interest in developing direct alkaline methanol fuel cells has grown quickly. In the past decades, the methanol decomposition and electro-oxidation at bulk Pt thin layers in both acidic and alkaline solutions have been extensively studied by *in situ* infrared spectroscopic techniques.[119–121] The mechanism of methanol oxidation on Pt is established as involving the parallel pathways (Figure 5-1). [24,117]

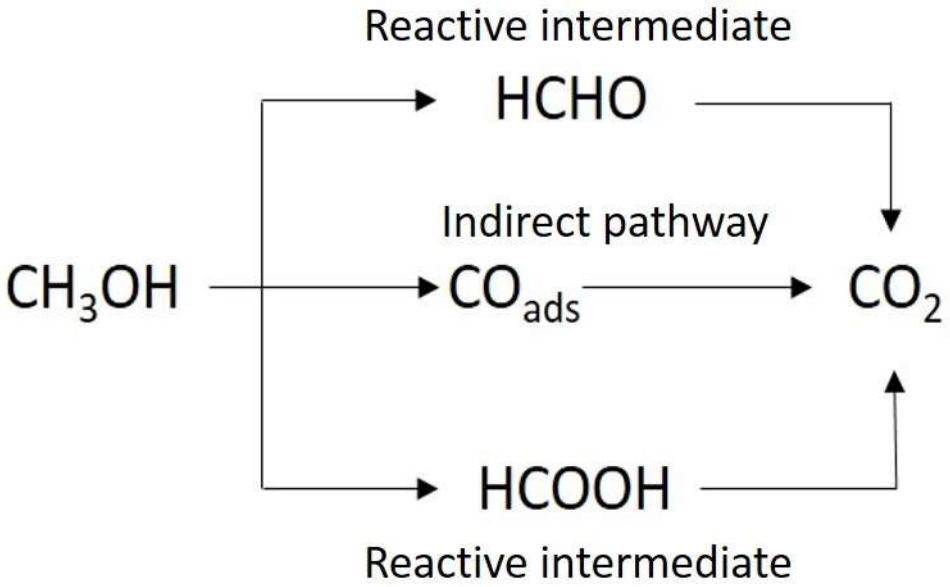


Figure 5-1 The parallel pathways of methanol oxidation proposed by the reference 116.

Palladium is more abundant in nature and sells at half the current market price of platinum. However, Pd shows very low activity for methanol oxidation in acidic conditions.[29] The spectroelectrochemical study in the chapter 4 suggests that CO_{ads} formation happens when there is a little amount of methanol present

in the reagent grade of formic acid in acidic conditions, providing a likely explanation for why the activity of methanol oxidation is low because the CO formation by methanol decomposition in acidic conditions is highly favoured. Recently, Pd has been found to have a good activity for methanol oxidation in alkaline conditions.[122,123] Therefore, the mechanistic study of methanol oxidation on Pd-based catalysts has attracted more and more interest in the past few years.

5.1.2 Previous infrared spectroscopic studies on Pd-catalysed electro-oxidation of methanol

There are very limited numbers of *in situ* IR spectroscopic mechanistic studies on methanol oxidation by Pd in alkaline solution. The first *in situ* IR spectroscopic study by Enyo et al.[37] on a Pd polycrystalline electrode was using electrochemically modulated infrared reflection spectroscopy and polarization modulated infrared reflection-adsorption. The study suggested that the CO_{ads} species produced by methanol oxidation are bridge-bonded to Pd sites instead of linearly bonded. These bridge-bonded Pd_2-CO species act as the surface poison and high potential is required for oxidative CO removal in alkaline solution. Very recently, the *in situ* IRAS and SEIRAS techniques were used to study methanol oxidation on thin layer bulk Pd metal in Cai group.[124] Their spectroscopic results suggested CH_3OH can be decomposed into CO_{ads} at a Pd electrode at open circuit potential and at potentials lower than ca. -0.10 V. [124]

The dissolved formate ($HCOO^-$) in solution was also found by IRAS as the intermediate and by-product of methanol oxidation. However, the adsorbed bridge-bonded formate was not detected, as in the cases for methanol or formic acid oxidation on Pt[119] or Pd in acidic solution.[97] Based on their results, Cai and co-workers proposed that the reaction pathway at the Pd electrode is to some extent similar to that at Pt electrodes in alkaline media. Nevertheless, a higher potential is required to oxidise the two intermediates (dissolved formate and CO_{ads}), and the conversion rate from formate to CO_2 at the Pd electrode is less than that at the Pt electrode, leaving more formate in the solution as the by-product in basic media.

In this chapter, the mechanism of methanol oxidation on Pd / XC-72 (Premetek) was studied by an *in situ* spectroelectrochemical approach in both acidic and alkaline environments.

5.2 IR Spectroelectrochemical study on methanol oxidation on Pd / XC-72 nanoparticles in acidic environment

To understand methanol oxidation on Pd / XC-72 in acidic conditions, the *in situ* SEC technique used in the previous chapters was also applied to this study. Cyclic voltammetry between 0 V and 1.2 V was first recorded in 0.5 M $HClO_4$ after electrochemically cleaning the catalyst surface with 10 potential scans in the SEC cell (Figure 5-2 red line). The typical hydrogen region, double layer

region and oxygen region indicate a clean surface (refer to section 3.1.1). Please note: the big hydrogen desorption peak (peak I in Figure 5-2) in the hydrogen region is due to the long electrochemical equilibrium time at low potential before the CV started. The 0.5 M $HClO_4$ with 0.1 M methanol was then pumped into the SEC cell for methanol oxidation. The low cathodic current in the cyclic voltammogram with methanol present suggests very little oxidation process in this potential range (0 V to 1.2 V) (Figure 5-2 black line). Moreover, the small changes of the peak I in the hydrogen region suggest no or very low coverage of poisoned Pd surface (Figure 5-2 black line) in the potential region. A slow increase of current was also observed in the double layer area. This can be explained as the very slow methanol oxidation via the direct pathway on the partially poisoned surfaces. The spectroelectrochemical study in chapter 4 suggested that CO_{ads} forms can be found when there is a little amount of methanol present in the reagent grade of formic acid in acidic conditions. Therefore, the formation of CO_{ads} in acidic condition can be expected here in a high concentration of methanol. The anodic peak II between 0.8 V and 1.0 V found in the voltammogram in Figure 5-2 is very similar to the anodic peak found in the CV of a CO pre-poisoned Pd surface (Figure 4-1). This suggests that the poison on the Pd surface is very likely to be CO. Another anodic peak III is observed at around 0.7 V during the negative potential sweep where the Pd-O / Pd-OH is reductively removed.

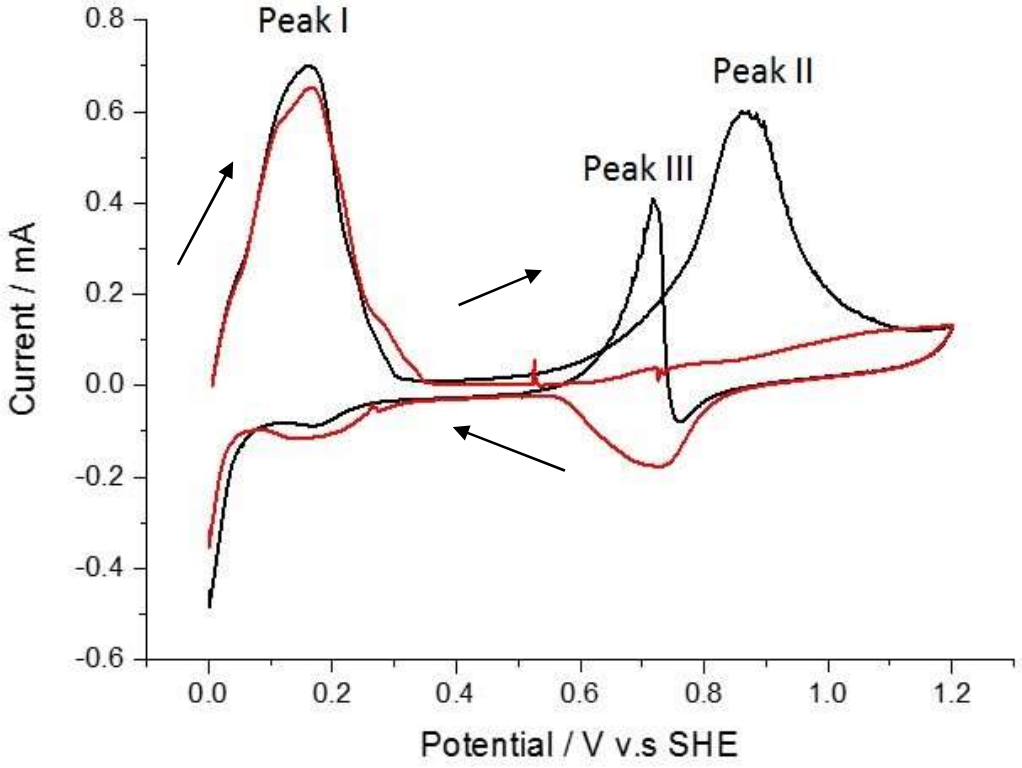


Figure 5-2 Red: Cyclic voltammogram of Pd / XC-72 in 0.5 M $HClO_4$. Black: Cyclic voltammogram of Pd / XC-72 in the 0.5 M $HClO_4$ containing 0.1 M CH_3OH. Both were recorded at a 1 mV sec^{-1} scan rate and 12 mL min^{-1} flow rate in the SEC cell.

Since the CO_{ads} has been oxidatively removed at high potential, the surface should be clean (not poisoned by CO_{ads}) for methanol oxidation via the direct pathway. However, similar to the case in formic acid oxidation on Pd and Pt, the formation of oxide / hydroxide on the metal surface results the low catalytic current in the high potential region. Peak III forms once the Pd-O and Pd-OH are removed on the backward scan, then the current decrease rapidly during the negative potential scan due to the reformation of CO_{ads}. Figure 5-3 shows the *in situ* ATR-IR spectra of the Pd electrode surface recorded simultaneously with

the voltammogram in Figure 5-2 (black). The *in situ* spectra also suggest that CO is the main poison. A broad band between 1700 and 1870 cm^{-1} was found in spectra recorded in the solution containing 0.1 M methanol in certain potential ranges. As discussed in section 4.2.2 this very broad band is assigned to overlap of the CO_H peak and the CO_M peak. Because of the broad shape of the band and change of water IR signal around 1645 cm^{-1}, it is very difficult to quantify the intensities of CO_H and CO_M peaks individually. Therefore, the integrated area between 1700 cm^{-1} and 1870 cm^{-1} is used to indicate the approximate intensity of the CO_{ads} peak. The peak height at 2341 cm^{-1} is used to present the intensity of solution phase CO_2 as described in chapter 3 and chapter 4. Figure 5-3B shows that CO_2 intensity tracks the catalytic current in the cyclic voltammogram indicating that CO_2 is the main product of the methanol oxidation catalysed by Pd / XC-72 in acidic conditions. The CO intensity decreases at high potential suggesting effective oxidative removal of CO on Pd. The gradual re-appearance of the CO peak when the current drops during the backward scan at peak III offers additional evidence of reformation of CO_{ads} as a poison.

To sum up, Pd has been reported as having very a low activity for methanol oxidation in acidic conditions. In this section, both electrochemical and spectroscopic data suggest that the low activity is due to the dominance of the indirect pathway in acidic conditions, causing the formation of CO_{ads}.

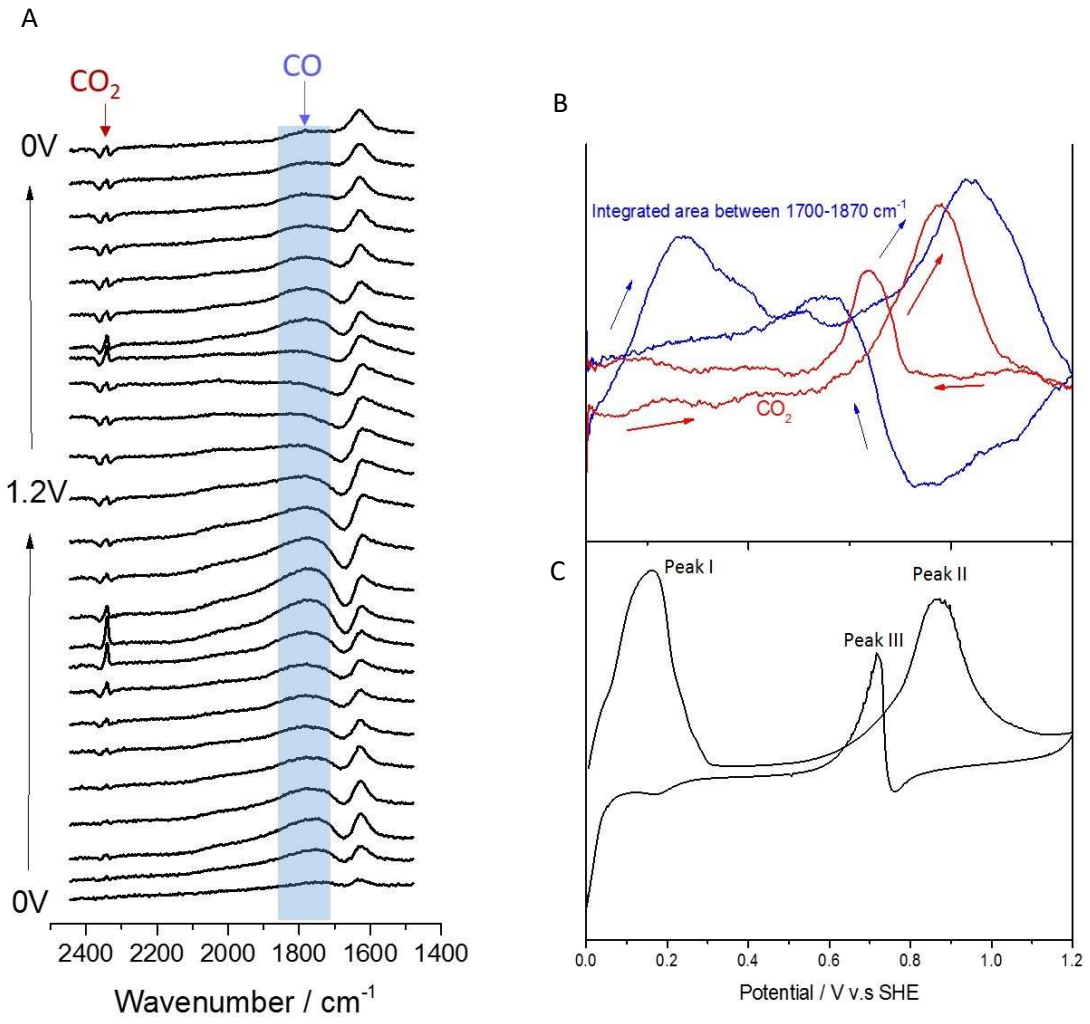


Figure 5-3 A: *In situ* ATR-IR spectra of Pd / XC-72 catalyst recorded simultaneously with the voltammogram in Figure 5-2 black line B: the integrated area between 1700-1870 cm^{-1}, indicative of CO peak intensity (blue) and the peak intensity of CO_2 during potential scan in Figure 5-2. C: the cyclic voltammogram recorded under methanol oxidation in the SEC cell reproduced from Figure 5-2.

Moreover, the formation of CO_{ads} must only occur when the potential is above 0.3 V since the hydrogen adsorption / desorption peaks are not missing in the cyclic voltammogram recorded with 0.1 M methanol present.

As introduced in Section 5.1, unlike in acidic conditions, the Pd has good activity for methanol oxidation in alkaline conditions. In the next section, methanol oxidation on Pd / XC-72 will be studied electrochemically and spectroelectrochemically.

5.3 Methanol oxidation on Pd / XC-72in alkaline solution

5.3.1 Cyclic voltammetry of Pd / XC-72 in alkaline solution

Before the *in situ* SEC measurement, the electrochemical properties of Pd / XC-72 in alkaline conditions were first characterised in conventional RDE measurement. Figure 5-4 shows the cyclic voltammogram of Pd / XC-72 on a glassy carbon RDE in 0.5 M KOH solution. Four main anodic peaks can be observed during the forward scan, which correspond to different electrochemical processes occurring on the Pd surface. Peak I in the potential range between −0.8 and −0.5 V is due to hydrogen desorption (Equation 5-3). Peak IV, which emerges above −0.1 V, can be attributed to the formation of the palladium (II) oxide layer on the surface of the catalyst.[125,126] Although the mechanism of this oxidation process remains unclear, it has been widely accepted that OH^- ions are first chemisorbed in the initial stage of the oxide formation, and then they are transformed into higher valence oxides at higher potentials. [127,128]

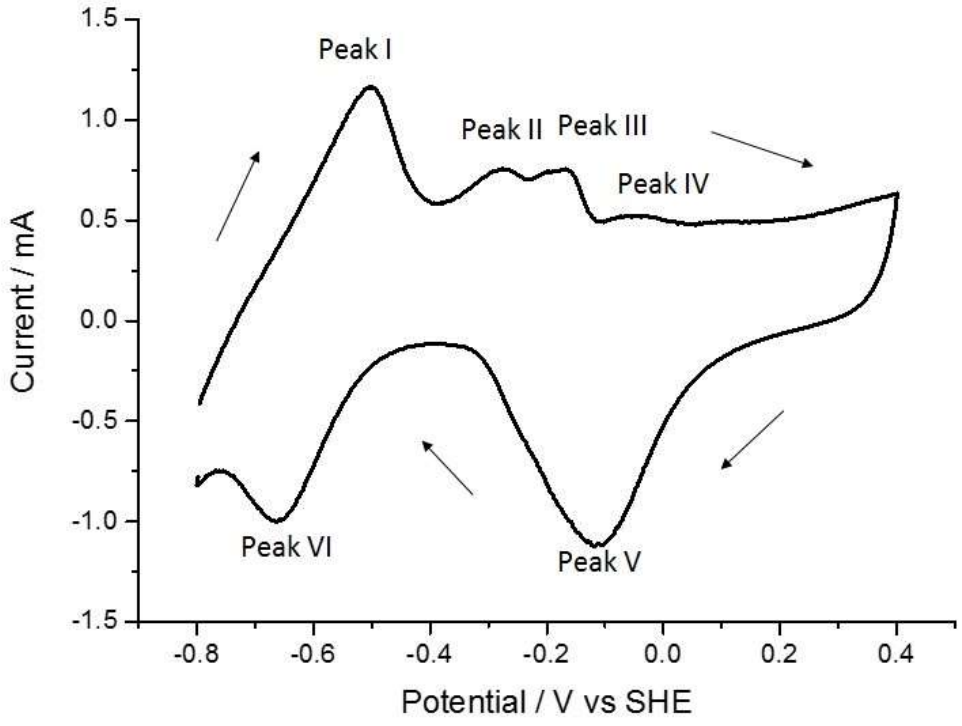


Figure 5-4 A cyclic voltammogram of Pd / XC-72 on a RDE electrode in 0.5 M KOH at 10 mV s^{-1} scan rate and 1000 rpm rotation rate.

$$Pd\text{-}H_{ads} + OH^- \rightarrow Pd + H_2O + e^- \quad (5\text{-}3)$$

$$Pd + OH^- \leftrightarrow Pd\text{-}OH_{ads} + e^- \quad (5\text{-}4)$$

$$Pd\text{-}OH_{ads} + OH^- \leftrightarrow Pd\text{-}O + H_2O + e^- \quad (5\text{-}5)$$

$$Pd\text{-}OH_{ads} + Pd\text{-}OH_{ads} \leftrightarrow 2Pd\text{-}O + H_2O \quad (5\text{-}6)$$

$$Pd\text{-}O + H_2O + 2e^- \leftrightarrow Pd + 2OH^- \quad (5\text{-}7)$$

The adsorption of OH^- on the Pd surface starts to occur at the negative potential and might partially overlap with hydrogen desorption peak (Equation 5-4). The

mechanism of formation of Pd-O is still not well established, but the peak II and peak III are very likely to result from the oxidation of Pd-OH (Equation 5-5 and 5-6).[127] The peak V, centred at -0.1 V, can be attributed to the reduction of Pd(II) oxide from the positive-going scan during the negative-going scan (Equation 5-7).[125–127] Peak VI is known to be associated with hydrogen adsorption.[125–127]

5.3.2 Cyclic voltammetry of Pd in 0.1 M methanol in alkaline solution

The cyclic voltammogram of Pd / XC-72 on a glassy carbon RDE in 0.5 M KOH containing 0.1 M methanol solution is shown in Figure 5-5. In the positive-going potential scan, the onset potential of methanol oxidation and first oxidative peak (Peak I in Figure 5-5) are located at ca. -0.2 and 0 V, respectively. The peak current in the forward scan is almost twice that in the backward scan, although the peak potential in the former (E_{pa} I = ca. 0 V) is slightly more positive than that in the latter (E_{pa} II = ca. -0.1 V).

It has been previously reported on the basis of IR spectroelectrochemistry studies by Sun and his co-workers that the anodic peak in the negative-going scan (Peak II in Figure II) is contributed by electro-oxidation of CO_{ads} which is formed during the positive-going scan.[129]

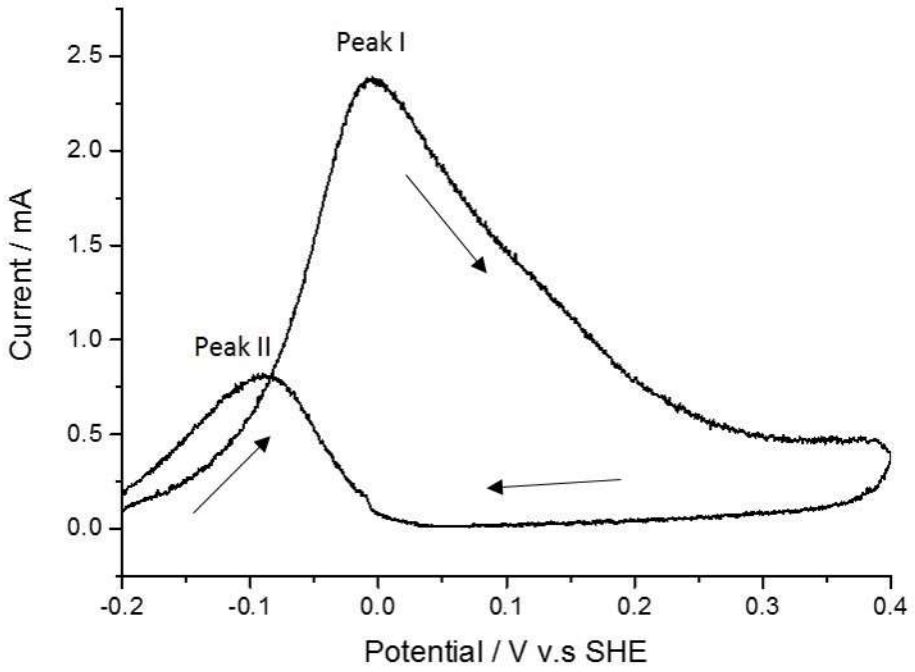


Figure 5-5 Cyclic voltammogram of Pd / XC-72 on a RDE in 0.5 M KOH containing 0.1 M methanol at 1 mV s^{-1} at 10 mV s^{-1} scan rate and 1000 rpm rotation rate.

The i_{pa} of peak I (i_{pa} I) is around 2.4 mA and the i_{pa} of peak II (i_{pa} II) is around 0.75 mA. The ratio of the i_{pa} in positive scan to the i_{pa} of the negative scan (i_{pa} I / i_{pa} II) is generally used as the index of the CO tolerance for catalysts.[123,124,130] The higher the ratio, the better the tolerance to CO poisoning, while the lower the ratio, the more likely that the catalyst is poisoned. The ratio found here with this Pd / XC-72 is around 3.2 which is higher than for bulk Pd metal (the ratio is around 2) [124] and similar to the other studies on supported Pd catalysts (the ratios are between 2.6 to 3.4).[123,130]

To sum up this section, the electrochemistry characterisation of this Pd / XC-72 particles suggests that these particles shows typical electrochemical features in alkaline conditions. Moreover, these particles shows similar CO tolerance to another supported Pd nano-materials which have been reported previously.[123,130]

In the next section, the SEC setup was used for further understanding of the mechanism of methanol oxidation on this commercial Pd / XC-72 catalyst.

5.3.3 *In situ* spectroelectrochemistry of methanol oxidation on Pd in alkaline solution

To obtain more mechanistic information on methanol oxidation on Pd / XC-72, a similar *in situ* IR spectroelectrochemical technique was used in this study. The *in situ* measurement on the Pd / XC-72 in 0.5 M KOH containing 0.1 M methanol was conducted as the potential was scanned from -0.2 to 0.4 V and then back to -0.2 V. Figure 5-6 shows IR spectra recorded under different electrochemical potentials with reference to the spectrum recorded at -0.2 V before methanol solution was flowed into the SEC cell. Several peaks can be found at the starting potential of the CV at -0.2 V. In Figure 5-6, the sharp peak at 1581 cm^{-1} present from -0.2 V could be assigned to the ν_{as}(OCO) band of dissolved formate ($HCOO^-$).[120,131] The broad band with the peak located at 1385 cm^{-1} from -0.2 V

has been reported to arise from the dissolved carbonate / bicarbonate species (CO_3^{2-} / HCO_3^-) in the recent studies.[124,132,133]

Table 5-1 A selection of wavenumbers of infrared signals of relevant species reported in the literature

Wavenumber / cm^{-1}	Species
1815 – 1870 cm^{-1}	Hollow-bound CO $\nu(CO_H)$ on Pd [97]
1600-1645 cm^{-1}	δ(H-O-H) of solution H_2O[134]
1581 cm^{-1}	ν_{as}(OCO) band of $HCOO^-$ [24]
1385 cm^{-1}	δ(C-H) band of $HCOO^-$ [131]
1350 cm^{-1}	ν_{as}(OCO) band of $HCOO^-$[135]
1323 cm^{-1}	ν_s(OCO) band of adsorbed formate ($HCOO_{ads}$) [97]

The ν_{as}(OCO) of solution CO_2 at 2343 cm^{-1} that was observed in both formic acid oxidation and methanol oxidation in acidic solution was not found since the pH of 0.5 M KOH is much high than the pKa of CO_2. Therefore, the dissolved CO_2 will exist mainly as either CO_3^{2-} or HCO_3^-. However, the IR signal at 1385 cm^{-1}

was also found at lower potential where the catalyst is not active. This indicates that the peak is not contributed by carbonate / bicarbonate species. The vibrational signal of the C-H bond, δ(C-H) of $HCOO^-$ has also been reported to be located at 1382 cm^{-1},[135] therefore the band is assigned as another piece of evidence of production of $HCOO^-$ from methanol decomposition.

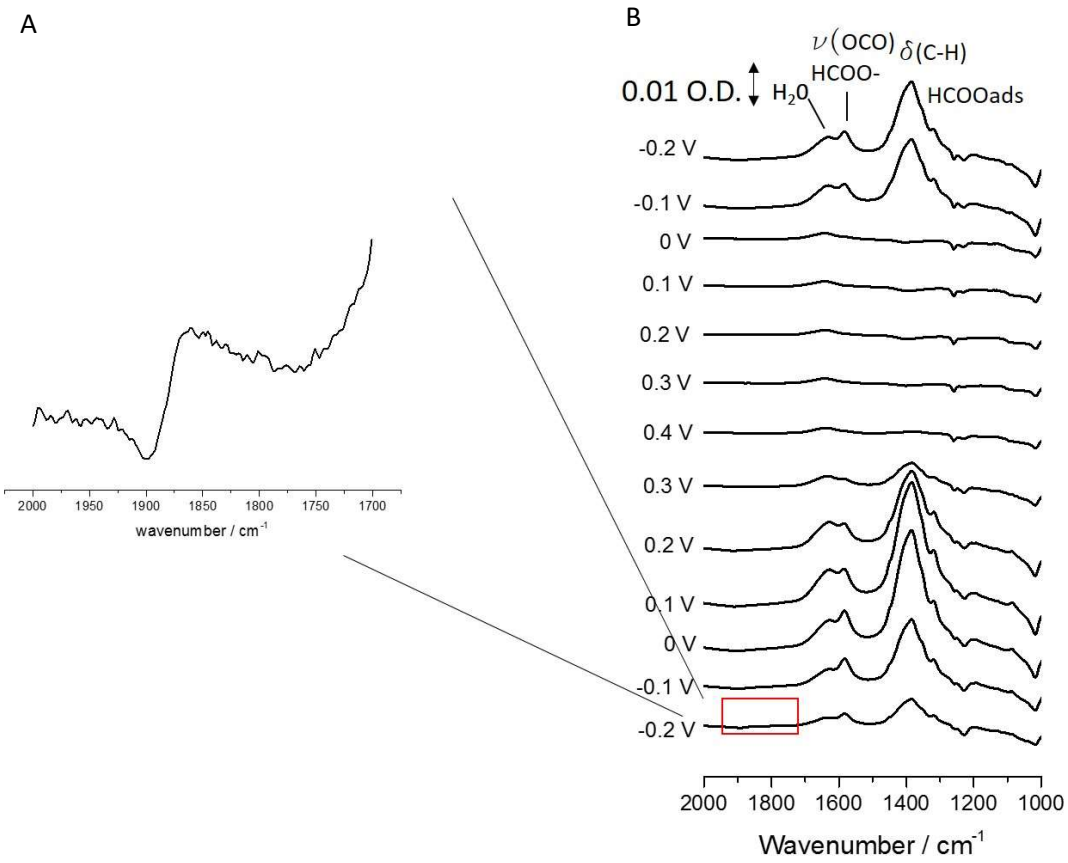


Figure 5-6 A: The amplified spectrum between 1700-2000 cm^{-1} at -0.2 V B: ATR-IR spectra of the Pd / XC-72 recorded simultaneously with the voltammogram in Figure 5-7 black line

The peak at 1323 cm^{-1} has not been detected previously in methanol oxidation on any Pd surface by IR techniques such as SEIRAS or IRAS but is expected to be located around 1320 cm^{-1}. [97,108,124] A similar peak was also observed by another group member in spectroelectrochemical study of formic acid oxidation on Pt.[105] In his work, a potential-dependant peak 1315 cm^{-1} was found and assigned as $\nu_{s(}$OCO) of bridge-bonded formate ($HCOO_{ads}$). Therefore, this 1323 cm^{-1} peak observed here is assigned to the bridge-bonded formate on Pd. A relatively less intense peak at around 1860 cm^{-1} was also found in the spectra (Figure 5-6A). This is the wavenumber of hollow bound CO (CO_H) which is consistent with reported by Enyo et al.[37] that the CO_{ads} formed by methanol oxidation is bridge-bonded or multi-bonded on Pd instead of linearly bound.

The intensities of these peaks are summarised in Figure 5-7. The peak intensities of both dissolved ($\nu_{as(}$OCO) and δ(C-H)) (Figure 5-7, brown, red)and adsorbed formate ν_s(OCO) (Figure 5-7, green) tracks the catalytic current of methanol oxidation (Figure 5-7, black). This indicates that formate acts as the reactive intermediate or the product of the electro-oxidation of methanol. As the potential is swept more positive, the CO_{ads} starts to be electro-oxidised at ca. -0.15 V and is then completely consumed at a potential above ca. 0.1 V (Figure 5-7 blue), close to the anodic stripping of the adsorbed CO ad-layer at the Pd electrode as reported previously.[37,124]

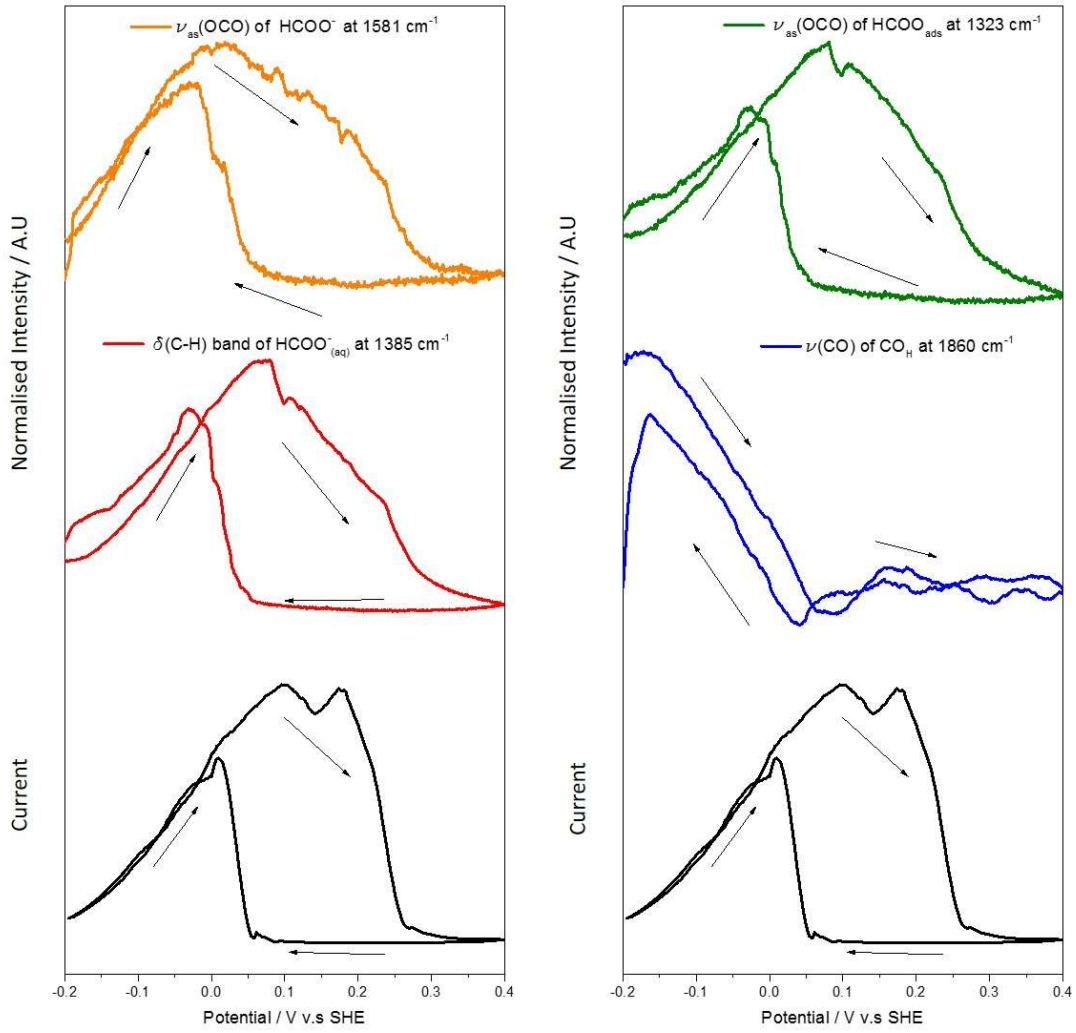


Figure 5-7 The infrared peak intensities of different IR signals during potential scan. ν_{as}(OCO) band of HCOO$^-$ (brown), δ(C-H) band of HCOO$^-$ (red), ν_s(OCO) band of HCOO$_{ads}$ (green) and ν(CO$_H$) of hollow-bound CO (blue). The cyclic voltammogram recorded under of methanol oxidation in the SEC cell in 0.5 KOH + 0.1 M methanol (black)

The CO_{ads} species regenerates from CH_3OH adsorptive decomposition at ca. 0.05 V during the negative-going scan from the vertex potential of 0.4 V, accompanied by the reduction of the surface oxide.

To sum up here, the observation of ν(CO) at 1860 cm^{-1} and ν_{as}(OCO) band of dissolved formate at 1581 cm^{-1} suggests both CO_{ads} and formate act as the two intermediates during electro-oxidation of CH_3OH at Pd / XC-72 in alkaline media. This is consistent with the previously proposed reaction pathways for CH_3OH oxidation at the Pt electrode in both acidic and alkaline media.[120,121] . The ν_s(OCO) band of $HCOO_{ads}$ around 1323 cm^{-1} on Pd was detected for the first time by an *in situ* IR technique. This offers promising evidence to support the proposed mechanism that the bridge-bonded formate is a significant reaction intermediate during methanol oxidation on Pd.[89106136] Moreover, the ν_s(OCO) band of $HCOO_{ads}$ are much more intense the $\nu(CO_{ads})$ indicating the reaction more favours formate pathway over the CO pathway.

The electrochemical potential for methanol decomposition to formate was also studied using the *in situ* measurements (Figure 5-8). The potential was first held at -0.8 V in KOH containing CH_3OH where the hydrogen adsorbed on the Pd surface strongly preventing CH_3OH adsorption and decomposition. The potential was then stepped to -0.6 V for 900 seconds and a difference spectrum was recorded using the -0.8 V spectrum as background. The typical derivative shape of the CO_{ads} peak found in this Thesis can be observed in the CO region. When the potential was stepped to -0.4 V the δ(C-H) of dissolved formate at 1385 cm^{-1} starts to increase. The peak of ν(OCO) of dissolved formate at 1581 cm^{-1} was not obvious because it overlaps with the broad δ(H-O-H) peak of water

around 1650 cm^{-1}, and there are slight changes in water content or pathlength as the potential is varied.

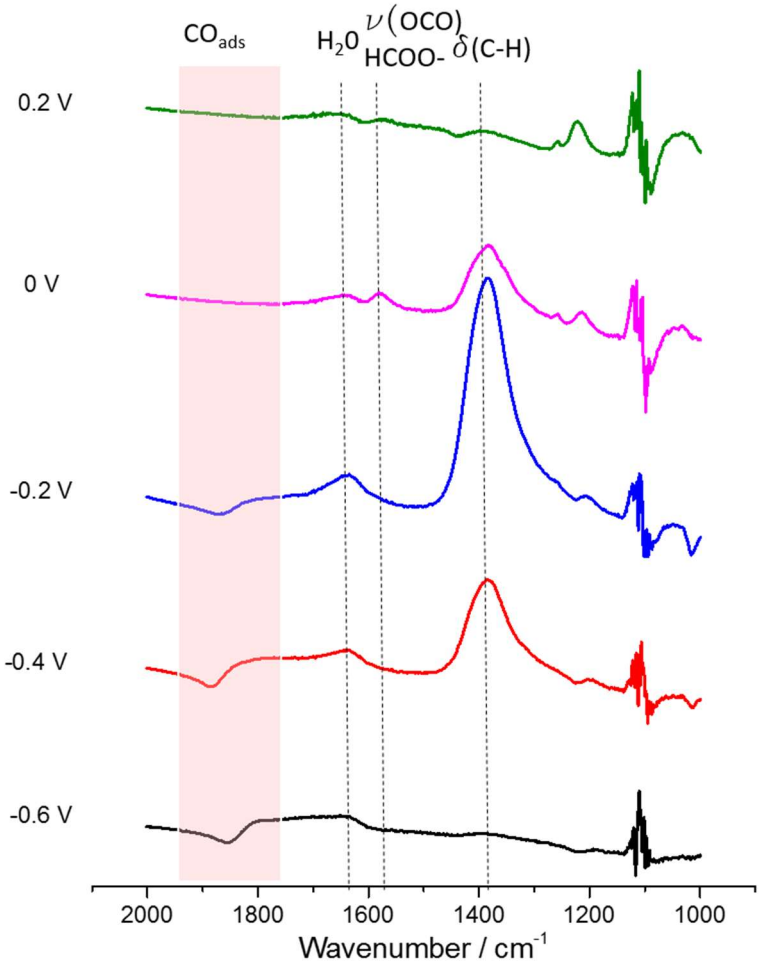


Figure 5-8 Difference spectra recorded at different potentials in 0.1 M methanol, processed using the initial spectrum at -0.8 V as reference.

The formation of CO_{ads} from the dehydrogenation of methanol to CO can occur even at the potentials as low as -0.6 V. Interestingly, the formation of formate required the more positive potentials (-0.4 V to -0.2 V) where the oxidation of

Pd-OH occurs (Equation 5-2 and Figure 5-4). This might imply that the oxidation of methanol to formate requires surface oxide.

5.4 Discussion

In this chapter, methanol oxidation on the Pd / XC-72 was studied in both acidic and alkaline conditions. Cyclic voltammetry of Pd / XC-72 in 0.5 M $HClO_4$ containing 0.1 M methanol shows very low catalytic current suggesting Pd / XC-72 has a low activity for methanol oxidation in acidic conditions, which is consistent with reports in the literature.[29] The strong CO_{ads} was found in the *in situ* spectra at potentials above 0.3 V in the positive-going scan of the CV. This explains why there is a low activity for methanol oxidation on Pd in acidic conditions because of the dominance of the CO pathway in methanol oxidation in acidic conditions.

In alkaline conditions, high catalytic current in the potential scan suggests that Pd / XC-72 has a high activity for methanol oxidation. The observation of ν(CO) at 1860 cm^{-1}, ν_{as}(OCO) band of $HCOO^-$ at 1581 cm^{-1} and δ(C-H) of $HCOO^-$ at 1385 cm^{-1} during the potential scan indicates both CO_{ads} and formate act as the intermediates for electro-oxidation of methanol on Pd / XC-72 in alkaline media. The formate peaks produced during methanol oxidation show very high similarities to the peaks in the formic acid spectrum in alkaline solution (Figure 5-9). This double confirmed the peaks assignment that 1581 cm^{-1} and 1385 cm^{-1}

peaks are contributed by formation of $HCOO^-$ via methanol oxidation and suggests the dual pathway is very likely to go through the formate pathway in alkaline environment.

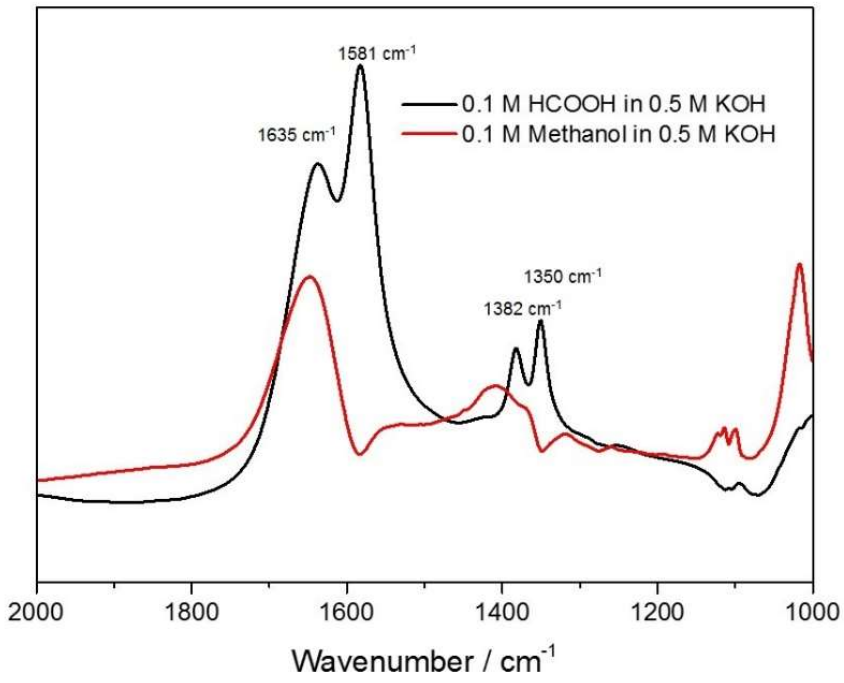


Figure 5-9 IR spectra of black: 0.1 M 0.1 M HCOOH + 0.1 M KOH red: 0.1 M methanol + 0.5 M KOH. Both against the spectra taken with 0.5 M KOH.

An IR band at 1323 cm^{-1} was detected and assigned as ν_s(OCO) of $HCOO_{ads}$ for the first time in methanol oxidation on Pd-based catalyst in alkaline conditions. The absence the ν_s(OCO) of $HCOO_{ads}$ band in formic acid solution in alkaline conditions offers another piece of evidence that the peak comes from an adsorbed species instead of solution species. This offer a promising evidence to support the proposed mechanism the bridge-bonded formate is one of the main reaction

intermediates during methanol oxidation on Pd. [89106136] Please note: the 1350 cm^{-1} in Figure 5-9 is assigned as ν_s(OCO) of $HCOO^-$. The absence of this peak in Figure 5-8 and Figure 5-6B might be due to it overlaps with δ(C-H) of dissolved formate.

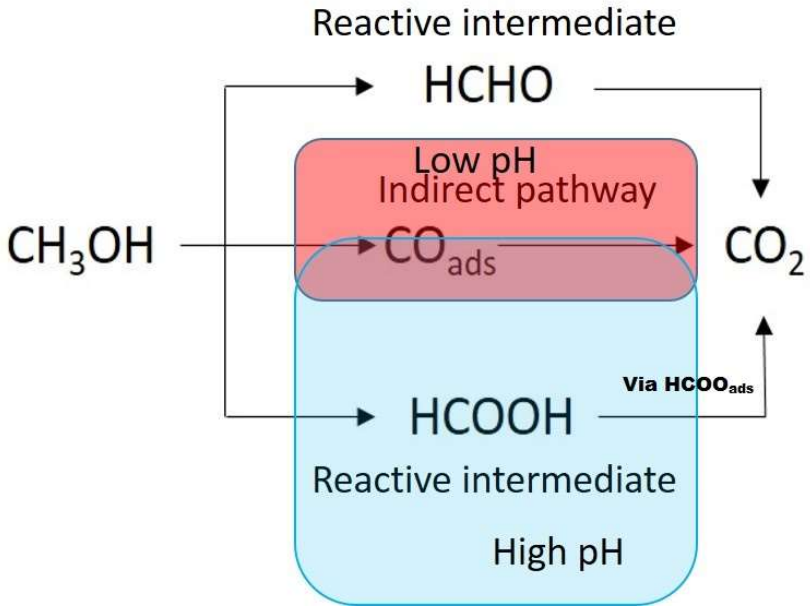


Figure 5-10 The parallel pathways of methanol oxidation on Pd.[117] The blue region presents the idea that in alkaline conditions the methanol oxidation mainly goes though the formic acid pathway. The reaction also goes through the CO pathway, but this is much less favourable. The red region presents the idea that in acid solution methanol oxidation is dominated by the CO pathway.

The very weak ν(CO) IR signal suggests, CO_{ads} act as a short-lived intermediate or the CO pathway is much less favourable than the formate pathway. The typical ν(C=O) of formaldehyde was not detected indicate the no formaldehyde or very little formaldehyde was produced.

Chapter 6

Abstract

In this Chapter, a catalytic cascade system for CO_2 electro-reduction to hydrocarbons was preliminarily designed. The key idea of the design is that setting up a composite system with the mixture of Cu nanoparticles and CODH enzymes allows the rate-determining step, CO_2 reduction to CO, to be accelerated by CODH, thus increasing the whole turnover rate of CO_2 reduction to hydrocarbons. By immobilising both copper nanoparticles and CODH onto carbon black particles, the preliminary results show more effective electrocatalysis of CO_2 reduction at mild overpotential compared to copper alone on carbon. Future studies will focus on the optimisation of the ratio of Cu and CODH and on the reaction in the different electrolytes, along with the determination of the product distribution.

Chapter 6

Electrochemical conversion of carbon dioxide into hydrocarbon feedstock

6.1 CODH / Cu particle system

As introduced in section 1.4, copper is the most promising metal that is able to catalyse CO_2 and CO reduction to hydrocarbons such as methane, ethylene, formic acid and methanol.[71,73] As discussed in section 1.4.2, the conversion between CO_2 and CO on a Cu electrode requires high overpotential which limits the turnover rate of CO_2 electro-reduction at moderate potentials.[71–74] CODH has great activity for CO_2 / CO conversion with a midpoint potential around -0.53 V[76,79] which is very close to the thermodynamic potential of CO_2 reduction to CO. Recently, a cascade electrocatalyst system by combining noble metals and enzymes for electro-reduction of nitrate to ammonia has been reported by Vincent group.[137] The result shows higher activity for nitrate reduction to ammonia on Pt / C and Rh / C catalysts when the enzyme (nitrate reductase) is present since the enzyme accelerates the rate-determining step in the reaction pathway.[137]

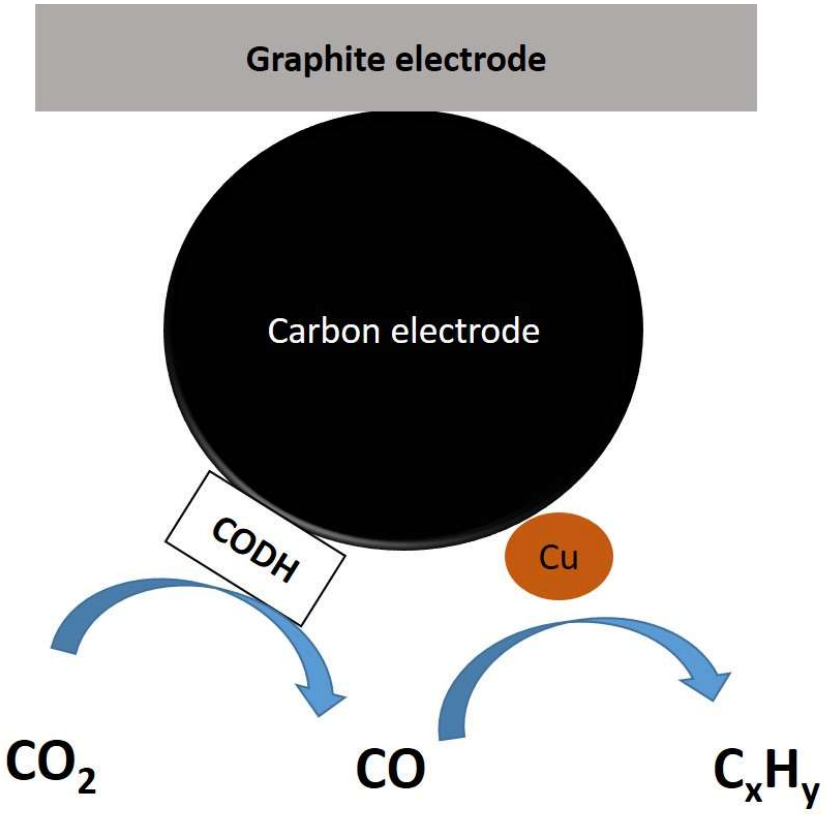


Figure 6-1 A schematic illustration for the composite electrocatalyst system for CO_2 reduction to hydrocarbons.

The idea here in this chapter is to set up a composite electrocatalyst system with a mixture of Cu nanoparticles and CODH enzyme as shown in Figure 6-1. This allows the rate-determining step at Cu, CO_2 reduction to CO, to be accelerated by CODH, and therefore increases the whole turnover rate of CO_2 reduction to hydrocarbons.

6.1.1 BP 2000 supported CODH

A number of metalloenzymes have been reported to be able to be immobilised on carbon materials (either through covalent attachment or direct adsorption)

allowing them to be electrochemically controlled over a wide potential range with more efficient electron transfer with the working electrode.[138] In the Vincent group, the method of supporting metalloenzymes by high surface area carbon materials havs been developed and been proven to enhance electrochemical response of metalloenzymes such as hydrogenases on a PGE electrode.[139,140] Here, CODH was absorbed on a high surface area carbon material for the same purpose. The carbon particle type used as the supporting material for CODH in this study is "black pearl" 2000 (BP 2000) purchased as powder from Cabot Corporation.

Because CODH is extremely oxygen sensitive, all the procedures for enzyme absorption onto carbon particles were required to be operated in an anaerobic glove box (Glove Box Technlogy, Ltd.). BP 2000 was used as water dispersion at 20 mg of BP 2000 per mL of Milli Q water. The CODH enzyme solution (having an approximate concentration of 200 μM) was mixed with the BP 2000 dispersion with 1:1 ratio after the BP 2000 particles dispersion had been sonicated for 1 hour to ensure being well dispersed. The enzyme-particle mixture was then kept in an icebox for 2 hours to allow for enzyme adsorption. After washing the particles 3 times to remove the excess enzyme by centrifugation, removing the supernatant and then remixing with pH 6.0, 50 mM MES buffer, the enzyme adsorbed particles were ready to be used.

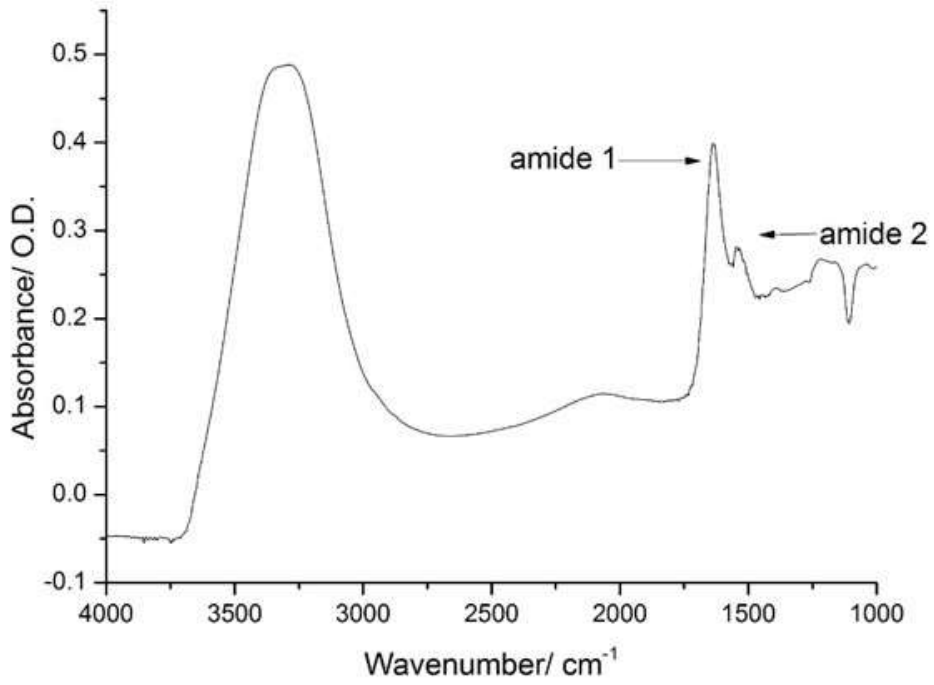


Figure 6-2 Different spectrum of 1 μL film of BP 2000 supported CODH dispersion using the spectrum taken with Si prism as background. The clear amide 1 band at 1645 cm^{-1} and amide 2 band at 1550 cm^{-1} indicates the existence of protein of the carbon particles.

Infrared spectroscopy was used to confirm the enzyme adsorption. One μL of BP 2000 supported enzyme particle dispersion was deposited onto a Si IRE by drop-casting method and allowed to dry. The cell was assembled as described in chapter 2. Two clear peaks at 1645 cm^{-1} and 1550 cm^{-1} were found and assigned as amide I and amide II respectively (Figure 6-2), implying significant enzyme adsorption onto BP2000.

6.1.2 Supporting copper nanoparticles on BP 2000

BP 2000 was also used to support Cu nanoparticles. Copper (Cu) nanopowder (99.9%, 40 nm, metal basis) from US nanomaterials was used for making a Cu nanoparticle dispersion. To avoid formation of copper oxide by reaction between Cu nanoparticles with O_2 in the air, the Cu nanoparticles, BP 2000 particles and solutions used for making BP 2000 supported Cu nanoparticles suspension were stored and prepared in a glove box. To make the Cu dispersion, Cu nanoparticles were mixed with Milli Q water at a loading of 20 mg of Cu nanoparticles per mL. First, the dispersion was sonicated for one hour; then, the dispersion was diluted by Milli Q water for 100 times to make a final "concentration" of 200 μg per mL. The Cu particle dispersion was then mixed with a BP 2000 dispersion (20 mg mL^{-1}) with 1:1 ratio and then followed by an extra hour of sonication. The mixture of Cu nanoparticles and BP 2000 particles dispersion was then stored at 4 °C for overnight while the adsorption took place. After washing out the excess Cu particles by centrifugation, removing the supernatant and then remixing with pH 6.0, 50 mM MES buffer for three times, the BP 2000 supported Cu particles were ready to be used.

6.2 Electrochemistry of BP 2000 supported CODH and Cu

6.2.1 BP2000 supported CODH

For electrochemical characterisation, 0.5 μL of BP 2000 supported enzyme particle dispersion deposited onto a PGE electrode. The cyclic voltammetry of BP 2000 supported CODH under 100 % CO atmosphere is shown in Figure 6-3. The potential was cycled between -0.8 V and 0.2 V at a scan rate of 10 mV s^{-1} under 100% of CO in 50 mM pH6.0 MES buffer.

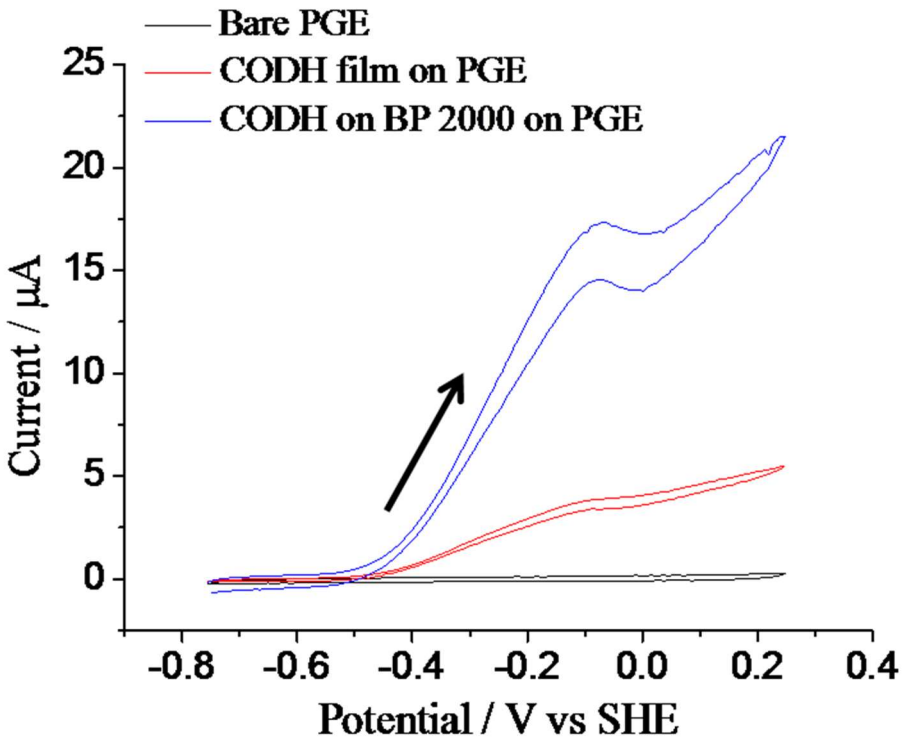


Figure 6-3 Protein film voltammetry of CODH under 100 % CO. Rotation rate: 1000rpm, scan rate: 10 mV s^{-1}.

The clear anodic current with an onset potential around -0.5 V can be ascribed to the electro-oxidation of CO. The result is consistent with previous PFE studies [77,84,141], suggesting that the enzyme is stable and fully functional on the BP 2000 particles. The catalytic CO oxidation current observed from CODH adsorbed BP 2000 is about five times the current measured on a flat PGE electrode (Figure 6-3).

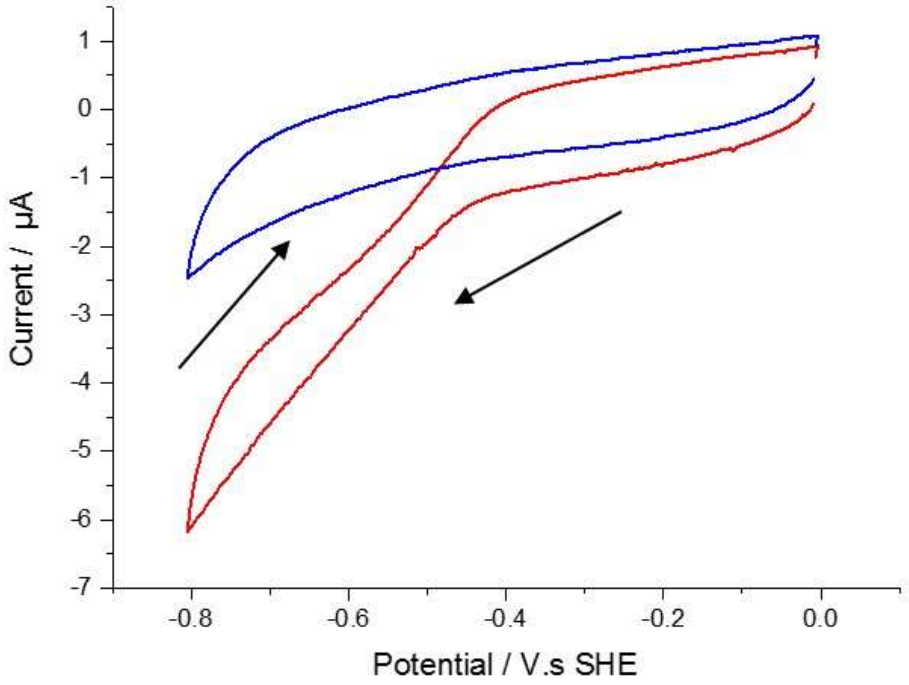


Figure 6-4 Protein film voltammetry of CODH: blue: CODH on BP 2000 on PGE under 100 % N_2, red: CODH film under 100% CO_2 on PGE. Rotation rate: 1000 rpm, scan rate: 10 mV s^{-1}.

This suggests a higher enzyme loading on the BP2000 modified electrode, as expected, while also showing that electrons can be transferred to the enzyme very efficiently. Secondly, the potential was cycled between 0 V and -0.8 V under

100% of CO_2 to investigate CO_2 reduction. The negative current with the onset potential at around -0.5 V arises from the electro-reduction of CO_2 to CO (Figure 6-4). This is also consistent with the literature. The onset potentials of both CO oxidation and CO_2 are very close to the thermodynamic potential of CO_2 reduction to CO, also agreeing with assertion that "CODH is a great catalyst for interconversion of CO and CO_2" as reported in the literature.[84]

6.2.2 BP2000 supported Cu nanoparticles

Cyclic voltammetry was also used for testing BP2000 supported Cu nanoparticles.

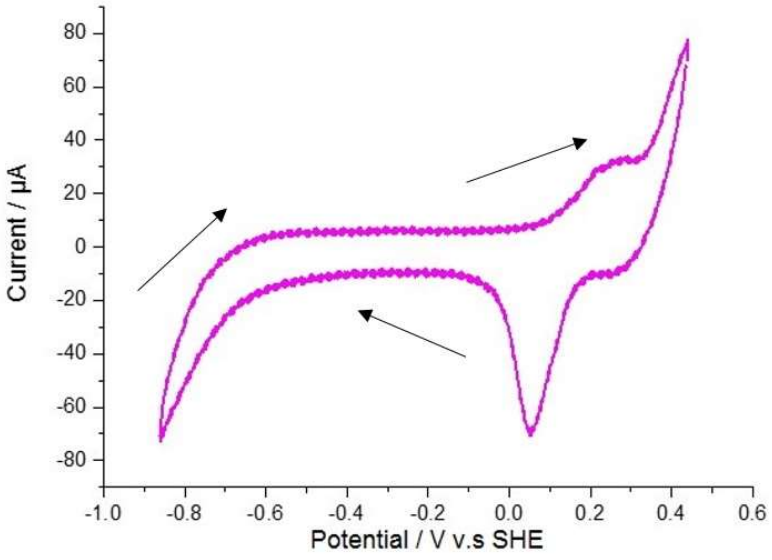


Figure 6-5 The cyclic voltammogram of BP 2000 supported Cu nanoparticles on a PGE electrode. Scan rate: 50 mV sec^{-1} Rotation rate: 1000 rpm. The CV shows typical features of Cu nanoparticles suggesting Cu nanoparticles are well supported on BP 2000.

The cyclic voltammogram in Figure 6-5 was recorded in N_2 - saturated 50 mM pH 6.0 MES buffer. The positive peak around 0.2 V is due to the formation of Cu_2O as reported previously[142] and the negative peak near 0.05 V is from Cu_2O reduction to Cu as Equation 6-1:

$$Cu_2O + H_2O \rightarrow 2Cu + 2OH^- + 2e^- \quad \text{.....(6-1)}$$

The cathodic current occurring at a potential lower than -0.6 V is from the formation of H_2 via proton reduction as expected.[72] These clear electrochemical features indicate the successful preparation of functioning carbon supported Cu nanoparticles.

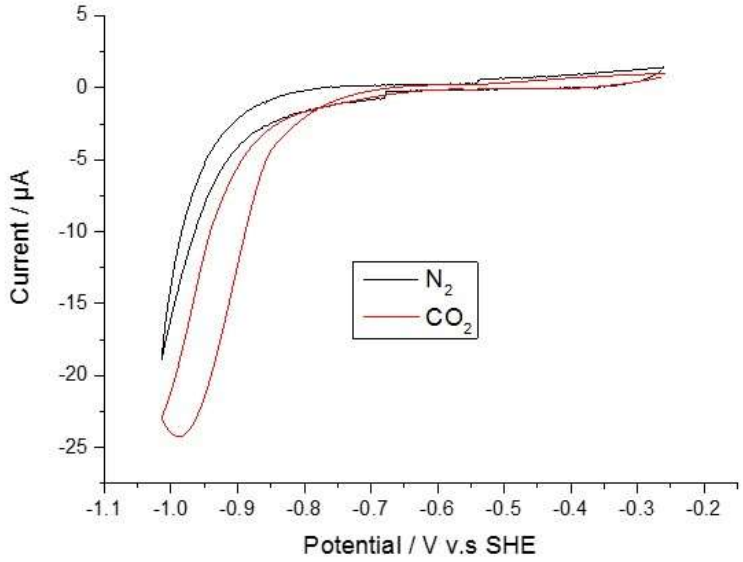


Figure 6-6 The cyclic voltammetry of BP 2000 supported Cu under 100 % N_2 (black), 100 % CO_2 (red) atmosphere in pH 6.0 50 mM MES buffer at 10 mV s^{-1} scan rate and 1000 rpm rotation rate.

The BP 2000 supported Cu particles were then tested for CO_2 reduction potential scans under CO_2 atmosphere. As shown in Figure 6-6, compared with the CV under N_2 atmosphere, the more negative current in the low potential region (more negative than ca. -0.7 V) under CO_2 atmosphere can be explained by reduction of CO_2 to CO and other hydrocarbon species.[72,74]

The CO adsorption peaks at potentials between -0.9 V and -1 V reported by Hori et al were not observed.[71,72] This might be caused by the peaks overlapping with the very negative peak from proton reduction. The different temperature condition might be another possibility since Hori's work was carried out at low temperature, close to 0 °C.

6.2.3 Cascade system for CO_2 reduction

To assemble a combined catalyst including CODH and the Cu nanoparticles, it would be ideal to immobilise both CODH and Cu onto the same particles. The enzyme solution and a dispersion of BP 2000 supported Cu nanoparticles were mixed together at a 1:1 volume ratio, and then kept at 4 °C for overnight. Figure 6-7B shows the BP 2000 supported Cu / CODH under 100 % CO_2 and 100 % N_2 atmospheres. The voltammetric profiles under 100 % N_2 in Figure 6-7B (black line) is in good agreement with that of Cu immobilised on BP2000 in the absence of CODH (Figure 6-7A, black line), suggesting that immobilisation of CODH would not change the stability of Cu nanoparticles on BP2000. Under 100 % CO_2 atmosphere, a larger negative current at the potential lower than -0.7 V can be

observed in the presence of CODH (Figure 6-7B, red line) compared to the CV that CODH is absent (Figure 6-7A, red line). This indicates that more reductive reactions occur in the potential region more negative than -0.7 V and the electro-reduction of CO_2 might be accelerated by CODH.

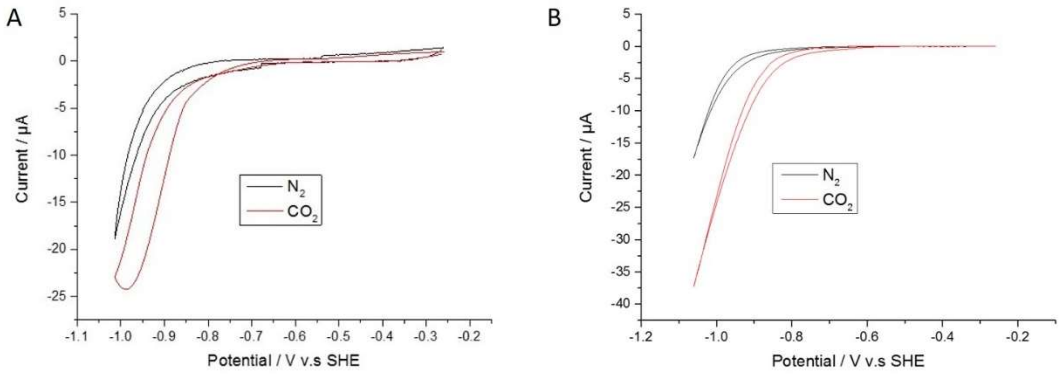


Figure 6-7 A: The cyclic voltammetry of BP 2000 supported Cu under 100 % N_2 (black) and 100 % CO_2 (red) atmosphere, reproduced from Figure 6-6. B: the cyclic voltammetry of BP 2000 supported Cu / CODH under 100 %N_2 (black), 100 % CO_2 atmosphere. All the CVs were recorded at 10 mV s^{-1} scan rate and 1000 rpm rotation rate.

Figure 6-8 shows a comparison of negative-going potential sweeps of BP 2000 supported Cu and BP 2000 supported Cu / CODH under 100 % CO_2 atmospheres. A larger negative current in the potential region around -0.5 V can be observed in the presence of CODH. This indicates that CODH is adsorbed alongside Cu particles that it can reduce CO_2 around -0.53 V is the potential where CODH can reduce CO_2 but Cu cannot.

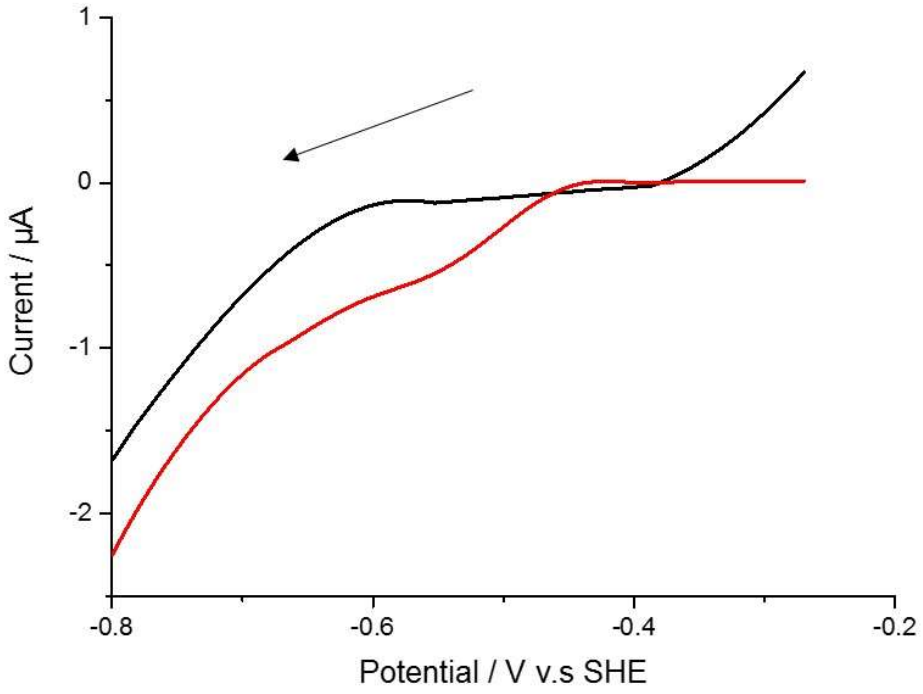


Figure 6-8 The potential sweep of BP 2000 supported Cu (black) and BP 2000 supported Cu / CODH (red) under 100 % CO_2 atmosphere at 10 mV s^{-1} scan rate and 1000 rpm rotation rate.

6.3 Discussion and outlook

Copper is the most promising transition metal that can catalyse formation of hydrocarbons such as methane, ethylene, formic acid and methanol from electro-reduction of CO_2. Evidence from published spectroelectrochemical IR data shows that CO is a reaction intermediate, and it adsorbs onto Cu.[74] The published electrochemical and spectroscopic results suggested that CO formation from CO_2 on copper requires a higher overpotential.[74] Therefore, the CO_2 reduction to CO can be considered as the rate-determining step for the

whole reaction of CO_2 reduction to hydrocarbons. The enzyme CODH can catalyse the reduction of CO_2 to CO with a near-zero overpotential. Therefore, the use of CODH for CO formation via CO_2 reduction to relay CO to Cu for further hydrogenation reactions is in principle a promising approach to enhance reaction rates. The preliminary electrochemical results in this chapter suggest that both CODH and Cu can be "supported" on carbon black particles BP 2000 and that both of them are stable and fully functional on the carbon particles. Furthermore, this strategy allows the careful control of the amount of the Cu and CODH adsorbed onto BP2000. The electrochemical data are encouraging, showing that CODH enhances CO_2 reduction with the onset potential close to the thermodynamic potential of CO_2 / CO conversion.

In this work, preliminary results on the combination of CODH and Cu were presented. Future studies will focus on the optimisation of the ratio of Cu and CODH and on the reaction in the different electrolytes, along with the determination of the product distribution by chromatographic techniques. Moreover, the *in situ* ATR-IR spectroelectrochemical technique used to investigate carbon supported Pd nanocatalyst can be extended to study the mechanism of this composite catalyst in the future.

Chapter 7

Conclusion and outlook

7.1 Conclusion

The supported metal nanoparticles are widely used as the catalysts for fuel cell anodic reactions such as hydrogen oxidation, methanol oxidation and formic acid oxidation. In this Thesis, an *in situ* ATR-IR spectroelectrochemical (SEC) approach for investigation of supported metal nanocatalysts was developed and used for the mechanistic studies of formic acid oxidation and methanol oxidation on carbon supported palladium nanocatalysts.

Chapter 3 is mainly focused on establishment of the SEC method for studying formic acid oxidation on carbon supported nanoparticles. Two commercial catalysts, Pd / C (Sigma-Aldrich, 10 wt. % loading, matrix activated carbon support) powder and Pd / XC-72 nanoparticle (Premetek, USA, 60% Pd / XC-72) were used to test the experimental setup for *in situ* spectroscopy. The unexpected observation of CO_{ads} and the CO_{ads} behaviour observed via *in situ* spectra of formic acid oxidation on the Pd / C catalyst suggests that the film thickness is critical for recording *in situ* spectra of reactions under electrochemical control. The sizes of the particle supports play an important role in controlling the catalyst film thickness on the ATR prism. The Pd / XC-72

particles have small particle size compared to Pd / C and the catalyst film can be made with < 2 μm thickness which is similar to the penetration depth of the evanescent wave of in the ATR setup. Moreover, the electrochemistry of the Premetek catalyst in the SEC cell and the fact that the CO_2 peak in the IR tracks the catalytic current suggest a reliable *in situ* measurement. Therefore, the Pd / XC-72 (Premetek) catalyst was then used for further *in situ* spectroelectrochemical studies of formic acid oxidation and methanol oxidation. In section 3.2.3, the *in situ* spectroelectrochemical approach was used to investigate HPLC grade formic acid oxidation. No CO_{ads} was detected between 0 V to 1.2 V suggesting CO formation from formic acid decomposition is not favourable on Pd in this potential range and this is generally consistent with the widely recognised proposal that formic acid oxidation mainly goes through the direct pathway without CO_{ads} on Pd.

Chapter 4 presents results that demonstrate deactivation of the Pd catalyst due to common impurities in industrial and reagent grade formic acids such as acetic acid, methanol and ethanol. IR peaks which have previously been assigned as multi-bonded CO (CO_M) and hollow-bonded CO (CO_H) were observed during oxidation of reagent grade formic acid, and CO_{ads} was also observed during potential scan in HPLC grade formic acid 'spiked' with 100 ppm ethanol and methanol. This supports the suggestion from literature that deactivation of Pd-based catalysts during formic acid oxidation arises from the impurities in the

fuel. Therefore, the use of Pd-based catalysts in DFAFC is not realistic since it is impractical to use high purity of formic acid for industrial use.

In chapter 5, the IR SEC method is applied to study methanol oxidation on the carbon supported Pd / XC-72 in both acidic and alkaline conditions. The *in situ* SEC study showed that the Pd / XC-72 has low activity for methanol oxidation in acidic condition because the reaction is dominated by the CO pathway. The observation of ν(CO), ν_{as}(OCO) and ν_{as}(OCO) bands of dissolved formate during the potential scan in 0.5 M KOH containing 0.1 M CH_3OH suggests CO and formate both act as the intermediates in electro-oxidation of methanol at the Pd / XC-72 catalyst in alkaline media. This is consistent with the previously proposed reaction pathways for CH_3OH oxidation at the Pd electrode in both acidic and alkaline media which is similar to the case at a Pt electrode.[120,121] Moreover, the fact that the ν_{as}(OCO) of $HCOO^-$ signal is much more intense the ν(CO) signal suggests the reaction favours the formate pathway rather than the CO pathway or that CO is a short-lived intermediate. The ν_s(OCO) band of $HCOO_{ads}$ around 1320 cm^{-1} was detected for the first time for Pd by an *in situ* IR technique in this work. This suggests that bridge-bonded formate is the main reaction intermediate during methanol oxidation on Pd. The reaction mechanism can be summarised as:

(i) In alkaline condition: methanol oxidation mainly goes through the formate pathway. The reaction also goes through the CO pathway, but this is much less favourable.

(ii) In acidic condition: methanol oxidation is dominated by the CO pathway

In chapter 6, a catalytic cascade system for CO_2 electro-reduction to hydrocarbons was preliminarily designed. The designs use copper nanoparticles and the enzyme carbon monoxide dehydrogenase (CODH). Copper is the one of the metals that is able to catalyse CO_2 and CO reduction to hydrocarbons such as methane, ethylene, formic acid and methanol. However, the electro-reduction of CO_2 to CO on a Cu electrode requires high overpotential which limits the turnover rate of CO_2 electro-reduction. CODH has high activity for CO_2 / CO conversion with a midpoint potential around -0.53 V which is very close to the thermodynamic potential of CO_2 reduction to CO. The key idea of the design is that setting up a composite system with the mixture of Cu nanoparticles and CODH enzymes allows the rate-determining step, CO_2 reduction to CO, to be accelerated by CODH, thus increasing the whole turnover rate of CO_2 reduction to hydrocarbons. By immobilising both copper nanoparticles and CODH onto carbon black particles, the preliminary results show more effective electrocatalysis of CO_2 reduction at mild overpotential compared to copper alone on carbon. Future studies will focus on the optimisation of the ratio of Cu and

CODH and on the reaction in the different electrolytes, along with the determination of the product distribution.

7.2 Outlook

- In this Thesis, an *in situ* IR SEC method was applied to study a carbon supported Pd catalyst. This provided significant insight into mechanism of fuel oxidation and poisoning of Pd. This fundamental insight explains previous qualitative observations on Pd catalysts for fuel oxidation and will be useful for designing future Pd-based catalysts for fuel oxidation.

- In the future, similar SEC techniques can be applied to understand how CODH catalyses CO / CO_2 interconversion. This can offer a model for designing future biomimetic catalysts for CO oxidation / CO_2 reduction.

- The SEC technique can be applied to different supported nanocatalysts for different reactions.

Bibliography

1. Raich, J. W. & Schlesinger, W. H. The global carbon dioxide flux in soil respiration and its relationship to vegetation and climate. *Tellus* **44B,** 81–99 (1992).

2. Winkler, W. & Nehter, P. Thermodynamics of fuel cells. *Model. Solid Oxide Fuel Cells* 25–37 (2008). doi:10.1007/978-1-4020-6995-6_2

3. Mekhilef, S., Saidur, R. & Safari, A. Comparative study of different fuel cell technologies. *Renew. Sustain. Energy Rev.* **16,** 981–989 (2012).

4. Andujar, J. M. & Segura, F. Fuel cells: History and updating. A walk along two centuries. *Renew. Sustain. Energy Rev.* **13,** 2309–2322 (2009).

5. Kirubakaran, A., Jain, S. & Nema, R. K. A review on fuel cell technologies and power electronic interface. *Renew. Sustain. Energy Rev.* **13,** 2430–2440 (2009).

6. Wang, Y., Chen, K. S., Mishler, J., Cho, S. C. & Adroher, X. C. A review of polymer electrolyte membrane fuel cells: Technology, applications, and needs on fundamental research. *Appl. Energy* **88,** 981–1007 (2011).

7. Wu, J., Yuan, X. Z., Martin, J. J., Wang, H., Zhang, J., Shen, J., Wu, S. & Merida, W. A review of PEM fuel cell durability: Degradation mechanisms and mitigation strategies. *J. Power Sources* **184,** 104–119 (2008).

8. Zhou, Z.-Y., Tian, N., Huang, Z.-Z., Chen, D.-J. & Sun, S.-G. Nanoparticle catalysts with high energy surfaces and enhanced activity synthesized by electrochemical method. *Faraday Discuss.* **140,** 93–112 (2008).

9. Zhu, Y., Khan, Z. & Masel, R. I. The behavior of palladium catalysts in direct formic acid fuel cells. *J. Power Sources* **139,** 15–20 (2005).

10. Pan, Y., Zhang, R. & Blair, S. L. Anode Poisoning Study in Direct Formic Acid Fuel Cells. *Electrochem. Solid-State Lett.* **12,** B23–B26 (2009).

11. Okamoto, H., Kon, W. & Mukouyama, Y. Five current peaks in voltammograms for oxidations of formic acid, formaldehyde, and methanol on platinum. *J. Phys. Chem. B* **109,** 15659–15666 (2005).

12. Pavese, A., Solis, V. & Giordano, M. C. Electrocatalytic oxidation of formic acid on Pd + Pt alloys of different bulk composition in acidic medium. *J. Electroanal. Chem.* **245,** 145–156 (1988).

13. Obradović, M. D. & Gojković, S. L. HCOOH oxidation on thin Pd layers on Au: Self-poisoning by the subsequent reaction of the reaction product. *Electrochim. Acta* **88,** 384–389 (2013).

14. Brandt, K., Steinhausen, M. & Wandelt, K. Catalytic and electro-catalytic oxidation of formic acid on the pure and Cu-modified Pd(1 1 1)-surface. *J. Electroanal. Chem.* **616,** 27–37 (2008).

15. Arenz, M., Stamenkovic, V., Schmidt, T. J., Wandelt, K., Ross, P. N. & Markovic, N. M. The electro-oxidation of formic acid on Pt?Pd single crystal bimetallic surfaces. *Phys. Chem. Chem. Phys.* **5,** 4242 (2003).

16. Russell, A. E. Preface. *Faraday Discuss.* **140,** 9–10 (2009).

17. Sun, S. G., Clavilier, J. & Bewick, A. The mechanism of electrocatalytic oxidation of formic acid on Pt (100) and Pt (111) in sulphuric acid solution: an emirs study. *J. Electroanal. Chem.* **240,** 147–159 (1988).

18. Samjeske, G., Miki, A., Ye, S. & Osawa, M. Mechanistic study of electrocatalytic oxidation of formic acid at platinum in acidic solution by time-resolved surface-enhanced infrared absorption spectroscopy. *J. Phys. Chem. B* **110,** 16559–16566 (2006).

19. Capon, A. & Parsons, R. The oxidation of formic acid on noble metal electrodes II. A comparison of the behavior of pure electrodes. *J. Electroanal. Chem. Interfacial Electrochem.* **44,** 239–254 (1973).

20. Niquirilo, R. V., Teixeira-Neto, E., Buzzo, G. S. & Suffredini, H. B. Formic acid oxidation at Pd, Pt and PbOx-based catalysts and calculation of their approximate electrochemical active areas. *Int. J. Electrochem. Sci.* **5,** 344–354 (2010).

21. Si, F., Ge, J., Li, C., Liang, L., Liu, C. & Xing, W. Investigations of Pt modified Pd / C catalyst synthesized by one-pot galvanic replacement for formic acid electrooxidation. *Int. J. Hydrogen Energy* **39,** 2489–2496 (2014).

22. Arenz, M., Stamenkovic, V., Ross, P. N. & Markovic, N. M. Surface (electro-)chemistry on Pt(111) modified by a Pseudomorphic Pd monolayer. *Surf. Sci.* **573,** 57–66 (2004).

23. Ha, S., Larsen, R. & Masel, R. I. Performance characterization of Pd / C nanocatalyst for direct formic acid fuel cells. *J. Power Sources* **144,** 28–34 (2005).

24. Liu, H., Song, C., Zhang, L., Zhang, J., Wang, H. & Wilkinson, D. P. A review of anode catalysis in the direct methanol fuel cell. *J. Power Sources* **155,** 95–110 (2006).

25. Yu, X. & Pickup, P. G. Deactivation/reactivation of a Pd/C catalyst in a direct formic acid fuel cell (DFAFC): Use of array membrane electrode assemblies. *J. Power Sources* **187,** 493–499 (2009).

26. Aricò, a S., Srinivasan, S. & Antonucci, V. DMFCs: From Fundamental Aspects to Technology Development. *Fuel Cells* **1,** 133–161 (2001).

27. Wasmus, S. & Küver, A. Methanol oxidation and direct methanol fuel cells: a selective review. *J. Electroanal. Chem.* **461,** 14–31 (1999).

28. Sundmacher, K., Schultz, T., Zhou, S., Scott, K., Ginkel, M. & Gilles, E. D. Dynamics of the direct methanol fuel cell (DMFC): Experiments and model-based analysis. *Chem. Eng. Sci.* **56,** 333–341 (2001).

29. Bianchini, C. & Shen, P. K. Palladium-based electrocatalysts for alcohol oxidation in half cells and in direct alcohol fuel cells. *Chem. Rev.* **109,** 4183–4206 (2009).

30. Borasio, M., De La Fuente, O. R., Rupprechter, G. & Freund, H. J. In situ studies of methanol decomposition and oxidation on Pd(111) by PM-IRAS and XPS spectroscopy. *J. Phys. Chem. B* **109,** 17791–17794 (2005).

31. Collins, S. E., Baltanás, M. A. & Bonivardi, A. L. Mechanism of the decomposition of adsorbed methanol over a Pd/α,ß-Ga2O3 catalyst. *Appl. Catal. A Gen.* **295,** 126–133 (2005).

32. Xiong, Y., Liu, Q. L., Zhu, A. M., Huang, S. M. & Zeng, Q. H. Performance of organic-inorganic hybrid anion-exchange membranes for alkaline direct methanol fuel cells. *J. Power Sources* **186,** 328–333 (2009).

33. Yu, E. H. & Scott, K. Development of direct methanol alkaline fuel cells using anion exchange membranes. *J. Power Sources* **137,** 248–256 (2004).

34. Matsuoka, K., Iriyama, Y., Abe, T., Matsuoka, M. & Ogumi, Z. Alkaline direct alcohol fuel cells using an anion exchange membrane. *J. Power Sources* **150,** 27–31 (2005).

35. Lue, S. J., Wang, W. T., Mahesh, K. P. O. & Yang, C. C. Enhanced performance of a direct methanol alkaline fuel cell (DMAFC) using a polyvinyl alcohol/fumed silica/KOH electrolyte. *J. Power Sources* **195,** 7991–7999 (2010).

36. Prabhuram, J. & Manoharan, R. Investigation of methanol oxidation on unsupported platinum electrodes in strong alkali and strong acid. *J. Power Sources* **74,** 7 (1998).

37. Nishimura, K., Kunimatsu, K. & Enyo, M. Electrocatalysis on Pd + Au alloy electrodes. Part III. IR spectroscopic studies on the surface species derived from CO and CH3OH in NaOH solution. *J. Electroanal. Chem.* **260,** 167–179 (1989).

38. Schwab, G.-M. Advances in Catalysis. *Zeitschrift für Phys. Chemie* **63,** 219–220 (1969).

39. Balandin, A. A. Modern State of the Multiplet Theor of Heterogeneous Catalysis1. *Adv. Catal.* **19,** 1–210 (1969).

40. Helmut Knözinger, K. K. *'Heterogeneous Catalysis and Solid Catalysts', Ullmann's Encyclopedia of Industrial Chemistry*. (Wiley-VCH Verlag, 2005).

41. Van der Spoel, E., Rozing, M. P., Houwing-Duistermaat, J. J., Eline Slagboom, P., Beekman, M., De Craen, A. J. M., Westendorp, R. G. J. & Van Heemst, D. Association analysis of insulin-like growth factor-1 axis parameters

with survival and functional status in nonagenarians of the Leiden Longevity Study. *Aging (Albany. NY).* **7,** 956–963 (2015).

42. Zaera, F. Probing liquid / solid interfaces at the molecular level. *Chem. Rev.* **112,** 2920–2986 (2012).

43. Blyholder, G. Molecular orbital view of chemisorbed carbon monoxide. *J. Phys. Chem. A* **68,** 2772–2777 (1964).

44. Hoffmann, F. Infrared reflection-absorption spectroscopy of adsorbed molecules. *Surf. Sci. Rep.* **3,** 107 (1983).

45. Yan, Y. G., Li, Q. X., Huo, S. J., Ma, M., Cai, W. Bin & Osawa, M. Ubiquitous strategy for probing ATR surface-enhanced infrared absorption At platinum group metal-electrolyte interfaces. *J. Phys. Chem. B* **109,** 7900–7906 (2005).

46. Sun, S. G., Christensen, P. A. & Wiñeckowski, A. *In-situ spectroscopic studies of adsorption at the electrode and electrocatalysis*. (Elsevier, 2007).

47. Osawa, M. Dynamic Processes in Electrochemical Reactions Studied by Surface-Enhanced Infrared Absorption Spectroscopy (SEIRAS). *Bull. Chem. Soc. Jpn.* **70,** 2861–2880 (1997).

48. Hartstein, A., Kirtley, J. R. & Tsang, J. C. Enhancement of the infrared absorption from molecular monolayers with thin metal overlayers. *Phys. Rev. Lett.* **45,** 201–204 (1980).

49. Hatta, A., Suzuki, Y. & Suëtaka, W. Infrared absorption enhancement of monolayer species on thin evaporated Ag films by use of a Kretschmann configuration: Evidence for two types of enhanced surface electric fields. *Appl. Phys. A Solids Surfaces* **35,** 135–140 (1984).

50. Chen, D., Sun, S. & Tong, Y. Y. J. On the chemistry of activation of a commercial carbon-supported PtRu electrocatalyst for the methanol oxidation reaction †. *Chem. Commun.* **50,** 12963–12965 (2014).

51. Hofstead-Duffy, A. M., Chen, D. J. & Tong, Y. J. An in situ attenuated total reflection-surface enhanced infrared absorption spectroscopic study of enhanced methanol electro-oxidation activity on carbon-supported Pt nanoparticles by poly(vinylpyrrolidone) of different molecular weights. *Electrochim. Acta* **82,** 543–549 (2012).

52. Stamenkovié, V., Arenz, M., Ross, P. N. & Markovié, N. M. Temperature-induced deposition method for anchoring metallic nanoparticles onto reflective substrates for in situ electrochemical infrared spectroscopy. *J. Phys. Chem. B* **108,** 17915–17920 (2004).

53. Albo, J. & Irabien, A. Non-dispersive absorption of CO_2 in parallel and cross-flow membrane modules using EMISE. *J. Chem. Technol. Biotechnol.* **87,** 1502–1507 (2012).

54. D'Alessandro, D. M., Smit, B. & Long, J. R. Carbon dioxide capture: Prospects for new materials. *Angew. Chemie - Int. Ed.* **49,** 6058–6082 (2010).

55. Boot-Handford, M. E., Abanades, J. C., Anthony, E. J., Blunt, M. J., Brandani, S., Mac Dowell, N., Fernandez, J. R., Ferrari, M.-C. M.-C., Gross, R., Hallett, J. P., Haszeldine, R. S., Heptonstall, P., Lyngfelt, A., Makuch, Z., Mangano, E., Porter, R. T. J., Pourkashanian, M., Rochelle, G. T., Shah, N., Yao, J. G., Fennell, P. S., Fernández, J. R., Ferrari, M.-C. M.-C., Gross, R., Hallett, J. P., Haszeldine, R. S., Heptonstall, P., Lyngfelt, A., Makuch, Z., Mangano, E., Porter, R. T. J., Pourkashanian, M., Rochelle, G. T., Shah, N., Yao, J. G. & Fennell, P. S. Carbon capture and storage update. *Energy Environ. Sci.* **7,** 130–189 (2014).

56. Whipple, D. T. & Kenis, P. J. A. Prospects of CO_2 utilization via direct heterogeneous electrochemical reduction. *J. Phys. Chem. Lett.* **1,** 3451–3458 (2010).

57. Albo, J., Alvarez-Guerra, M., Castaño, P. & Irabien, A. Towards the electrochemical conversion of carbon dioxide into methanol. *Green Chem.* **17,** 2304–2324 (2015).

58. Alvarez-Guerra, M., Quintanilla, S. & Irabien, A. Conversion of carbon dioxide into formate using a continuous electrochemical reduction process in a lead cathode. *Chem. Eng. J.* **207-208,** 278–284 (2012).

59. Kas, R., Kortlever, R., Milbrat, A., Koper, M. T. M., Mul, G. & Baltrusaitis, J. Electrochemical CO_2 reduction on Cu_2O-derived copper nanoparticles: controlling the catalytic selectivity of hydrocarbons. *Phys. Chem. Chem. Phys.* **16,** 12194–201 (2014).

60. Gattrell, M., Gupta, N. & Co, A. Electrochemical reduction of CO_2 to hydrocarbons to store renewable electrical energy and upgrade biogas. *Energy Convers. Manag.* **48,** 1255–1265 (2007).

61. Lewis, N. S. & Nocera, D. G. Powering the planet: chemical challenges in solar energy utilization. *Proc. Natl. Acad. Sci. U. S. A.* **103,** 15729–35 (2006).

62. Oloman, C. & Li, H. Electrochemical processing of carbon dioxide. *ChemSusChem* **1,** 385–391 (2008).

63. Kumar, B., Llorente, M., Froehlich, J., Dang, T., Sathrum, A. & Kubiak, C. P. Photochemical and photoelectrochemical reduction of CO2. *Annu. Rev. Phys. Chem.* **63,** 541–69 (2012).

64. Jitaru, M., Lowy, D. a., Toma, M., Toma, B. C. & Oniciu, L. Electrochemical reduction of carbon dioxide on flat metallic cathodes. *J. Appl. Electrochem.* **27,** 875–889 (1997).

65. Smolinka, T., Heinen, M., Chen, Y. X., Jusys, Z., Lehnert, W. & Behm, R. J. CO_2 reduction on Pt electrocatalysts and its impact on H_2 oxidation in CO_2 containing fuel cell feed gas - A combined in situ infrared spectroscopy, mass spectrometry and fuel cell performance study. *Electrochim. Acta* **50,** 5189–5199 (2005).

66. Qiao, J., Liu, Y., Hong, F. & Zhang, J. *A review of catalysts for the electroreduction of carbon dioxide to produce low-carbon fuels. Chemical Society reviews* **43,** (2014).

67. Benson, E. E., Kubiak, C. P., Sathrum, A. J. & Smieja, J. M. Electrocatalytic and homogeneous approaches to conversion of CO_2 to liquid fuels. *Chem. Soc. Rev.* **38,** 89–99 (2009).

68. Wong, K., Chung, W. & Lau, C. The effect of weak Bronsted acids on the electrocatalytic reduction of carbon dioxide by a rhenium tricarbonyl bipyridyl complex. *Jounal Electroanal. Chem.* **453,** 161–170 (1998).

69. Hammouche, M., Lexa, D., Momenteau, M. & Saveant, J. M. Chemical catalysis of electrochemical reactions. Homogeneous catalysis of the electrochemical reduction of carbon dioxide by iron('0') porphyrins. Role of the addition of magnesium cations. *J. Am. Chem. Soc.* **113,** 8455–8466 (1991).

70. Bhugun, I., Lexa, D. & Savéant, J. Catalysis of the Electrochemical Reduction of Carbon Dioxide by Iron(0) Porphyrins. Synergistic Effect of Lewis Acid Cations. *J. Am. Chem. Soc.* **118,** 1769–1776 (1996).

71. Hori, Y., Murata, A., Takahashi, R. & Suzuki, S. Enhanced formation of ethylene and alcohols at ambient temperature and pressure in electrochemical reduction of carbon dioxide at a copper electrode. *J. Chem. Soc. Chem. Commun.* **109,** 17 (1988).

72. Hori, Y., Murata, A. & Takahashi, R. Formation of hydrocarbons in the electrochemical reduction of carbon dioxide at a copper electrode in aqueous solution. *J. Chem. Soc. Faraday Trans. 1 Phys. Chem. Condens. Phases* **85,** 2309 (1989).

73. Hori, Y., Murata, A., Takahashi, R. & Suzuki, S. Enhanced formation of ethylene and alcohols at ambient temperature and pressure in electrochemical reduction of carbon dioxide at a copper electrode. *J. Chem. Soc. Chem. Commun.* **109,** 17 (1988).

74. Hori, Y., Koga, O., Yamazaki, H. & Matsuo, T. Infrared spectroscopy of adsorbed CO and intermediate species in electrochemical reduction of CO2 to hydrocarbons on a Cu electrode. *Electrochim. Acta* **40,** 2617–2622 (1995).

75. Oda, I., Ogasawara, H. & Ito, M. Carbon monoxide adsorption on copper and silver electrodes during carbon dioxide electroreduction studied by infrared

reflection absorption spectroscopy and surface-enhanced Raman spectroscoopy. *Langmuir* **12,** 1094–1097 (1996).

76. Ragsdale, S. W. Life with Carbon Monoxide. *Crit. Rev. Biochem. Mol. Biol.* **39,** 165–195 (2004).

77. Svetlitchnyi, V., Peschel, C., Acker, G. & Meyer, O. Two membrane-associated NiFeS-carbon monoxide dehydrogenases from the anaerobic carbon-monoxide-utilizing eubacterium Carboxydothermus hydrogenoformans. *J. Bacteriol.* **183,** 5134–5144 (2001).

78. Hu, Z., Spangler, N. J., Anderson, M. E., Xia, J., Ludden, P. W., Lindahl, P. A. & Mu, E. Nature of the C-Cluster in Ni-Containing Carbon Monoxide Dehydrogenases. *J. Am. Chem. Soc.* **118,** 830–845 (1996).

79. Wang, V. C. C., Ragsdale, S. W. & Armstrong, F. A. Investigations of two bidirectional carbon monoxide dehydrogenases from carboxydothermus hydrogenoformans by protein film electrochemistry. *ChemBioChem* **14,** 1845–1851 (2013).

80. Kung, Y., Doukov, T. I., Seravalli, J., Ragsdale, S. W. & Drennan, C. L. Crystallographic snapshots of cyanide- and water-bound C-clusters from bifunctional carbon monoxide dehydrogenase/acetyl-CoA synthase. *Biochemistry* **48,** 7432–7440 (2009).

81. Volbeda, A. & Fontecilla-Camps, J. Crystallographic evidence for a CO / CO_2 tunnel gating mechanism in the bifunctional carbon monoxide dehydrogenase/acetyl coenzyme A synthase from Moorella thermoacetica. *JBIC J. Biol. Inorg. Chem.* **9,** 525–532 (2004).

82. Dobbek, H. Crystal Structure of a Carbon Monoxide Dehydrogenase Reveals a [Ni-4Fe-5S] Cluster. *Science (80-.).* **293,** 1281–1285 (2001).

83. Armstrong, F. A. & Hirst, J. Reversibility and efficiency in electrocatalytic energy conversion and lessons from enzymes. *Proc. Natl. Acad. Sci. U. S. A.* **108,** 14049–54 (2011).

84. Parkin, A., Seravalli, J., Vincent, K. A., Ragsdale, S. W. & Armstrong, F. A. Rapid and efficient electrocatalytic CO2/CO interconversions by Carboxydothermus hydrogenoformans CO dehydrogenase I on an electrode. *J. Am. Chem. Soc.* **129,** 10328–10329 (2007).

85. Christmann K. & Ertl G. *Catalyst Characterization Science.* **288,** (American Chemical Society, 1985).

86. Wolf, K. B. & Krotzsch, G. Geometry and dynamics in refracting systems. *Eur. J. Phys.* **16,** 14–20 (1999).

87. Zhang, H.-X., Wang, H., Re, Y.-S. & Cai, W.-B. Palladium nanocrystals bound by {110} or {100} facets: from one pot synthesis to electrochemistry. *Chem. Commun.* **48,** 8362 (2012).

88. Grdeń, M., Łukaszewski, M., Jerkiewicz, G. & Czerwiński, A. Electrochemical behaviour of palladium electrode: Oxidation, electrodissolution and ionic adsorption. *Electrochim. Acta* **53,** 7583–7598 (2008).

89. Zhou, W. P., Lewera, A., Larsen, R., Masel, R. I., Bagus, P. S. & Wieckowski, A. Size effects in electronic and catalytic properties of unsupported palladium nanoparticles in electrooxidation of formic acid. *J. Phys. Chem. B* **110,** 13393–13398 (2006).

90. Zalineeva, A., Baranton, S., Coutanceau, C. & Jerkiewicz, G. Electrochemical behavior of unsupported shaped palladium nanoparticles. *Langmuir* **31,** 1605–1609 (2015).

91. Will, F. G. Hydrogen Adsorption on Platinum Single Crystal Electrodes. *J. Electrochem. Soc.* **112,** 451 (1965).

92. Zhang, L. Y., Zhao, Z. L. & Li, C. M. Formic acid-reduced ultrasmall Pd nanocrystals on graphene to provide superior electocatalytic activity and stability toward formic acid oxidation. *Nano Energy* **11,** 71–77 (2015).

93. Wang, S. & Manthiram, A. Graphene ribbon-supported Pd nanoparticles as highly durable, efficient electrocatalysts for formic acid oxidation. *Electrochim. Acta* **88,** 565–570 (2013).

94. Garbarino, S. & Burke, L. D. The surface active site model for formic acid electrooxidation at palladium in aqueous acid solution. *Int. J. Electrochem. Sci.* **5,** 828–851 (2010).

95. Yu, X. & Pickup, P. G. Mechanistic study of the deactivation of carbon supported Pd during formic acid oxidation. *Electrochem. Commun.* **11,** 2012–2014 (2009).

96. Claudel, B., Nueilati, M. & Andrieu, J. Oxidation of formic acid in aqueous solution by palladium catalysts. *Appl. Catal.* **11,** 217–225 (1984).

97. Miyake, H., Okada, T., Samjeské, G. & Osawa, M. Formic acid electrooxidation on Pd in acidic solutions studied by surface-enhanced infrared absorption spectroscopy. *Phys. Chem. Chem. Phys.* **10,** 3662 (2008).

98. Mikołajczuk, A., Borodzinski, A., Kedzierzawski, P., Stobinski, L., Mierzwa, B. & Dziura, R. Deactivation of carbon supported palladium catalyst in direct formic acid fuel cell. *Appl. Surf. Sci.* **257,** 8211–8214 (2011).

99. Lambert, D. K. & Tobin, R. G. CO on Pt(335): Vibrational Stark effect, mode coupling, and local field effects on a stepped surface. *Surf. Sci.* **232,** 149–160 (1990).

100. Lambert, D. K. Vibrational Stark effect of CO on Ni (100), and CO in the aqueous double layer: Experiment, theory, and models. *J. Chem. Phys.* **89,** 3847–3860 (1988).

101. Garbarino, S. & Burke, L. D. The surface active site model for formic acid electrooxidation at palladium in aqueous acid solution. *Int. J. Electrochem. Sci.* **5,** 828–851 (2010).

102. Jiang, K., Zhang, H.-X., Zou, S. & Cai, W.-B. Electrocatalysis of formic acid on palladium and platinum surfaces: from fundamental mechanisms to fuel cell applications. *Phys. Chem. Chem. Phys.* **16,** 20360–20376 (2014).

103. Yen, Y. S. & Wong, J. S. Infrared reflectance properties of surface thin films. *J. Phys. Chem.* **93,** 7208–7216 (1989).

104. Miljković, M., Bird, B. & Diem, M. Line shape distortion effects in infrared spectroscopy. *Analyst* **137,** 3954–64 (2012).

105. Mcpherson, I. DPhil thesis: An Infrared Spectroelectrochemical Approach for Understanding Electrocatalysis at Supported Metal Nanoparticles. *Univ. Oxford* (2016).

106. Rezaei, M., Tabaian, S. H. & Haghshenas, D. F. The Role of Electrodeposited Pd Catalyst Loading on the Mechanisms of Formic Acid Electro-Oxidation. *Electrocatalysis* **5,** 193–203 (2014).

107. Zhang, H. X., Wang, S. H., Jiang, K., André, T. & Cai, W. Bin. In situ spectroscopic investigation of CO accumulation and poisoning on Pd black surfaces in concentrated HCOOH. *J. Power Sources* **199,** 165–169 (2012).

108. Wang, J. Y., Zhang, H. X., Jiang, K. & Cai, W. Bin. From HCOOH to CO at Pd electrodes: A surface-enhanced infrared spectroscopy study. *J. Am. Chem. Soc.* **133,** 14876–14879 (2011).

109. Hoshi, N., Kida, K., Nakamura, M., Nakada, M. & Osada, K. Structural effects of electrochemical oxidation of formic acid on single crystal electrodes of palladium. *J. Phys. Chem. B* **110,** 12480–12484 (2006).

110. Osawa, M., Komatsu, K. I., Samjeské, G., Uchida, T., Ikeshoji, T., Cuesta, A. & Gutiérrez, C. The role of bridge-bonded adsorbed formate in the electrocatalytic oxidation of formic acid on platinum. *Angew. Chemie - Int. Ed.* **50,** 1159–1163 (2011).

111. Pronkin, S., Hara, M. & Wandlowski, T. Electrocatalytic properties of Au(111)-Pd quasi-single-crystal film electrodes as probed by ATR-SEIRAS. *Russ. J. Electrochem.* **42,** 1177–1192 (2006).

112. Uhm, S., Lee, H. J. & Lee, J. Understanding underlying processes in formic acid fuel cells. *Phys. Chem. Chem. Phys.* **11,** 9326–9336 (2009).

113. Law, W. L., Platt, A. M., Wimalaratne, P. D. C. & Blair, S. L. Effect of Organic Impurities on the Performance of Direct Formic Acid Fuel Cells. *J. Electrochem. Soc.* **156,** B553 (2009).

114. Rudi, S., Tuaev, X. & Strasser, P. Electrocatalytic Oxygen Reduction on Dealloyed Pt1-xNix Alloy Nanoparticle Electrocatalysts. *Electrocatalysis* **3,** 265–273 (2012).

115. Kunimatsu, K., Hanawa, H., Uchida, H. & Watanabe, M. Role of adsorbed species in methanol oxidation on Pt studied by ATR-FTIRAS combined with linear potential sweep voltammetry. *J. Electroanal. Chem.* **632,** 109–119 (2009).

116. Iwasita, T. Electrocatalysis of methanol oxidation. *Electrochim. Acta* **47,** 3663–3674 (2002).

117. Batista, E. A., Malpass, G. R. P., Motheo, A. J. & Iwasita, T. New mechanistic aspects of methanol oxidation. *J. Electroanal. Chem.* **571,** 273–282 (2004).

118. Tripkovi, A. V., Popovi, K. D., Grgur, B. N., Blizanac, B., Ross, P. N. & Markovi, N. M. Methanol electrooxidation on supported Pt and PtRu catalysts in acid and alkaline solutions. *Electrochim. Acta* **47,** 3707–3714 (2002).

119. Chen, Y. X., Miki, A., Ye, S., Sakai, H. & Osawa, M. Formate, an active intermediate for direct oxidation of methanol on Pt electrode. *J. Am. Chem. Soc.* **125,** 3680–3681 (2003).

120. Zhou, Z. Y., Tian, N., Chen, Y. J., Chen, S. P. & Sun, S. G. In situ rapid-scan time-resolved microscope FTIR spectroelectrochemistry: Study of the

dynamic processes of methanol oxidation on a nanostructured Pt electrode. *J. Electroanal. Chem.* **573,** 111–119 (2004).

121. Christensen, P. A. & Linares-Moya, D. The role of adsorbed formate and oxygen in the oxidation of methanol at a polycrystalline Pt electrode in 0.1 M KOH: An in situ fourier transform infrared study. *J. Phys. Chem. C* **114,** 1094–1101 (2010).

122. Wang, X., Wang, W., Qi, Z., Zhao, C., Ji, H. & Zhang, Z. Electrochemical catalytic activities of nanoporous palladium rods for methanol electro-oxidation. *J. Power Sources* **195,** 6740–6747 (2010).

123. Mellinger, Z. J., Kelly, T. G. & Chen, J. G. Pd-modified tungsten carbide for methanol electro-oxidation: From surface science studies to electrochemical evaluation. *ACS Catal.* **2,** 751–758 (2012).

124. Yang, Y. Y., Ren, J., Zhang, H. X., Zhou, Z. Y., Sun, S. G. & Cai, W. Bin. Infrared spectroelectrochemical study of dissociation and oxidation of methanol at a palladium electrode in alkaline solution. *Langmuir* **29,** 1709–1716 (2013).

125. Vračar, L., Burojević, S. & Krstajić, N. The surface processes at Pd–Ni alloy in acid and alkaline solutions. *Int. J. Hydrogen Energy* **23,** 1157–1164 (1998).

126. Prabhuram, J. & Manoharan, R. Effects of incorporation of Cu and Ag in Pd on electrochemical oxidation of methanol in alkaline solution. *J. Appl. Electrochem.* **28,** 935–941 (1998).

127. Liang, Z. X., Zhao, T. S., Xu, J. B. & Zhu, L. D. Mechanism study of the ethanol oxidation reaction on palladium in alkaline media. *Electrochim. Acta* **54,** 2203–2208 (2009).

128. Grdeń, M. & Czerwiński, A. EQCM studies on Pd-Ni alloy oxidation in basic solution. *J. Solid State Electrochem.* **12,** 375–385 (2008).

129. Zhou, Z. Y., Tian, N., Chen, Y. J., Chen, S. P. & Sun, S. G. In situ rapid-scan time-resolved microscope FTIR spectroelectrochemistry: Study of the dynamic processes of methanol oxidation on a nanostructured Pt electrode. *J. Electroanal. Chem.* **573,** 111–119 (2004).

130. Zhao, Y., Zhan, L., Tian, J., Nie, S. & Ning, Z. MnO2 modified multi-walled carbon nanotubes supported Pd nanoparticles for methanol electro-oxidation in alkaline media. *Int. J. Hydrogen Energy* **35,** 10522–10526 (2010).

131. Christensen, P. A. & Linares-Moya, D. The role of adsorbed formate and oxygen in the oxidation of methanol at a polycrystalline Pt electrode in 0.1 M KOH: An in situ fourier transform infrared study. *J. Phys. Chem. C* **114,** 1094–1101 (2010).

132. Berna, A., Rodes, A., Feliu, J. M., Illas, F., Gil, A., Clotet, A. & Ricart, J. M. Structural and spectroelectrochemical study of carbonate and bicarbonate adsorbed on Pt(111) and Pd/Pt(lll) electrodes. *J. Phys. Chem. B* **108,** 17928–17939 (2004).

133. Zhou, Z. Y., Wang, Q., Lin, J. L., Tian, N. & Sun, S. G. In situ FTIR spectroscopic studies of electrooxidation of ethanol on Pd electrode in alkaline media. *Electrochim. Acta* **55,** 7995–7999 (2010).

134. Ataka, K., Yotsuyanagi, T. & Osawa, M. Potential-Dependent Reorientation of Water Molecules at an Electrode/Electrolyte Interface Studied by Surface-Enhanced Infrared Absorption Spectroscopy. *J. Phys. Chem.* **100,** 10664–10672 (1996).

135. Lucks, C., Rossberg, A., Tsushima, S., Foerstendorf, H., Fahmy, K. & Bernhard, G. Formic acid interaction with the uranyl(VI) ion: structural and photochemical characterization. *Dalton Trans.* **42,** 13584–9 (2013).

136. Liu, Y., Wang, L., Wang, G., Deng, C., Wu, B. & Gao, Y. High active carbon supported PdAu catalyst for formic acid electrooxidation and study of the kinetics. *J. Phys. Chem. C* **114,** 21417–21422 (2010).

137. Duca, M., Weeks, J. R., Fedor, J. G., Weiner, J. H. & Vincent, K. A. Combining Noble Metals and Enzymes for Relay Cascade Electrocatalysis of

Nitrate Reduction to Ammonia at Neutral pH. *ChemElectroChem* **2,** 1086–1089 (2015).

138. Léger, C. & Bertrand, P. Direct electrochemistry of redox enzymes as a tool for mechanistic studies. *Chem. Rev.* **108,** 2379–2438 (2008).

139. Quinson, J., Hidalgo, R., Ash, P. a, Dillon, F., Grobert, N. & Vincent, K. a. Comparison of carbon materials as electrodes for enzyme electrocatalysis: hydrogenase as a case study. *Faraday Discuss.* **172,** 473–96 (2014).

140. Hidalgo, R., Ash, P. A., Healy, A. J. & Vincent, K. A. Infrared Spectroscopy During Electrocatalytic Turnover Reveals the Ni-L Active Site State During H_2 Oxidation by a NiFe Hydrogenase. *Angew. Chemie - Int. Ed.* **54,** 7110–3 (2015).

141. Lazarus, O., Woolerton, T. W., Parkin, A., Lukey, M. J., Reisner, E., Seravalli, J., Pierce, E., Ragsdale, S. W., Sargent, F. & Armstrong, F. A. Water-gas shift reaction catalyzed by redox enzymes on conducting graphite platelets. *J. Am. Chem. Soc.* **131,** 14154–14155 (2009).

142. Paracchino, A., Laporte, V., Sivula, K., Grätzel, M. & Thimsen, E. Highly active oxide photocathode for photoelectrochemical water reduction. *Nat. Mater.* **10,** 456–461 (2011).